Cool Stellar Activity at Low Radio Frequencies

Mr. Andrew John Zic

A thesis submitted to fulfil requirements for the degree:

Doctor of Philosophy (PhD)

Supervisor:
Prof. Tara Murphy

Co-supervisors:
Dr. Christene Lynch & Dr. George Heald

Sydney Insititute for Astronomy
School of Physics
The University of Sydney

CSIRO Astronomy and Space Science

2020

Dedicated to the memory of Mr. Daniele Velcich OAM,
and Prof. Richard Hunstead.

Declaration of originality

I certify that to the best of my knowledge, the content of this thesis submitted in fulfillment for the degree of Doctor of Philosophy (PhD) is my own work. This thesis has not been submitted for any degree or other purposes. I certify that the authorship attribution statement on the following page are correct.

Mr. Andrew John Zic

August 28, 2020

As supervisor for the candidature upon which this thesis is based, I confirm that the originality and authorship attribution statements above and on the next page are correct.

Prof. Tara Murphy

August 28, 2020

Included papers and attribution

Chapters 2, 3, and 4 are peer-reviewed journal articles led by myself, published as Zic et al. (2019a), Zic et al. (2019b), and Zic et al. (2020) respectively. These chapters have been reproduced as published, except for minor typographical and formatting changes to keep consistent style throughout this thesis. Important contributions from others toward the work in this thesis are as follows. Tara Murphy: general supervision and guidance, advice on experimental design and analysis. Christene Lynch: assistance with data reduction and numerical modelling, advice on scientific interpretation and analysis. George Heald: advice on polarimetry, analysis, modelling and interpretation. Emil Lenc: reduction of ASKAP observations, and advice on radio data reduction. David L. Kaplan: advice on scientific analysis, interpretation, statistics, and on optical data reduction. Adam Stewart: assistance with data analysis and interpretation. Specific contributions are detailed at the beginning of each chapter.

Chapter 2

Low-frequency GMRT observations of ultra-cool dwarfs

Andrew Zic, Christene Lynch, Tara Murphy, David L. Kaplan, and
Poonam Chandra

Published in *Monthly Notices of the Royal Astronomical Society*, 483, 614, 2019a.

Chapter 3

ASKAP detection of periodic and elliptically polarized radio pulses from UV Ceti

Andrew Zic, Adam Stewart, Emil Lenc, Tara Murphy, Christene Lynch,
David L. Kaplan, Aidan Hotan, Craig Anderson, John D. Bunton,
Aaron Chippendale, Stacy Mader, and Chris Phillips

Published in *Monthly Notices of the Royal Astronomical Society*, 488, 559, 2019b.

Chapter 4

A Flare–Type IV Burst Event from Proxima Centauri and Implications for Space Weather

Andrew Zic, Tara Murphy, Christene Lynch, George Heald, Emil Lenc,
David L. Kaplan, Iver H. Cairns, David Coward, Bruce Gendre, Helen Johnston,
Meredith MacGregor, Danny C. Price, and Michael S. Wheatland

Published in *The Astrophysical Journal*, 905, 23, 2020.

Acknowledgements

This thesis represents a significant milestone in my research career and personal life. I am very fortunate to have been given many wonderful opportunities and experiences throughout my candidature, and am grateful for the many people who supported me along the way. I would like to dedicate this thesis to the memory of my Nonno, Mr. Daniele Velcich OAM, and Prof. Richard “Dick” Hunstead, who sadly passed away during the course of my PhD candidature. Firstly, I would like to share some reflections on them both.

Nonno was endlessly generous, and had an uncanny ability to bring laughter to any situation with his singing, dancing, and absolutely unique sense of humour. His qualities, and my time spent with him, shaped me as a person. He was much loved by his community, by his family, and is greatly missed.

Dick Hunstead was my first research supervisor, when I was a first-year undergraduate lucky enough to partake in the Talented Student Program (TSP) at the USyd School of Physics. Like many other TSP students, this was my first taste of scientific and astronomical research, and played a major role in guiding me to where I am now. Dick remained involved in my research activities from then onwards, mentoring me throughout my Honours, and occasionally through my PhD. I am grateful to have had the chance to work with him, and for his work in making the TSP program successful at The School of Physics, which gave me the opportunity to kick-start my research career.

I would also like to pay respects to A/ Prof. Jean-Pierre “JP” Macquart, who sadly passed away in 2020. I will remember him for his lively discussions with his colleagues and myself, his intellect, and for his kind heart.

I would like to express my deepest appreciation to my partner, Charlotte, my parents, Julie and John, and my sister, Karina, for their unwavering support, encouragement, and love throughout the ups and downs of the last few years. I love you all.

I am extremely grateful to my supervisor, Tara Murphy. It has been a privilege to work with Tara for the last six years, during undergraduate and Summer research projects, Honours, MOOC course development, teaching, and finally my PhD. Her ongoing support, guidance, and advice has stimulated me to grow as a researcher and as a person.

I would also like to deeply thank my co-supervisors Christene Lynch and George Heald for sharing their guidance and expertise with me, for being there to help me through any research problems, and for giving advice on topics of science, careers, and more. It has been wonderful to work with them both.

I am glad to have had the opportunity to work closely with several collaborators beyond my supervision group. These include David L. Kaplan, Emil Lenc, Adam Stewart, and Meredith MacGregor. I am also grateful for the discussions and advice from many excellent researchers who I have met throughout my PhD: Craig Anderson, Marin Anderson, Martin Bell, Ramesh Bhat, Shivani Bhandari, Shari Breen, Iver Cairns, Joe Callingham, David Coward, Shi Dai, Ron Ekers, Bruce Gendre, Gregg Hallinan, Paul Hancock, George Hobbs, Ward Howard, Huib Intema, Helen Johnston, Chris Jordan, Jane Kaczmarek, JP Macquart, Don Melrose, John Morgan, Vanessa Moss, Simon Murphy, Bob Mutel, Rachel Osten, Sebastian Pineda, Danny Price, Ryan Shannon, Michael Wheatland, and Stephen White.

One of the best parts of undertaking a PhD was having the opportunity to befriend many fellow students and early-career researchers from within the department, around Australia, and internationally. I thank all of them for making conferences fun, and I look forward to seeing them again in the future. I am also very grateful to all my friends outside of astronomy for being the best pals a PhD student can get, especially when times weren't so great.

I would like to thank my grandparents, Neno and Dedo, Nonna and Nonno, for always welcoming me with a warm hug, and fresh bread or a bowl of soup. I love you, and Nonno, I miss you. I'd also like to thank the rest of my extended family for bringing a great deal of joy into my life, for their support, and for asking fun questions about my research. I extend a special thanks to Dan and Mik for letting me crash at their place during my trips to Perth.

I wish the best of luck to the next generation of radio transients students – Andy Wang, Daniele D'Antonio, James Leung, Josh Pritchard, Mark Edwards, Teresa Klinner-Teo, and Yuanming Wang – and I thank them for the enthusiasm and ideas they bring to the group. I am also greatly indebted to Josh for his careful proofreading of this thesis.

I'd like to thank all my PhD officemates, past and current: Dougal Dobie, Harry Qiu, Mohammed Rafat, Kat Ross, Troy Whinray, and Charlotte Ward. It's been a blast working with you, yelling when code breaks, complaining about writing, talking about science problems (whether sensical or not), discussing sport, politics, and all other sorts of shenanigans. I'll miss being around you all. Dougal, it's been great to work alongside you under Tara since the early days, and it's pretty sweet that we get to submit our theses on the same date. Good luck in your new role at Swinburne.

Finally, I am very grateful for the support I have received from The University of Sydney, CSIRO Astronomy and Space Science, and the ARC Centre for All-Sky Astrophysics. I also acknowledge support from the Australian Government through the Research Training Program scholarship.

Abstract

Stellar magnetic fields drive a wide range of energetic phenomena, which have a crucial influence on their properties, evolution, and environment. In this thesis, we investigate the low-frequency radio emission from active low-mass stars. We harness this emission to constrain magnetospheric properties and processes arising from different magnetic activity paradigms. In Chapter 2, we present low-frequency observations of a sample of ultra-cool dwarfs. We show that while most ultra-cool dwarfs do not produce low-frequency emission, their magnetospheric properties can be constrained with measurements of the optically-thick side of the quiescent spectral energy distribution. In Chapter 3, we present Australian Square Kilometre Array Pathfinder (ASKAP) observations of the prototypical flare star, UV Ceti. Our observations reveal the presence of periodic, elliptically polarised radio pulses, confirming that large auroral current systems can be produced in the magnetospheres of active M-dwarfs. In Chapter 4, we present results from one night of an 11-night multi-wavelength campaign targeting the nearest stellar neighbour, and magnetically-active planet host, Proxima Centauri. We detected a powerful flare with optical photometric and spectroscopic facilities, accompanied by a solar-like type IV radio burst. By analogy with the solar radio burst paradigm, we suggest that this event indicates a coronal mass ejection leaving the corona, and ongoing electron acceleration associated with a post-eruptive loop arcade.

Together, the results presented in this thesis show the diverse forms of magnetic activity exhibited by low-mass stars. We have shown that low-frequency radio observations are sensitive to both auroral and solar-like activity. Future low-frequency radio surveys and multi-wavelength observations may reveal the role of stellar properties such as rotation, mass, and age, in driving these different forms of magnetic activity.

Contents

List of Figures

List of Tables

Chapter 1

Introduction

1.1 Stellar and planetary magnetic fields

On September 1 1859, during routine solar observations, R. C. Carrington observed two "intensely bright and white patches of light" appear close to a large group of sunspots (Carrington, 1859). This was followed approximately 18 hours later by an intense geomagnetic storm which has now come to be known as the Carrington event, where strong aurorae appeared up to equatorial latitudes, and strong fluctuations in the terrestrial magnetic field were recorded. Though the phenomenon was not understood at the time, Carrington's observations were the first recordings of a solar flare and coronal mass ejection event, and illustrated the significant influence of solar magnetic activity on the Sun and throughout the solar system. Despite the close temporal correspondence between the flare and subsequent geomagnetic storm, the connection between them was not confirmed until several decades later Bartels (1937), following work linking solar activity and geomagnetic activity by Hale (1931).

The solar magnetic field was first discovered by Hale (1908), and was a crucial step toward revealing the link between solar and geomagnetic activity. Beyond the Sun, a broad range of stars are now known to possess magnetic fields, from the coolest brown dwarfs to massive O-type stars, along with evolved giant stars, and stellar remnants such as white dwarfs and neutron stars. Along with stars, solar system planets such as Earth, Jupiter, and Saturn possess magnetic fields which drive auroral current systems. The same is expected to be true for exoplanets (Zarka, 2007), although exoplanetary magnetic fields have yet to be detected. Magnetic fields play a key role in many aspects around these bodies, such as their formation, mass loss, angular momentum evolution, interaction with companions, and for processes within the magnetosphere.

In the following sections, we discuss the generation of magnetic fields, various manifestations of magnetic activity, and important phenomena which are influenced or driven by magnetic activity in low-mass stars.

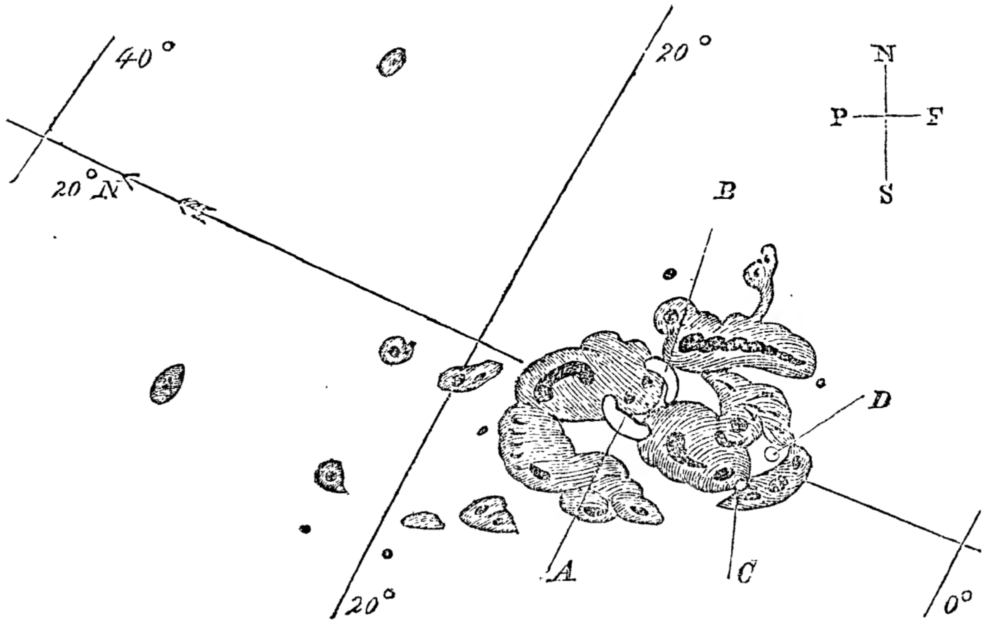

Figure 1.1: Illustration of the flare observed by Carrington (1859) and Hodgson (1859). Bright features, labelled A and B rapidly evolved towards their positions labelled at C and D, where their intensity had greatly declined. The shaded features indicate the structure of a large group of sunspots where the flare originated. Figure from Carrington (1859).

1.1.1 Generation of magnetic fields in low-mass stars

The solar magnetic field is thought to be generated in the region between the radiative core and the convective envelope, called the *tachocline* (Ossendrijver, 2003). The radiative core rotates as a solid body, while the convective envelope exhibits differential rotation, with relatively fast angular velocity near the equator, and slow angular velocity near the poles (Thompson et al., 1996). The interface between these regions is therefore subject to strong and variable shear forces, and gives rise to toroidal structure in the magnetic field from the initially poloidal field generated inside the convective zone (the Ω-effect; Ossendrijver, 2003). Magnetic buoyancy instabilities may cause these toroidal field components to rise through the convective envelope, where they may emerge from the surface and appear as *sunspots*, or be shredded by turbulent convective motion and restored to a poloidal field (α-effect). The sequence of the Ω-effect followed by the α-effect repeats cyclically, and so this dynamo process is known as the α-Ω dynamo.

Stars of mass lower than about $0.35\,\mathrm{M}_\odot$, (spectral type $\sim$M3) do not possess a radiative core. Instead, their interior is *fully convective*, meaning that their interior consists only of a convective layer extending from the centre through to the surface (Chabrier & Baraffe, 1997). The lack of a radiative core with solid-body rotation in the stellar interior means that the α-Ω dynamo mechanism invoked to explain the solar magnetic field cannot operate in these stars. Early numerical simulations suggested that fully-convective stellar interiors should only produce weak, complex magnetic fields (Durney et al., 1993) as opposed to large-scale fields such as the

Sun's. Later work supported the suggestion of a weak or non-existent dipole field component (Shulyak et al., 2015; Browning, 2008; Chabrier & Küker, 2006; Küker & Rüdiger, 1999). However, observations have shown that fully-convective low-mass stars can possess strong magnetic fields at both small and large scales (Reiners & Basri, 2009), which are predominantly poloidal in nature (Morin et al., 2010, 2008; Donati et al., 2006). In addition, fully convective stars exhibit high levels of activity as traced through X-ray and H α emissions (West et al., 2004; Mohanty & Basri, 2003, e.g.). These observations conflicted with early expectations of fully-convective dynamos (Durney et al., 1993), but more recent simulations have been able to explain some key features such as strong magnetic fields (Christensen et al., 2009), presence of small and large scale fields (Yadav et al., 2015), and magnetic cycles similar to the solar cycle (Yadav et al., 2016). However, low-mass binaries where both members have similar masses, age, and rotation rate often exhibit distinct magnetic properties – e.g. L726−8AB (a.k.a. BL-UV Ceti) (Kochukhov & Lavail, 2017), NLTT 33370 (a.k.a. 2MASS J1314+1320) (Williams et al., 2015a; McLean et al., 2011), and Ross 867-8 Quiroga-Nuñez et al., 2020. This suggests that current understanding of fully convective dynamos may be incomplete.

1.1.2 Manifestations of stellar magnetic activity

The generation of magnetic fields by dynamo processes leads to a wide range of phenomena in stellar photospheres and atmospheres. These phenomena can be probed by several methods, which reveal important information about the magnetic field and the activity it drives.

Flares

Flares are sudden, intense brightenings of a star, caused by an explosive release of magnetic energy within its atmosphere. The brightening can occur across the electromagnetic spectrum, from radio frequencies of a few gigahertz up to high-energy X-rays. The first flare observed on the Sun was the so-called Carrington flare, described in Section 1.1 (Carrington, 1859; Hodgson, 1859), and to this day our understanding of these events is primarily formed through solar observations. Flares are typically composed of a pre-flare, impulsive, and a gradual phase. The pre-flare phase is marked by low levels of activity in X-rays and extreme ultraviolet prior to any explosive energy release. The primary release of magnetic energy occurs in the impulsive phase, when the corona, chromosphere and photosphere are bombarded by high-energy particles. At this stage, the energy is directed into plasma heating, particle acceleration, and outflows. Observationally, the impulsive phase is marked by rapidly-increasing and bursty, intense emissions in optical, ultraviolet, and X-rays. In the gradual phase, the intensity slowly decreases as the injected energy decays via radiative and thermal processes.

The mechanism(s) which drive flares are still poorly understood (e.g. Benz, 2017). However, there is general consensus that the gradual motions of magnetic fields within the corona leads to a build-up of energy as the magnetic fields become twisted, followed by *magnetic reconnection*. This phenomenon involves the interaction of oppositely-directed magnetic field lines as they approach one another, leading to

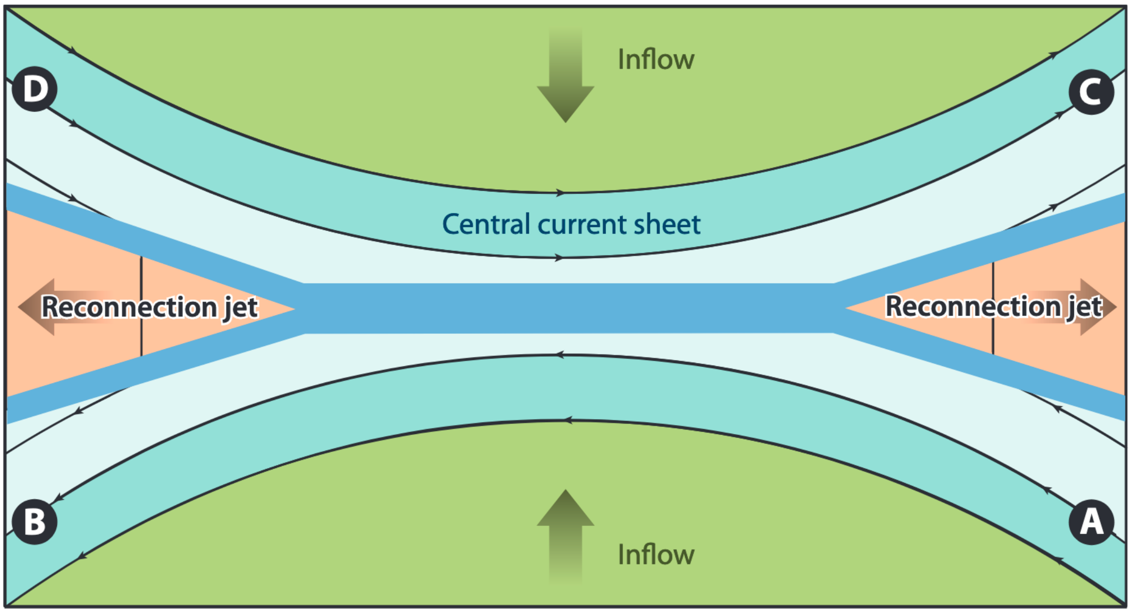

Figure 1.2: Two-dimensional schematic of magnetic reconnection. When oppositely-directed magnetic field lines interact, they drive oppositely-directed current sheets which become increasingly thin, causing an increasing current density. Eventually, there is an impulsive release of energy and the magnetic field reconfigures. Magnetic field lines, originally directed from A to B and D to C, reconfigure to connect A to C and D to B. Figure from Benz & Güdel (2010).

an explosive release of energy as plasma is freed and accelerated, and the magnetic fields restructure into a lower-energy configuration (e.g. Yamada et al., 2010). A simplified illustration of magnetic reconnection is shown in Figure 1.2.

A successful model for explaining many features commonly observed in solar flares is the CSHKP model (named after the its primary contributors: Carmichael, 1964; Sturrock, 1966; Hirayama, 1974; Kopp & Pneuman, 1976). A schematic cartoon of this model is shown in Figure 1.3. In this model, reconnection occurs at the cusp of magnetic loops in the solar (or stellar) corona. Electrons are accelerated both toward and away from the surface. Those that move toward the surface may radiate non-thermal gyrosynchrotron radiation as the electrons spiral around magnetic field lines (see Section 1.3.3). The high-energy electrons impact the chromosphere, producing hard X-ray emissions, and energising the chromospheric plasma, resulting in enhancements of chromospheric emission lines (e.g. H α, Ca II H & K). Chromospheric material is heated and expands into the corona, where it radiates thermally in soft X-rays. This is known as *chromospheric evaporation*, and is the underlying principle behind an observational phenomenon called the *Neupert effect* (Neupert, 1968). This effect relates the time integral of the radio luminosity to the soft X-ray luminosity:

$$\int_0^t L_R(t')dt' \propto L_X(t) \ . \tag{1.1}$$

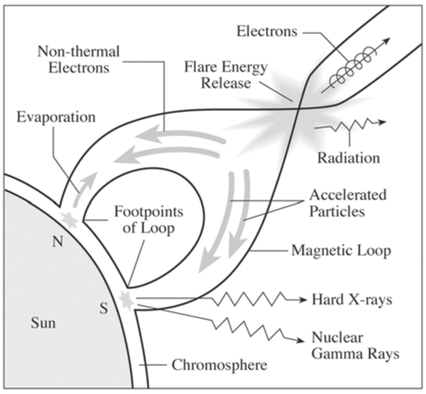

Figure 1.3: Simplified cartoon schematic of the CSHKP flare model, from Lang (2006). Flare energy is converted into radiation and acceleration of non-thermal electrons, which produce non-thermal gyrosynchrotron radio emission. The accelerated particles impact and heat the chromospheric material, which evaporates, leading to thermal soft X-ray emission. Image credit: Lang (2006).

Physically, this effect arises because the radio emission traces energy deposition by high-velocity electrons into the chromosphere, and the soft X-ray emission traces energy released from the chromosphere (via thermal processes) after energisation by electrons accelerated by the reconnection event. The operation of the Neupert effect has been observed in both solar and stellar flares Benz & Güdel (2010); Güdel et al. (2004); Dennis & Zarro (1993). An illustration of the Neupert effect is shown in Figure 1.4.

The first stellar flares were reported by van Maanen (1940) and Luyten (1949), and stars across the HR diagram are now known to exhibit flares (Pettersen, 1989). Compared to the solar counterparts, stellar flares (particularly from active M-dwarfs) are capable of releasing much more energy, and are also capable of lasting longer than solar counterparts (Benz & Güdel, 2010). However, stellar flares also exhibit many important similarities with solar flares (Haisch et al., 1991), such as temporal morphology in optical light-curves, and the observation of the Neupert effect occurring in association with stellar flares (e.g. Hawley et al., 1995; Guedel et al., 1996; Güdel et al., 2002a). Steady H α and soft X-ray emission from active stars can be explained within the CSHKP flare paradigm, through ongoing chromospheric evaporation caused by numerous small flare events operating quasi-continuously. These features are therefore often used as a tracer for stellar activity levels (e.g. Mohanty & Basri, 2003).

An important empirical trend in active stars, known as the Güdel-Benz relation (Gudel et al., 1993; Benz & Guedel, 1994), shows that there is a close relationship between the soft X-ray luminosity and the non-thermal radio luminosity of active stars. The trend, incorporating data from solar and stellar observations, can be described by a power-law relationship (Benz & Guedel, 1994):

$$L_X \propto L_{\nu,R}^{0.73\pm0.03} \tag{1.2}$$

where L_X and $L_{\nu,R}$ are the X-ray and radio luminosities, respectively. This relationship arises from the same origin as the Neupert effect – namely, a close causal relationship between non-thermal electrons accelerated by magnetic reconnection in flares, which generate radio emission via the gyrosynchrotron mechanism (see Section 1.3.3); and the thermal electrons which are heated in the chromosphere by the non-thermal electrons and evaporate into the corona, where they radiate in soft X-rays. This empirical relationship holds over nearly 10 orders of magnitude in luminosity, and in a broad range of active stars, illustrating the wide applicability of the CSHKP paradigm. Instances when the Güdel-Benz relation is violated indi-

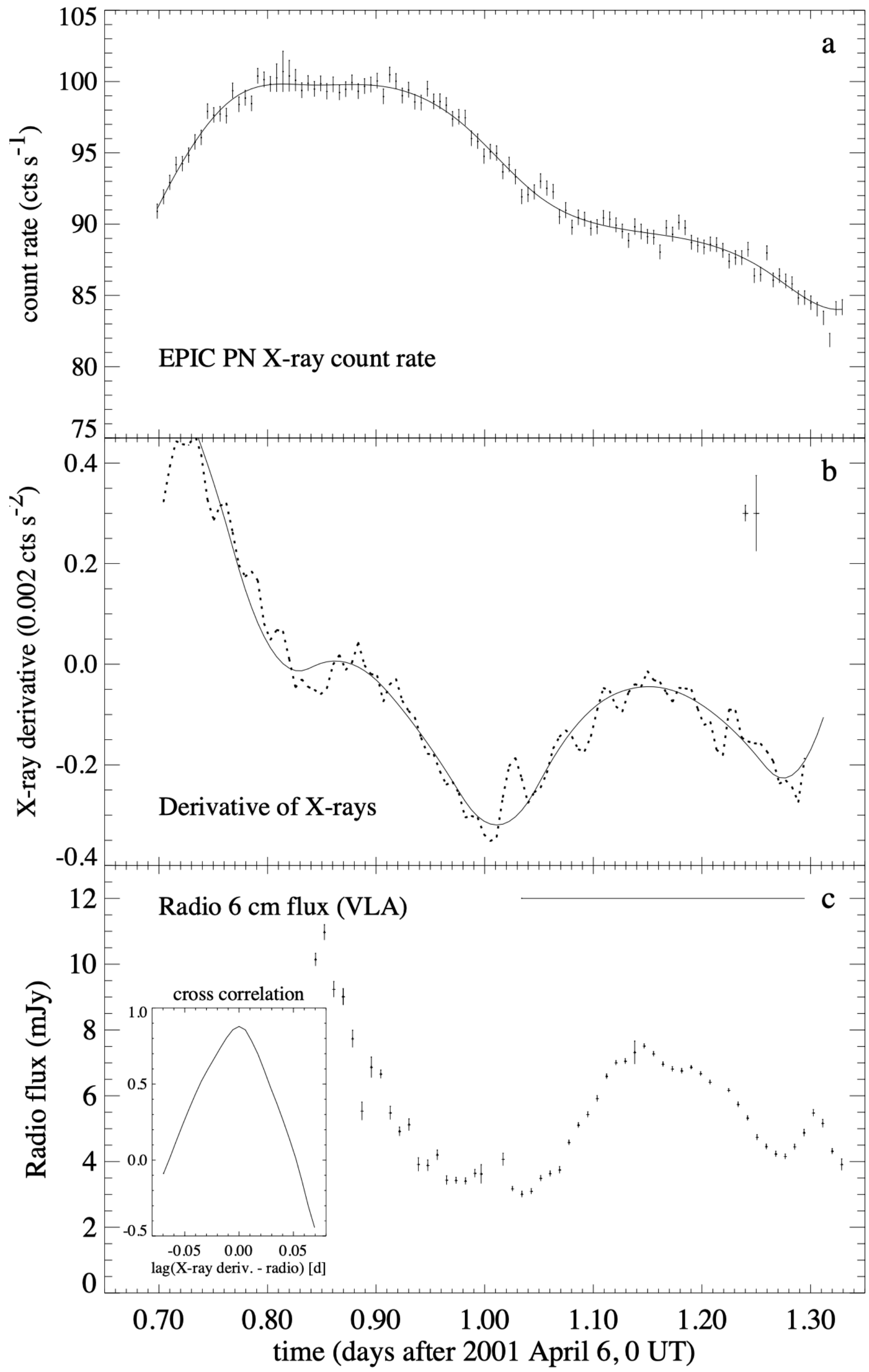

Figure 1.4: X-ray light-curve (a), X-ray light-curve time derivative (b), and 6 cm radio light-curve (c) of a flare on the RS Canum Venaticorum (interacting close binary system) σ Gem, from Güdel et al. (2002b). The radio light-curve follows the X-ray time derivative closely, as expected from the Neupert effect. The cross-correlation between the X-ray time derivative and the radio light-curves is inset in sub-figure (c). Image credit: Güdel et al. (2002b).

cate the operation of a non-standard flare paradigm (e.g. Osten et al., 2005), or a fundamentally distinct process at work, particularly when coherent radio emission is involved e.g. auroral radio emission from brown dwarfs (Hallinan et al., 2015), or coherent bursts from M-dwarfs unassociated with flaring activity (Kundu et al., 1988).

Space weather

Related to flares is the family of phenomena collectively known as *space weather*, which describes the conditions of the magnetised plasma beyond the stellar corona (Schwenn, 2006). This includes:

- the stellar wind – a steady outflow of diffuse, supersonic plasma from the corona (Cranmer & Winebarger, 2019);
- energetic particle events (Schwenn, 2006) – beams of relativistic particles accelerated in the corona, travelling out into interplanetary space; and
- coronal mass ejections – powerful expulsions of magnetised plasma from the corona (Webb & Howard, 2012).

Like flaring activity, space weather ultimately results from the generation, stochastic movement, and reconfiguration of magnetic fields. Flaring and space weather activity are often (but not always) closely related.

Coronal mass ejections are the most significant space weather phenomenon of those outlined above, with the potential to severely impact companion objects. Statistical studies with large samples of solar CMEs have shown that they have masses ranging from 10^{13}–10^{16} g, speeds of $\sim$ 200–2000 km s^{-1}, and have total energies of 10^{27}–10^{33} erg (Vourlidas et al., 2002; Gopalswamy, 2004). These events have the potential to cause great damage to spacecraft, space personnel, and ground-based electricity networks over large areas, and subsequently may endanger human safety and cause economic loss (Cliver & Dietrich, 2013; Committee on the Societal and Economic Impacts of Severe Space Weather Events, 2008; Tsurutani et al., 2003). Attempts to understand and make predictions about solar space weather and CMEs are therefore a key areas in current solar research (Schwenn, 2006).

Solar CMEs are typically identified in white-light coronagraph or heliospheric imager observations (see Webb & Howard, 2012, for a review). Low-frequency radio emission also provides a useful window into this phenomenon – an early example came from Riddle (1970), who detected an outward-moving radio source with the Culgoora Radioheliograph at 80 MHz, likely generated by a CME. Solar radio bursts, such as type IV and shock-driven type II bursts, can also indicate CME activity (Salas-Matamoros & Klein, 2020; Gopalswamy, 2006; Robinson, 1986). Figure 1.5 shows an example of a CME-associated solar type II and IV burst from the Green Bank Solar Radio Spectrometer (White, 2007). In Chapter 4, we report the detection of a solar-like type IV burst associated with a large flare. This detection is indicative of a CME leaving the star, and ongoing electron acceleration associated with post-eruptive magnetic structures (Salas-Matamoros & Klein, 2020; Cliver et al., 2011).

Interest in the space weather environment around active stars has increased in recent years, driven by the growing population of confirmed extrasolar planets, and

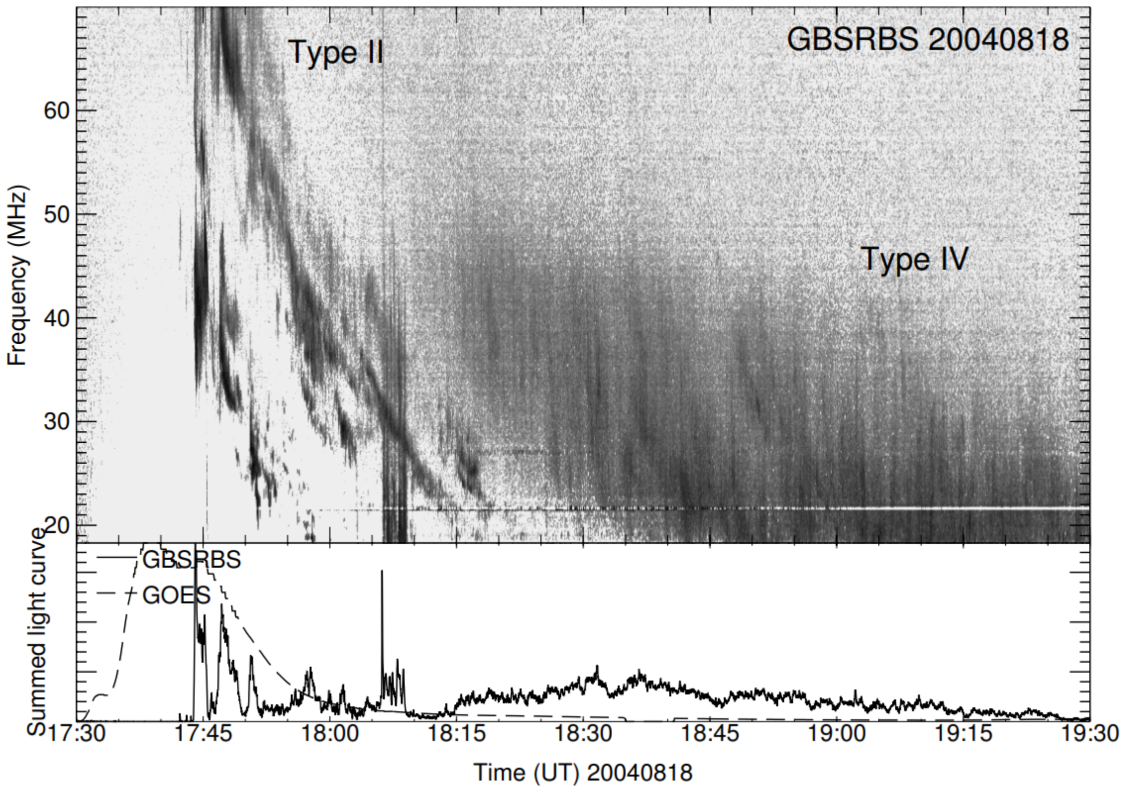

Figure 1.5: Dynamic spectrum (showing intensity as a function of frequency and time) of type II and IV solar radio bursts observed with the Green Bank Solar Radio Burst Spectrometer (GBSRBS). A type II burst appears as a slowly drifting pair of lanes through the dynamic spectrum beginning at about 17:45 UT. A low-frequency type IV burst, appearing as a more smooth, finely-structured and slow-drifting burst follows the type II burst, commencing at about 18:15 UT. The nearly-vertical features appearing around 18:07 UT are a group of type III bursts. The bottom panel shows the frequency-averaged GBSRBS intensity (solid line), and the soft X-ray flux measured by the GOES satellite (dashed line), showing the occurrence of a flare associated with these bursts. Figure from White (2007).

the need to empirically constrain the habitability of planets around active stellar hosts (Khodachenko et al., 2007). There have been several observational searches for stellar CMEs, with only one confirmed event reported thus far (Argiroffi et al., 2019). There have also been several candidate events identified through blue-shifted Balmer line components (Houdebine et al., 1990; Vida et al., 2019a, e.g.), and ongoing X-ray absorption during flares (Moschou et al., 2017, 2019, e.g.). However, these candidates may also be produced solely by flaring phenomena, such as filament eruptions. To date, there have been no confirmed CMEs from active M-dwarf stars. Searches for type II burst emission at low radio frequencies have returned nil detections (Crosley et al., 2016; Crosley & Osten, 2018a,b; Villadsen & Hallinan, 2019). Numerical modelling by Alvarado-Gómez et al. (2018) has shown that large-scale strong overlying magnetic fields may prevent CME escape from M-dwarf coronae. Those that are able to escape the strong M-dwarf magnetosphere may not produce shocks at appropriate electron densities due to high Alfvén speeds, preventing the production of type II emission because there is no shock (Alvarado-Gómez et al., 2020; Mullan & Paudel, 2019).

Auroral processes

Aurorae are prevalent in the magnetised planets of the solar system, including on Earth, where they manifest as the famous terrestrial *Aurora Australis* and *Aurora Borealis*. As discussed below, studies in the last two decades have revealed that aurorae are also present in a number of ultra-cool dwarfs (UCDs; spectral type > M7), and in magnetically chemically-peculiar (MCP) stars.

Aurorae are driven by large-scale field-aligned current systems, which can be produced in several ways. Firstly, interaction between the object's magnetosphere and a flow of magnetised plasma can cause magnetic reconnection events, accelerating the plasma along magnetic field lines toward the polar regions. This is the mechanism responsible for the aurorae on Earth and Saturn, whose magnetospheres interact with the solar wind (e.g. Cowley et al., 2004). Secondly, orbit of a satellite through a magnetosphere sets up a current system within the magnetic flux tube connecting the satellite and the parent body. This mechanism operates in the jovian magnetosphere with its moons Io, Europa and Ganymede (Saur et al., 2013; Zarka, 1998; Bigg, 1964; Goldreich & Lynden-Bell, 1969), and in the cronian magnetosphere with Enceladus (Tokar et al., 2006). Figure 1.6 shows an ultraviolet image of the jovian auroral oval, which features "hotspots" corresponding to the footpoints of magnetic flux tubes connected with Io, Ganymede, and Europa. Finally, breakdown of rigid co-rotation between the magnetosphere and a rotating plasma disk sets up magnetosphere-ionosphere coupling currents, which act as the auroral current system (Cowley & Bunce, 2001). This mechanism is responsible for the jovian main auroral oval. As is the case with Jupiter, the mechanisms described above are not necessarily mutually exclusive.

The large-scale current systems driving aurorae are responsible for a wide variety of emissions when the high-energy particles impact the neutral atmosphere (see Figure 1.6). These include the well-known optical emission in Earth's atmosphere, and ultra-violet, optical, and infrared emission on Jupiter and Saturn (e.g. Vasavada et al., 1999; Clarke et al., 1996; Caldwell et al., 1980). Aurorae can also generate

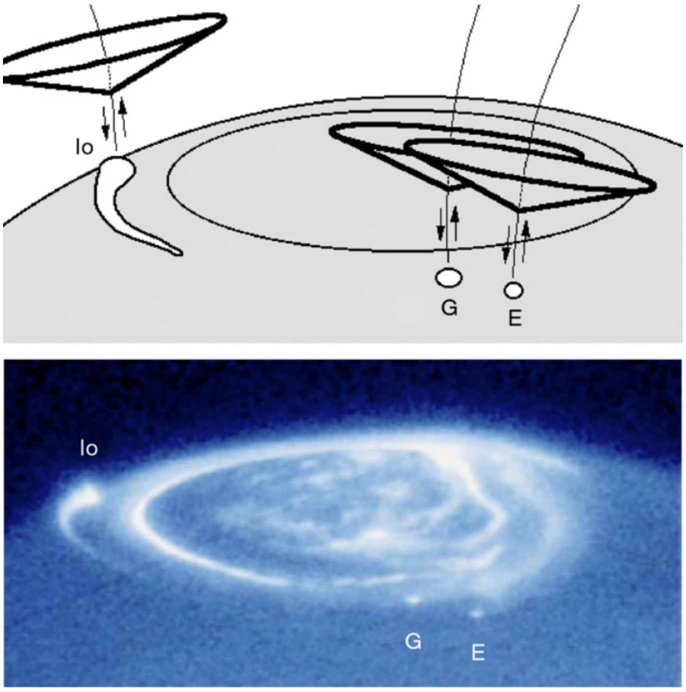

Figure 1.6: *Top*: cartoon illustration showing the geometry of jovian auroral radio emission from the magnetic flux tubes connected with the moons Io, Ganymede (G), and Europa (E). The emission is highly beamed in a thin cone at a large angle (> 70°) from the magnetic field.*Bottom*: Hubble Space Telescope ultraviolet image of the the northern jovian auroral region, showing the full auroral oval along with the "footprints" of the Io, Ganymede and Europa magnetic flux tubes. Figure from Zarka (2007).

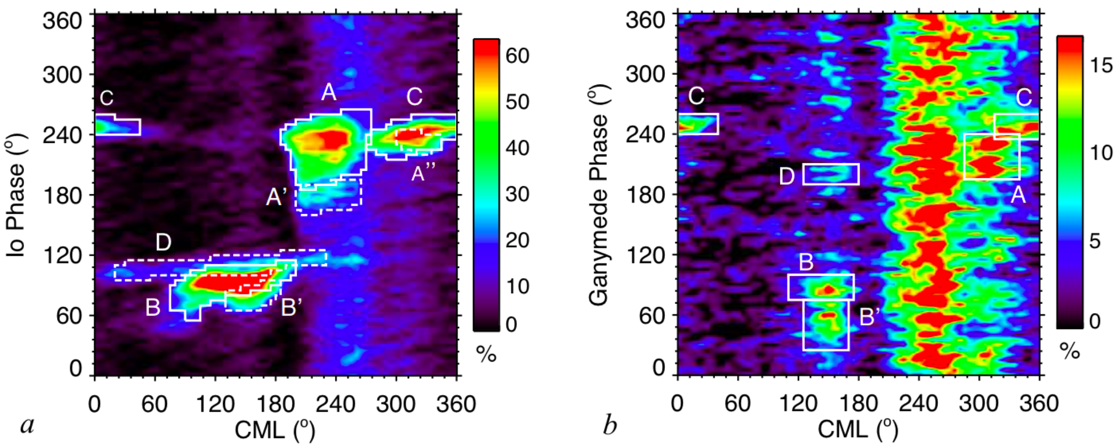

Figure 1.7: Occurrence probability of jovian radio emission as a function of central meridian longitude (CML) and satellite orbital phase, for Io and Ganymede, compiled from 26 years of observations. Localised patches in this phase space correspond with emission from an excited flux tube crossed by a satellite. Vertical features reveal stationary magnetic features which are responsible for some of the radio emission. Figure from Zarka et al. (2018).

extremely powerful radio emissions: at frequencies below 20 MHz, radio emission from the jovian aurorae are more intense than the quiescent Sun (Zarka, 1998). The radio emission is produced through the electron cyclotron maser instability, which we discuss in detail in Section 1.3.4.

An important feature of this emission is that it is highly directional, with emission occurring in a hollow cone nearly perpendicular to the magnetic field (Treumann, 2006). The exact emission geometry depends on the electron velocity distribution anisotropy driving the maser – see Section 1.3.4. As a result, the emission can be rotationally modulated as the beamed emission crosses the line of sight, in a similar fashion to a pulsar. Figure 1.6 illustrates the beamed radio emissions produced in the magnetic flux tubes connected to its satellites Io, Europa and Ganymede. Depending on the driver of the aurorae, the beamed emission can generate periodic pulses at the rotational period of the source object, at the orbital period of a satellite, or remain quasi-stable if the emission originates from a full auroral oval.

Figure 1.7 shows the probability of observing a jovian auroral radio burst as a function of jovian central meridian longitude (CML) and the orbital phase of Io, and Ganymede. The vertical stripe near a CML of 250° is indicative of an emission region that remains fixed in jovian longitude, producing bursts that are periodic with the jovian rotation. The localised patches of high probability, outlined and labelled A, B, C, and D in either sub-figure, correspond with emission features that occur near a fixed satellite orbital phase and at favourable jovian longitudes. This is an example of emission that is rotationally modulated by the orbital period of the satellite along with the rotation of the object. In this way, the presence of periodic or rotationally-modulated radio emission is the hallmark of aurorae operating within a magnetosphere.

The observation of periodic radio pulses from the ultra-cool dwarf TVLM 513−46546 (Hallinan et al., 2006, 2007, see Figure 1.8), and later from several other ultra-cool dwarfs (e.g. McLean et al., 2011; Berger et al., 2009; Hallinan et al., 2008) suggests that auroral processes are capable of operating in low-mass stars with fully-convective dynamos (Hallinan et al., 2015). Following this discovery, rotationally-modulated optical emission (both continuum and in H α emission) has been observed and attributed to the same underlying auroral mechanism driving the periodic radio pulses (Harding et al., 2013; Hallinan et al., 2015). To date, none of the radio-loud ultra-cool dwarfs have exhibited periodicity distinct from their known rotational period, which would be a hallmark of the interaction between the star and a companion planet. The most plausible driver for ultra-cool dwarf aurorae is breakdown of co-rotation of a plasma disk and the magnetosphere, but the nature of the auroral engine is as yet, unconfirmed (Hallinan et al., 2015; Pineda et al., 2017).

Aside from ultra-cool dwarfs, auroral radio emissions have also been observed in hot magnetic stars. The first example was CU Virginis, which was observed to produce periodic radio pulses by Trigilio et al. (2000). For more than a decade, CU Virginis was the only known hot magnetic star to exhibit this behaviour, but analogous examples have also been recently uncovered (e.g. Leto et al., 2018; Das et al., 2018, 2019a,b).

That some ultra-cool dwarfs and hot magnetic stars exhibit aurorae may be a consequence of their stable, large-scale, rotation-dominated magnetospheres, similar to

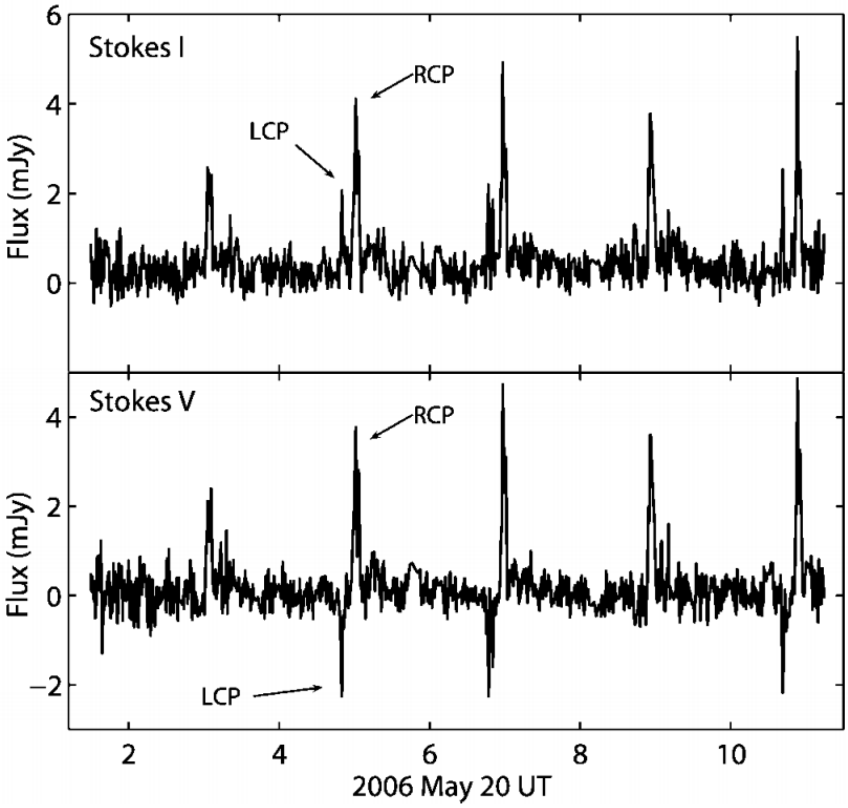

Figure 1.8: Auroral radio pulses from the ultra-cool dwarf TVLM 513−46546. The top panel shows Stokes I (total intensity), and the bottom panel shows Stokes V (circularly polarised intensity). The periodic and highly polarised nature of the pulses is evident. From Hallinan et al. (2007).

the planetary magnetospheres which also host aurorae. The presence of aurorae on ultra-cool dwarfs, implying the existence of a large scale magnetic field, is consistent with fully-convective dynamo modelling by Yadav et al. (2016, 2015), which shows that dynamos in rapidly-rotating (low Rossby number) fully-convective stars produce stable, axisymmetric fields, whereas more slowly-rotating (higher Rossby number) fully-convective stars produce more complex, cyclic magnetic field structures. However, it remains unclear how common this phenomenon may be in fully or even partially-convective main sequence stars, which likely exhibit activity more consistent with the solar paradigm.

1.2 The influence of stellar magnetic activity

Magnetic activity has a significant influence in most aspects of the life of a star, such as its formation, evolution, chemical enrichment, and on its environment (Donati & Landstreet, 2009). Below we discuss some effects which strongly influence the evolution of, and environment around main-sequence low-mass stars.

1.2.1 Mass loss and angular momentum evolution

Mass loss and angular momentum evolution hold a two-way relationship with the magnetic activity of low-mass stars. Mass loss of active stars can arise from two main components – the stellar wind, and coronal mass ejections. An important distinction is that the wind is steady, so is a constant source of mass loss, whereas coronal mass ejections are transient in nature, only causing mass loss in isolated episodes.

Mass loss on the Sun is dominated by the solar wind, with coronal mass ejections only contributing a few percent to the total mass-loss rate of $\sim 10^{-14}\,\mathrm{M}_\odot\,\mathrm{yr}^{-1}$ (Vourlidas et al., 2010). However, statistical studies of solar flares and related CMEs have revealed an empirical correlation between solar X-ray flare energy and CME mass (Drake et al., 2013; Aarnio et al., 2012). This raises the possibility that coronal mass ejections may be a significant source of mass loss on active stars, which flare more frequently and more powerfully than the Sun (Osten & Wolk, 2015; Lacy et al., 1976; Benz & Güdel, 2010). Drake et al. (2013) estimate a CME-driven mass-loss rate of up to $10^{-11}\,\mathrm{M}_\odot\,\mathrm{yr}^{-1}$ for active stars, orders of magnitude higher than the solar rate. Aarnio et al. (2012) reached similar conclusions, finding mass loss rates in the range of 10^{-12}–$10^{-9}\,\mathrm{M}_\odot\,\mathrm{yr}^{-1}$. Using energy partitions between various radiative components of solar flares and CMEs, Osten & Wolk (2015) derived CME-driven mass-loss rates for active stars finding they were generally orders of magnitude greater than the solar mass-loss rate. However, the true occurrence frequency of CMEs on active stars is currently unknown, and so the assumption of a solar-like CME scaling relationship cannot be verified and may not hold. Simulations of CMEs from active stars suggest that a strong overlying magnetic field may suppress CMEs, diminishing the influence of this phenomenon on stellar mass loss (Alvarado-Gómez et al., 2018, 2019). These results, and the current lack of strong observational constraints on stellar CMEs (Leitzinger et al., 2011, 2020; Crosley et al., 2016; Crosley & Osten, 2018a,b; Villadsen & Hallinan, 2019; Vida et al., 2019a; Leitzinger et al., 2020), necessitate further observational campaigns for transient mass loss from a broad range of active stars.

The angular momentum evolution of active stars is also closely related with the operation of stellar activity. Skumanich (1972) established that as isolated main-sequence stars age, their rotational velocity decays in proportion to $t^{-1/2}$, demonstrating ongoing angular momentum loss throughout the majority of a star's life. This spin-down is thought to be driven by mass loss from the magnetised stellar wind, which applies magnetic stresses on the rotating star (e.g. Weber & Davis, 1967). Aarnio et al. (2012) found that CME activity can be a significant driver of angular momentum loss in pre-main sequence stars, and CME activity on main-sequence stars is likely to have a similar effect (Osten & Wolk, 2015).

In addition to angular momentum, activity levels tend to decrease with stellar age (Irwin et al., 2011; West et al., 2008). This trend is related to the rotation-activity relation – more rapidly-rotating stars exhibit higher activity levels (usually measured using tracers such as H α or X-ray luminosity), up until a rotation rate where activity level saturates (Mohanty & Basri, 2003; Reiners & Basri, 2008a). These trends highlight the relationship between rapid rotation and dynamos which drive the generation of magnetic fields in low-mass stars. In addition, the spin-down rate tends to decline with mass, so that lower-mass M-dwarfs retain their angular momentum for longer than solar-like stars (Gallet & Bouvier, 2015; Reiners & Basri, 2008a). This decline in spin-down rate may arise due to the increasing importance of large-scale, dipolar magnetic fields in fully-convective stars (Morin et al., 2008, 2010), compared with the more complex fields found in solar-like stars (Reiners & Basri, 2008a). For stars later than spectral type M9, the rotation-activity relation breaks down, potentially due to the emergence of a neutral atmosphere in these cool stars, which may suppress chromospheric activity such as H α emission due to high atmospheric resistivity (Mohanty & Basri, 2003).

To summarise this relationship between magnetic fields, rotation, and mass loss: young stars tend to rotate more rapidly, which favours higher activity arising from a more efficient dynamo. This magnetic activity drives the stellar wind (e.g. Mestel, 2012), and CME activity, which in turn drive stellar mass loss. Magnetic braking and angular momentum transport caused by this mass loss slow the stellar rotation, resulting in a less efficient dynamo. This in turn leads to diminishing levels of activity, setting up a negative feedback cycle between activity, mass loss, and spin down.

1.2.2 Planetary atmospheres, magnetospheres, and habitability

Along with fundamental stellar parameters such as mass and rotation rate, stellar magnetic activity also significantly influences planetary companions, through the interaction of planetary atmospheres and magnetospheres with magnetised outflows and radiation from the host star. In the solar system, the link between solar activity and geomagnetic storms and planetary aurorae has been firmly established for nearly a century (Chapman & Ferraro, 1930; Hale, 1931). Solar wind and CMEs drive aurorae throughout the entire solar system (Prangé et al., 2004; Zarka, 1998), causing ionisation of neutral atmospheric molecules. The solar wind is also capable of eroding planetary atmospheres (e.g. Lundin et al., 2007), which likely caused significant atmospheric loss in Mars and Venus, which lack a strong, shielding magnetic field similar to the terrestrial field (Lundin et al., 2007). The loss of the martian atmosphere and its water content illustrates the profound influence of stellar winds on atmospheric chemistry and therefore planetary habitability.

The traditional circumstellar “habitable zone” (HZ) is defined by the range of orbital radii where the planetary equilibrium temperature is compatible with the presence of liquid water. For cool M-dwarfs, which dominate the galactic stellar population (Henry et al., 2006), the HZ lies much closer to the host star than the solar HZ, at orbital radii of ~ 0.04–0.5 AU depending on the mass and age of the host star (Khodachenko et al., 2007). This increases the susceptibility of M-dwarf HZ planets to high levels of stellar activity. Several works using numerical simulations have investigated the influence of stellar activity and space weather on close-in exoplanets. Khodachenko et al. (2007) and Lammer et al. (2007) investigated the influence of CMEs on close-in Earth-like exoplanets around active M-dwarfs, finding that these stars are capable of exposing their companion planets to energetic CMEs throughout their entire lifetime, causing strong magnetospheric compression and subsequent

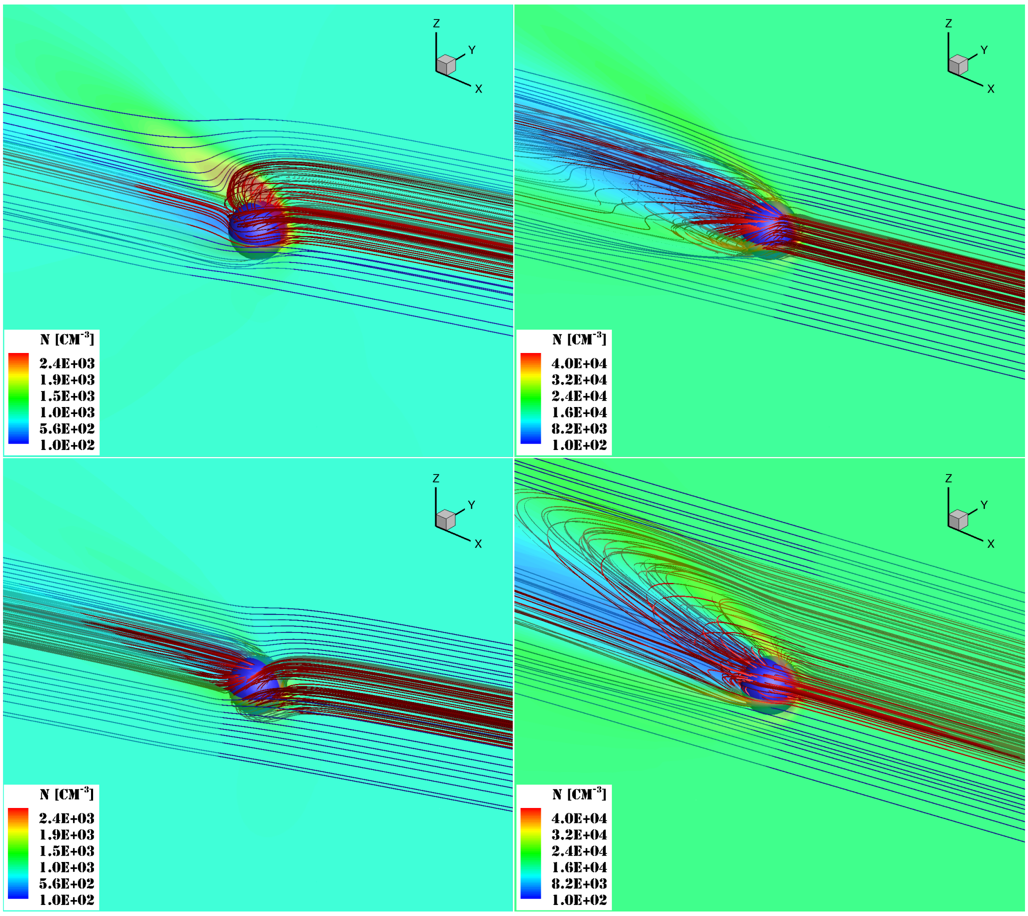

Figure 1.9: Magneto-hydrodyanamic simulation of the interaction of the planet TRAPPIST-1 f and the magnetised wind of its host star. The planet is represented by the blue sphere, and the star is located along the x-axis to the right. Top panels show simulation results for an Earth-like magnetic field, and bottom panels show results for an Earth-like field with polarity reversed. Left and right panels correspond to a sub- and super-Alfvénic wind, respectively. Magnetic field lines directly-connected to the planetary magnetosphere are shown in red, whereas nearby stellar field lines are shown in blue. The background colour indicates the wind density. The connection of the planetary magnetosphere to the stellar magnetic field acts as a conduit to the stellar wind directly onto the planetary atmosphere, causing strong erosion. Figure from Garraffo et al. (2017).

atmospheric erosion by these space weather events. The effects of a stellar wind have also been investigated in detail by Garraffo et al. (2016) and Garraffo et al. (2017) for Proxima Centauri b (Anglada-Escudé et al., 2016) and the TRAPPIST-1 planetary system (Gillon et al., 2017) respectively. They find wind pressures on the planetary atmospheres exceeding the solar wind pressure on Earth by a factor of 10^3–10^5, leading to strong atmospheric erosion and variable magnetospheric compression. In the case of the TRAPPIST-1 system, magnetic field lines from the star may connect with the planetary magnetosphere, providing a direct conduit of the stellar wind onto the planetary atmosphere. This is illustrated in Figure 1.9. In a similar vein, Vidotto et al. (2013) have shown that magnetic pressure alone may reduce the size of planetary magnetospheres, leaving them susceptible to erosion. A somewhat less frightening scenario is presented by Vidotto & Cleary (2020), who argue that strong pressure from stellar winds around close-in planets may actually confine their atmospheres from escape, rather than eroding them. In addition to magnetospheric compression, stellar winds may form magnetospheric bow shocks, and drive auroral radio emission from strongly-magnetised exoplanets (Vidotto et al., 2015).

Ongoing exposure to energetic particles ($> 10\,\mathrm{MeV}$) and high levels of ionising radiation from flaring activity may also have an important influence on planetary atmospheres and habitability. Howard et al. (2018) reported the detection of a superflare (a flare with bolometric energy exceeding $10^{33}\,\mathrm{erg}$) from Proxima Centauri. They found that repeated exposure to energetic particle events from the repeated flares from Proxima Centauri may deplete atmospheric ozone, leaving simple surface life susceptible to intense far-ultraviolet radiation produced by superflares (Howard et al., 2018). These conclusions are similar to the study of Segura et al. (2010), who find that the strong far-ultraviolet radiation from stellar flaring alone does not significantly impact habitability for surface life in an Earth-like atmosphere, but ongoing exposure to energetic protons associated with flaring may remove atmospheric ozone, leaving the surface susceptible to ionising radiation.

Although the above works may paint a threatening picture for the habitability of M-dwarf exoplanets, the key ingredient that is still missing is direct observational evidence of the response of exoplanet atmospheres and magnetospheres to the space weather environment created by its host star. The next generation of large-scale astronomical facilities, such as the Square Kilometre Array, and the James Webb Space Telescope, may provide long-sought observational constraints on these topics.

1.3 Stellar radio emission processes

Stellar atmospheres contain an abundance of plasma which is subject to thermal processes, and forces primarily from electric and magnetic fields. Accelerated electrons within a plasma produce electromagnetic radiation at radio wavelengths, and as a result, stellar atmospheres are a natural place to expect radio emission. This is demonstrated by the detection of radio emission from a wide variety of stars across the Hertzprung-Russell diagram. Radio emission is driven by, and carries important information about the plasma in stellar magnetospheres. It is therefore an important probe into stellar coronae, providing information that is complementary to other wavebands and techniques.

Basic phenomena responsible for accelerating individual electrons include thermal free-free collision (bremsstrahlung), or gyration around magnetic field lines due to the Lorentz force. These processes result in *incoherent* emission – the population of electrons do not gyrate or collide in phase, and so the ensemble of emission from the electrons is not in phase. In more special circumstances involving plasma instabilities or resonances, described in Section 1.3.4 below, *coherent* emission is produced. This emission can be extremely bright, highly polarised, and exhibit complex time-frequency structure.

The plasma environment and physical processes driving the emission leave signatures on the observable parameters, such as temporal variability, spectral structure, polarisation, luminosity, and brightness temperatures. Observing these parameters provides a means for remote sensing of the plasma environment in stellar atmospheres, and for inferring the physical processes operating in stellar atmospheres. This makes stellar radio emission an effective probe of stellar atmospheres, and the physical processes operating within them.

Before a detailed description of the important radio emission mechanisms, it is useful to introduce key concepts that will aid our understanding of these mechanisms. Firstly, it is useful to introduce the characteristic frequencies of the magnetised plasmas which produce radio emission. These are the electron plasma frequency

$$\nu_p = \left(\frac{e^2 n_e}{\pi m_e}\right)^{1/2} \approx 9.0\, n_e^{1/2}\,\mathrm{kHz}, \tag{1.3}$$

and the electron cyclotron frequency:

$$\nu_c = \frac{eB}{2\pi m_e c} \approx 2.8\, B\,\mathrm{MHz}\,. \tag{1.4}$$

where the constants have been evaluated in Gaussian cgs units for the numerical approximations. The plasma frequency is the characteristic frequency of plasma oscillation or *Langmuir waves*, and the electron cyclotron frequency (also known as the electron gyrofrequency) is the rotation frequency of the gyrating electrons. These frequencies are often described in terms of their angular frequencies, i.e. $\omega_p = 2\pi\nu_p$, $\omega_c = 2\pi\nu_c$. Which of these two frequencies dominates the other is a key factor in which radiative processes can operate, and which are quenched. It is also worth noting that the contribution of ions is usually neglected, since their high mass compared to electrons means that they are not accelerated as much by electromagnetic forces.

Before proceeding to discuss emission mechanisms in detail, it is useful to outline some fundamentals of radiation in a stellar context. Further details for the following Sections 1.3.1 and 1.3.2 can be found in textbooks such as Melrose (1986), Aschwanden (2005), Koskinen (2011), and Condon & Ransom (2016).

1.3.1 Magnetoionic modes and polarisation

Stellar radio emission arises from, and propagates through, a magnetised plasma. The magnetic field of the plasma causes *birefringence*, i.e. refractive indices which depend on the wave polarisation. The radiation is subject to the plasma dispersion equation, whose solutions depend on the geometry of the wave-vector, electric field and magnetic field. These solutions define the magneto-ionic modes of the plasma. The derivations of these solutions is quite involved, but a common simplification is to take the *cold plasma approximation*. This approximation assumes that the wave group velocity is assumed to be much greater than the thermal velocity of the electrons, and the contribution of massive ions are neglected.

The most important modes are those where the waves are able to escape the plasma as freely-propagating electromagnetic radiation (i.e. radio waves). These are known as the *ordinary* (o) and *extraordinary* (x) modes. The name of the ordinary mode reflects that its dispersion relation is independent of the background magnetic field when the radiation wave vector is perpendicular to the magnetic field, so this mode describes the propagation in the absence of a magnetic field. The refractive index of the extraordinary mode differs from the ordinary mode due to the influence of the magnetic field.

In most cases, the so-called *quasi-circular* approximation applies (Melrose, 1986), which implies that o and x-mode radiation are 100% circularly polarised in opposite senses. The electric field vector of radiation in the x-mode rotates in the same direction as the electron gyromotion, while for o-mode the electric field rotation is opposite to the gyromotion. As a result, x-mode radiation is right-hand circularly polarised (RCP) if emitted from the magnetic north polar region of a radiation source, and left-hand circularly polarised if emitted from a magnetic south polar region. The opposite is true for o-mode radiation, i.e. emission from a magnetic south will be RCP, and emission from a magnetic north will be LCP.

A net polarisation is produced when radiation from different modes have different intensities. If a detector can measure the polarisation state of incoming radiation, then it can be used as a powerful diagnostic of the radiation source and its propagation path. For example, if the magnetic field direction at the source can be determined independently (for example, through *Zeeman Doppler Imaging*), the handedness of the circular polarisation is indicative of the magneto-ionic mode of the radiation, and therefore of the emission mechanism. On the other hand, if the emission mechanism is known, then the polarisation handedness gives insights into the magnetic field structure at the source.

Propagation effects can also influence the polarisation of the radiation, potentially transferring information about the medium to a distant observer. For example, the distinct refractive indices for the x and o-modes of a magnetised plasma causes the polarisation angle of linearly polarised radiation ϕ to rotate as it propagates through the medium. When the electron cyclotron frequency is much smaller than the emission frequency ($\omega_c \ll \omega$), the rate of rotation can be expressed as:

$$\frac{d\phi}{ds} = -\frac{\omega_p^2 \omega_c}{2c\omega^2} = -\frac{e^3}{2\pi m_e^2 c^4}\lambda^2 n_e B_{\parallel}\,. \tag{1.5}$$

This effect is known as *Faraday Rotation*, and is widely used to probe the magnetic fields of radio galaxy lobes and AGN (e.g. O'Sullivan et al., 2017), galaxies (Beck, 2015), and the Milky Way interstellar medium (e.g. Oppermann et al., 2015), enabling a broad range of scientific investigations (e.g. Heald et al., 2020). Defining the *rotation measure* (RM),

$$\mathrm{RM} = \frac{e^3}{2\pi m_e^2 c^4} \int_d^0 n_e(s) B_\parallel(s) ds \,, \tag{1.6}$$

the total rotation of the polarisation plane can be expressed

$$\phi = -\mathrm{RM}\,\lambda^2 \,, \tag{1.7}$$

which means that the rotation measure can be determined by wide-band polarimetric radio observations. Under typical conditions in stellar coronae, the magnetic field is relatively strong ($\sim$ 1–1000 G), and the plasma is dense ($\sim 10^7$–$10^{10}\,\mathrm{cm}^{-3}$) (Yang et al., 2020; Morin et al., 2010; Ness et al., 2004). These conditions mean that Faraday rotation occurs rapidly enough for *bandwidth depolarisation*, when the polarisation angle rotates significantly within one frequency channel, so that the polarisation information is lost. In addition, the coronal magnetic field strength and electron density are strongly inhomogeneous, and as a result, the value of the rotation measure varies strongly throughout the corona. If the spatial extent of the radiation source is sufficiently large, then emission from different depths along the line of sight are subject to different degrees of Faraday rotation – this is termed *differential Faraday rotation*, and is an intrinsic depolarisation process. Similarly, variations in the rotation measure orthogonal to the line of sight, but on angular scales smaller than the angular resolution of the telescope cause *beamwidth depolarisation*. These depolarisation effects are expected to be strong for stellar radio sources, so linear polarisation is not expected to detectable from stellar coronae – see Sokoloff et al. (1998) for a review of Faraday depolarisation effects. In Chapters 3 and 4, we present observations of linearly polarised emission from UV Ceti and Proxima Centauri respectively, and explain the polarisation features in terms of emission from extremely rarefied cavities within the stellar magnetosphere.

Another propagation effect, mode coupling, may cause reversals in the sense of circular polarisation, and conversion between the magneto-ionic modes as the radiation propagates. This is thought to be particularly important in so-called quasi-transverse regions, where the magnetic field is perpendicular to the direction of propagation. For example, Shaposhnikov et al. (1997) argued that the elliptical polarisation of Jovian decametric emission arose due to linear mode coupling, rather than intrinsically elliptically polarised emission produced from a highly rarefied source region (Melrose & Dulk, 1991). White et al. (1992) provide an overview of mode coupling theory, and discuss its relevance in radio observations of the solar corona.

1.3.2 Brightness temperature and radiative transfer

The specific intensity describes the power dP received from a radiating source with solid angle $d\Omega$, at an angle θ from the normal to a surface area $d\sigma$, in a small frequency range $d\nu$ around frequency ν. It is defined as

$$I_\nu \equiv \frac{dP}{\cos\theta d\sigma d\Omega d\nu} \,, \tag{1.8}$$

and has units of $\mathrm{erg\,s^{-1}\,cm^{-2}\,Hz^{-1}\,sr^{-1}}$. In a vacuum, the specific intensity from an isolated point source I_ν is conserved along a ray s:

$$\frac{dI_\nu}{ds} = 0. \tag{1.9}$$

In the case of propagation through a medium, absorption and emission may occur along the ray path. We define the absorption coefficient κ as the constant of proportionality of the infinitesimal probability dP of a photon being absorbed in a slab of thickness ds:

$$dP = \kappa ds\,. \tag{1.10}$$

The corresponding fractional change in intensity is therefore

$$\frac{dI_\nu}{I_\nu} = -\kappa ds\,. \tag{1.11}$$

Integrating both sides along the intervening medium yields

$$\ln\left(\frac{I_\nu(s_{\mathrm{out}})}{I_\nu(s_{\mathrm{in}})}\right) = -\int_{\mathrm{in}}^{\mathrm{out}} \kappa(s')ds' \tag{1.12}$$

for a purely absorbing medium. Exponentiating both sides, and defining the *optical depth*

$$\tau \equiv \exp\left(\int_{\mathrm{in}}^{\mathrm{out}} \kappa(s')ds'\right)\,, \tag{1.13}$$

the fractional decrease in specific intensity after propagating through an absorbing medium is

$$\frac{I_\nu(s_{\mathrm{out}})}{I_\nu(s_{\mathrm{in}})} = \exp(-\tau)\,. \tag{1.14}$$

For $\tau \ll 1$, the absorption becomes negligible, and the emission is called *optically thin*. For $\tau \gg 1$, absorption is significant along the ray path and the emission is called *optically thick*. Note that $\tau \geq 0$ in general[1].

Similarly, a medium may emit a photon which will contribute positively to the specific intensity along an infinitesimal ray path, which can be characterised by the emission coefficient j_ν:

$$dI_\nu = j_\nu ds\,. \tag{1.15}$$

Considering both emission and absorption, we obtain the radiative transfer equation

$$\frac{dI_\nu}{ds} = -\kappa_\nu I_\nu + j_\nu\,. \tag{1.16}$$

An important characteristic of any radio emission is the brightness temperature. This is the temperature of a black body of a given size radiating via Planck's law, whose specific intensity matches the observed specific intensity of the source, even if

[1] Except for molecular maser sources which produce stimulated emission (i.e. negative absorption; $\tau < 0$) at specific wavelengths corresponding to molecular energy transitions. (Reid & Moran, 1981).

the source is not a black body. At low frequencies, when $h\nu/kT \ll 1$, the Rayleigh-Jeans approximation holds and the expression for black body radiation becomes

$$B_\nu(T) = \frac{2k_B T\nu^2}{c^2}\,. \tag{1.17}$$

The definition of brightness temperature T_b follows directly from the Rayleigh Jeans approximation, and is used to characterise the specific intensity even when emission is non-thermal (i.e. when $I_\nu \neq B_\nu$):

$$I_\nu = \frac{2k_B T_b \nu^2}{c^2} \tag{1.18}$$

so that

$$T_b = \frac{I_\nu c^2}{2k_B \nu^2} \tag{1.19}$$

for any I_ν.

For ray propagation in local thermodynamic equilibrium (LTE), $dI_\nu/ds = 0$, and $I_\nu = B_\nu(T)$. From Equation 1.16, it follows that

$$\frac{j_\nu}{\kappa_\nu} = B_\nu(T) \;\; \text{(Kirchoff's Theorem)}. \tag{1.20}$$

This relation ties together the emission and absorption coefficient of any gas, at any frequency and temperature, so long as the medium is in LTE. Noting this, we define the *source function*:

$$J_\nu = \frac{j_\nu}{\kappa_\nu}, \tag{1.21}$$

which equals the Planck function B_ν when the medium is in LTE. Dividing Equation 1.16 through by κ_ν then yields

$$\frac{1}{\kappa_\nu}\frac{dI_\nu}{ds} = \frac{dI_\nu}{d\tau} = -I_\nu + J_\nu\,, \tag{1.22}$$

since $d\tau = \kappa_\nu ds$. Introducing the *effective temperature* of the radiating electrons $T_{\rm eff}$, we can express the source function J_ν as

$$J_\nu = 2\frac{k_B \nu^2 T_{\rm eff}}{c^2}\,. \tag{1.23}$$

We note that in non-LTE conditions, $T_{\rm eff} \neq T_{\rm phys}$, the physical temperature. Now expressing I_ν in terms of the brightness temperature T_b, we have

$$\frac{dT_b}{d\tau} = -T_b + T_{\rm eff}\,. \tag{1.24}$$

Integrating, and assuming an isolated source with constant $T_{\rm eff}$, we have

$$T_b = T_{\rm eff}(1 - \exp(-\tau)) \tag{1.25}$$

$$\approx \begin{cases} T_{\rm eff} & \text{if } \tau \gg 1 \text{ (optically thick)} \\ T_{\rm eff}\,\tau & \text{if } \tau \ll 1 \text{ (optically thin)} \end{cases}\,. \tag{1.26}$$

Equations 1.25 and 1.26 have the important implication that the brightness temperature cannot exceed the effective temperature for incoherent radiation. Under typical stellar conditions, the effective temperature does not exceed 10^9–10^{10} K, which places an upper limit on the brightness temperature for incoherent stellar radio emission (Dulk, 1985). A more conservative limit on the brightness temperature of incoherent radio sources can be placed by considering inverse-Compton absorption, which yields an upper limit of 10^{12} K (Kellermann & Pauliny-Toth, 1969). These thresholds on brightness temperature mean that it is a useful diagnostic in determining whether observed emission is coherent.

For a single polarisation, the brightness temperature of a source with flux density S_ν is

$$T_b = \frac{k_B \nu^2}{c^2} \int S_\nu d\Omega \tag{1.27}$$

where $d\Omega$ is a differential solid angle and the integral is computed over the projected area of the source. If the source size can be estimated, the measured flux density of any radio source can be used to determine the corresponding brightness temperature.

Having established important concepts which can be used to understand and distinguish between different radio emission mechanisms, we briefly describe relevant mechanisms for stellar radio emission.

1.3.3 Incoherent emission

Incoherent radio emission is found in a wide range of contexts in radio astronomy, since the conditions for its production are quite easily met. An important distinction between various forms of incoherent emission is whether it is thermal or non-thermal in nature. Thermal emission refers to emission produced by a population of electrons which are in local thermodynamic equilibrium (LTE), with a Maxwellian velocity distribution. In this thesis, we investigate cool stars at low radio frequencies ($\lesssim$ 1 GHz). The combination of their cool temperatures, small angular size, and the ν^2 spectral slope for optically thick thermal emission means that it is not likely to be detectable with current low-frequency facilities. Non-thermal emission is produced by electrons whose velocity distribution deviates strongly from a Maxwellian. These emission processes are important because their energy is generally sourced from electrodynamic processes, and may carry information about magnetic fields from the source to the observer.

Gyro-emission – produced by the gyration of electrons around magnetic fields – is a ubiquitous form of incoherent emission in radio astronomy. In the non-relativistic limit $\gamma = 1$, gyroresonance emission is produced. Synchrotron emission is produced in the ultra-relativistic case ($\gamma \gg 1$), and gyrosynchrotron emission is produced in the mildy relativistic case ($1 \lesssim \gamma \lesssim 10$). Figure 1.10 shows characteristic intensity and brightness temperature spectra for thermal gyrosynchrotron, non-thermal gyrosynchrotron, and synchrotron emission.

Gyroresonance emission

The electrons responsible for gyroresonance emission are non-relativistic and low in energy. Collisions with the ambient plasma are therefore important, and the velocity

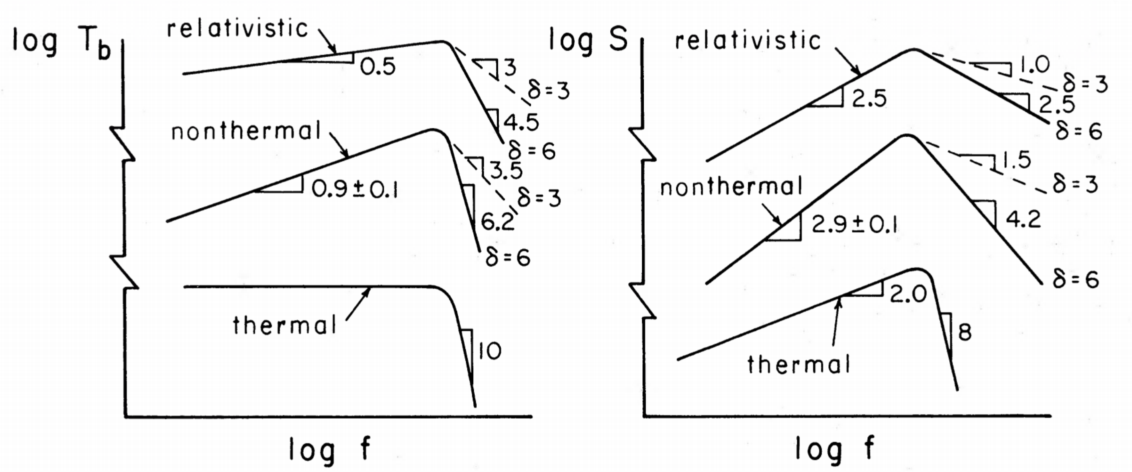

Figure 1.10: Characteristic brightness temperature (left) and intensity (right) spectra for thermal and non-thermal gyrosynchrotron emission as well as synchrotron emission. The high-frequency part of the spectra decline with increasing frequency, and corresponds with the optically-thin regime. For non-thermal (gyro)synchrotron, the optically-thin spectral slope is determined by the power law index of the electron velocity distribution, δ. The low-frequency part of the spectra corresponds with the optically-thick regime. For thermal gyro-emission, the brightness temperature is constant with frequency, and the optically-thick spectrum has a spectral index of $+2$. Figure from Dulk (1985).

distribution is usually well-described by a Maxwellian (Dulk, 1985). The emission is concentrated at the local electron cyclotron frequency ν_c and its moderately low harmonics $s \lesssim 10$.

Synchrotron emission

Synchrotron radiation is ubiquitous in radio astronomy, because it is the primary mechanism behind radio emission from active galactic nuclei and radio galaxies, which dominate the population of radio sources in the sky (e.g Condon et al., 1998). The plasma in these systems are readily accelerated to ultrarelativistic energies by the central supermassive black holes (Begelman et al., 1984). Although synchrotron emission has been observed in solar and stellar contexts (e.g. MacGregor et al., 2020, 2018), it requires unusually high-energy electrons in the context of stellar coronae, and is not commonly observed.

Gyrosynchrotron emission

Gyrosynchrotron emission can be generated by the electrons at the high-energy tail of a thermal velocity distribution, or by a population of non-thermal electrons with a velocity distribution generally described by a power-law:

$$n(E) = (\delta - 1)E_0^{\delta-1}N\,, \tag{1.28}$$

where $n(E)$ is the electron velocity distribution as a function of energy E, δ is the velocity distribution power-law index, E_0 is the low-energy cutoff (generally assumed to be $\sim 10\,\mathrm{keV}$), and N is the number of electrons with energies above E_0 (Dulk & Marsh, 1982). Emission at harmonics $10 \lesssim s \lesssim 100$ are usually most important for gyrosynchrotron emission. Analytic computation of the emission and absorption coefficients for gyrosynchrotron emission is nigh-intractable, although various numerical approximations have been determined (e.g. Dulk & Marsh, 1982; Robinson & Melrose, 1984). These have shown that the emission and absorption coefficients are dependent on the global plasma properties, such as the electron effective temperature, the viewing angle to the emission region, the electron density and the magnetic field strength (Dulk & Marsh, 1982; Robinson & Melrose, 1984). Gyrosynchrotron emission is usually mildly circularly polarised ($|f_C| \lesssim 50\%$), in the sense of the x-mode for optically-thin emission, and o-mode for optically thick emission. By measuring the broadband spectrum of gyrosynchrotron emission, plasma properties of the emission region can be determined through radiative transfer calculations. This makes gyrosynchrotron emission a valuable probe into the emission environment. Steady, non-flaring radio emission from a wide range of active stars, such as RS CVn binaries, active M-dwarfs, and ultra-cool dwarfs have been attributed to gyrosynchrotron emission from a population of mildly-relativistic power-law electrons (e.g. Gary et al., 1983; Mutel et al., 1987; Osten et al., 2005, 2006; Lynch et al., 2015). Centimetre-wavelength emissions associated with stellar flares are also usually attributed to gyrosynchrotron emission. Several studies of solar and stellar gyrosynchrotron emission have harnessed it to constrain the coronal properties of stars (e.g. Metodieva et al., 2017; Lynch et al., 2015; Osten et al., 2006). In Chapter 2 (published in Zic et al., 2019a), we use the low-frequency, optically-thick gyrosynchrotron emission spectrum from the ultra-cool dwarf 2MASS J1314+1320 to place constraints on its global electron density and magnetic field strength.

1.3.4 Coherent emission

Development of resistive instabilities in a plasma lead to "negative absorption" (Melrose, 2017). Strong amplification of electromagnetic radiation at certain wave modes of the plasma occurs, leading to *coherent* emission. This emission can only arise when the collisional frequencies of electrons and ions are lower than the resonance frequencies and sufficiently low so that the plasma instabilities are not destroyed. Coherent emission typically takes place at characteristic frequencies of the plasma, such as the electron plasma frequency ω_p or the electron cyclotron frequency ω_c. In the context of stellar radio emission, the two most important coherent emission processes are plasma emission and the electron cyclotron maser instability. These processes involve instabilities in the parallel and perpendicular velocity distributions of electrons with respect to the ambient magnetic field. We discuss these two emission mechanisms below.

Plasma emission

Plasma emission is the mechanism thought to be responsible for the majority of low-frequency solar radio bursts. These bursts, classified into types I-V, are typically generated by electrons accelerated in shocks or high-velocity electron streams. We provide further details on some types of solar radio bursts in Chapter 4, and a review

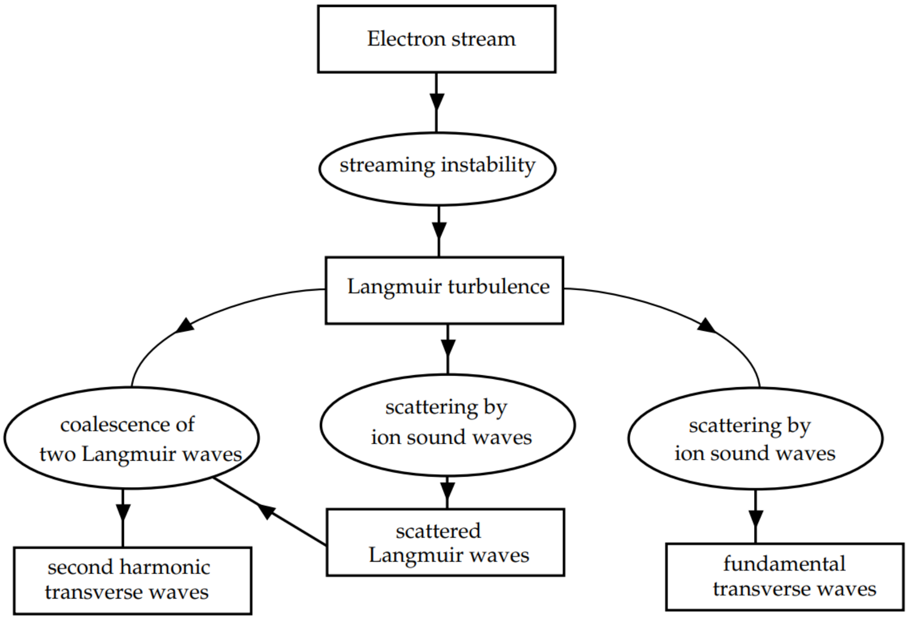

Figure 1.11: Schematic flowchart of the production of plasma emission, based on the original theory by Ginzburg & Zhelezniakov (1958). From Melrose (2017).

can be found in White (2007). Plasma emission has also been invoked to explain some coherent stellar radio bursts (e.g. Osten & Bastian, 2006).

Plasma emission is generated via secondary processes associated with Langmuir waves generated by high-velocity streams of electrons (also known as electron beams). As the high-velocity beam streams through the plasma, the velocity distribution of the ambient plasma develops a "bump" in the high-velocity tail. This bump leads to a plasma instability, which causes exponential growth of Langmuir waves which extract the free energy from the electron velocity distribution. Subsequent interaction with ion acoustic waves, outlined by the flowchart in Figure 1.11 can convert the plasma oscillations into free-propagating electromagnetic radiation at the fundamental or second harmonic of the local plasma frequency (Melrose, 2017). The theory behind the interactions of these wave modes is complex, and there have been significant developments since the foundational elements were established by Ginzburg & Zhelezniakov (1958) – see Robinson & Cairns (2000) and Melrose (2009) for reviews.

Observationally, plasma emission is expected to occur close to the local plasma frequency (see Equation 1.3) or its second harmonic (Melrose, 2017), enabling the emission to probe plasma density structure (e.g. Harding et al., 2019). Emission at the fundamental and second harmonic manifests clearly in solar type II and III bursts, which show clear harmonic pairs in dynamic spectra (see Figure 1.5). Fundamental plasma emission is polarised in the sense of the o-mode at the fundamental frequency, and weakly polarised at the second harmonic (Melrose et al., 1978).

The Electron Cyclotron Maser Instability

The electron cyclotron maser instability (ECMI) is responsible for the auroral radio emission of Earth and other magnetised solar system planets. Like plasma emission,

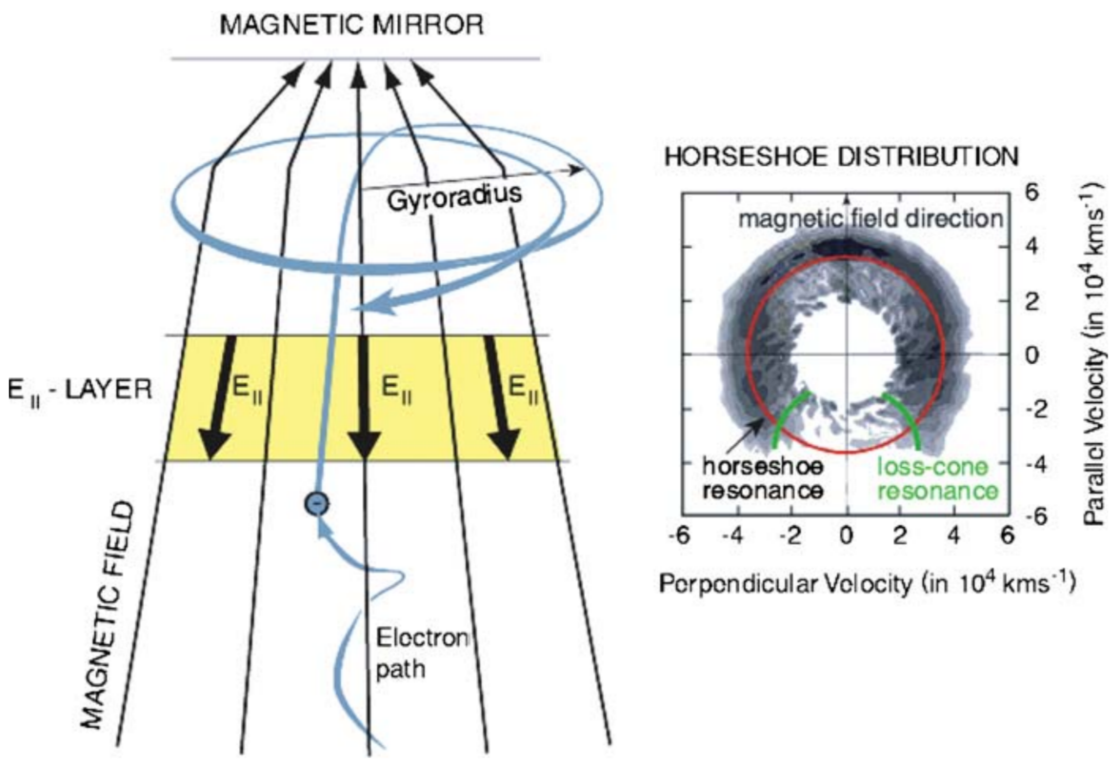

Figure 1.12: Illustration of the generation of a horse-shoe electron velocity distribution, from Treumann (2006). Electrons spiralling toward converging magnetic fields at the loop footpoint are accelerated by the parallel electric field. The magnetic mirror effect converts the excess energy gained from the electric field from parallel into perpendicular velocity, forming the electron velocity distribution in the figure right. The red and green lines indicate horseshoe and loss-cone relativistic resonance lines for perpendicular radiation in the x-mode. Image credit: Treumann (2006).

it is driven by a high-energy anisotropy in the electron velocity distribution, which leads to the exponential growth of radiation. For plasma emission, this anisotropy is in the parallel component of the electron velocity $v_\parallel$ (with respect to the magnetic field), whereas the electron cyclotron maser instability is driven by an anisotropy in the perpendicular component $v_\perp$, leading to negative absorption.

Early versions of ECMI theory were based on a loss-cone electron velocity distribution, where the electrons with a small $v_\perp$ (i.e. with small pitch angles $\alpha = \arctan(v_\perp/v_\parallel)$) are low in number. A loss cone velocity distribution can be generated within magnetic flux tubes within stellar and planetary magnetospheres as follows. Firstly, electrons high in magnetic loops are heated via magnetic reconnection, or accelerated by other processes (e.g. magnetosphere-ionosphere coupling; Cowley & Bunce, 2001; Nichols et al., 2012). These electrons initially have an isotropic pitch angle distribution, and so the velocity distribution function in $v_\perp$-$v_\parallel$ phase space is symmetric. An important requirement for the operation of the ECMI is that it operates in a highly-magnetised, low-density environment, such that the ratio of the plasma frequency to the electron cyclotron frequency $\omega_p/\omega_c \ll 1$.

As the electrons stream down toward the footpoints of the magnetic loop, the magnetic field strength increases, and so $v_\perp$ must also increase due to conservation of the first adiabatic invariant $\mu = m_e v_\perp^2/2B$, where m_e is the electron mass and B the local magnetic field strength. Conservation of kinetic energy implies that $v_\parallel$ decreases, and if the pitch angle is larger than a critical pitch angle $\alpha^* = \arcsin(B_{\text{top}}/B_{\text{foot}})$ (Dulk, 1985), the parallel velocity goes to zero and reverses: the magnetic mirror effect. Here, B_{top} and B_{foot} are the magnetic field strengths at the loop top, and at the foot. Particles with pitch angles $\alpha < \alpha^*$ are able to pass through the magnetic mirror, and so collide with the dense atmosphere below the magnetic loop and are lost. As a result, the velocity distribution function $f(\mathbf{x}, \mathbf{p})$ is depleted of particles with small pitch angles, and a region where $\partial f/\partial v_\perp > 0$ is formed.

Regions of the velocity distribution function with $\partial f/\partial v_\perp > 0$ are unstable to the growth of electromagnetic waves: there are more high-energy electrons which are able to donate their energy to an interacting wave than low-energy electrons which are able to absorb energy from the same wave (Dulk, 1985), leading to rapid wave growth. Theoretical studies have shown that the wave growth rate is fastest for the fundamental harmonic of the electron cyclotron frequency ($s = 1$), for the x-mode, at angles with respect to the magnetic field $\theta \sim 70°$ (Dulk, 1985; Melrose, 2017). Observationally, this means that emission from the loss-cone driven ECMI is highly circularly polarised according to the x-mode, and is highly beamed along a hollow cone, generating strong rotational modulation of the emission from the perspective of a distant observer.

However, loss-cone driven ECMI cannot explain some features of the terrestrial auroral kilometric radiation, such as ECMI frequencies occurring slightly below the cyclotron frequency, and radiation nearly perpendicular to the magnetic field (Bingham & Cairns, 2000). These discrepancies led to the development of horse-shoe driven ECMI, which combines a ring velocity distribution, where more electrons are able to contribute to the radiation energy compared with a loss-cone distribution (Treumann, 2006), and the loss-cone, forming a horse-shoe shaped velocity distribution (see Figure 1.12). This distribution can be set up in magnetic flux tubes in a similar way to the loss cone, but with the addition of an electric field parallel to the magnetic field, directed away from the object's surface. This is illustrated in Figure 1.12. Electrons are accelerated by the electric field parallel to the magnetic field, which evacuates the magnetic flux tube and increases the initial pitch angle threshold for electrons being lost to the atmosphere or reflected by the magnetic mirror. This provides a plausible explanation for solar, stellar, and planetary ECMI emissions (Ergun et al., 2000; Treumann, 2006; Melrose & Wheatland, 2016).

Several works have developed software to simulate the spectro-temporal signature of beamed ECMI radiation based on magnetic field geometries, beaming patterns, and magnetospheric refraction (Louis et al., 2019; Das et al., 2020; Leto et al., 2017; Lynch et al., 2015).

1.4 Research aims and outline of this thesis

This thesis presents investigations of cool stellar activity at low radio frequencies. Magnetically active stars display a wide range of variable behaviour across all wavelengths, such as flaring behaviour, space weather events, and auroral activity (see Sections 1.1.2). Low frequency radio emission provides an important probe into these processes, tracing particle acceleration, shocks, and the plasma environment.

Radio observations of ultra-cool dwarfs have revealed strong non-thermal radio emissions, with both persistent and bursty components, indicating the presence of strong magnetic fields (Berger et al., 2001; Berger, 2002, 2006; Kao et al., 2018). This was unexpected, since there is a sharp decline in other magnetic activity tracers such as H α and X-ray luminosity for these stars. The discovery of intense, periodic bursts from ultra-cool dwarfs showed that these stars host stable large-scale current systems which drive persistent aurorae (Hallinan et al., 2006, 2007, 2015). This demonstrated that the magnetic activity of these stars operates within a separate paradigm to the well-studied solar activity.

On the other hand, attempts to understand the radio emission from active M-dwarfs have largely been from within the solar activity paradigm (e.g. Bastian, 1990). At face value, this is well-justified – observations of stellar activity at other wavelengths have shown that they conform relatively well to the solar activity paradigm (e.g. Hawley et al., 1995; Guedel et al., 1996; Güdel et al., 2002a). However, the low-frequency radio emission of active M-dwarfs have shown properties inconsistent with the solar paradigm: primarily, the poor correlation with optical or X-ray activity, and key differences between the burst properties of solar and stellar low-frequency bursts; e.g. dynamic spectrum morphology and polarisation.

An important issue that arises is the relevance of the auroral and solar magnetic activity paradigms to the low frequency emission of active M-dwarfs. If the low-frequency emission from these stars can be shown to operate within the solar paradigm, it may provide key insights into the space weather around these stars (see Section 1.1.2). If the auroral paradigm applies, it has important implications for the behaviour of the large scale magnetic fields of these stars, demonstrating that processes operating in planetary magnetospheres can also operate in the magnetospheres of main sequence stars. Until work presented in this thesis (Chapter 3, published as Zic et al., 2019b), there were no confirmed detections of active M-dwarf aurorae reported in the literature.

In this thesis, we present detailed low-frequency observations of active stars, with the aim of probing their magnetospheres and determining the processes operating within. In Chapter 2, we present observations of nine ultra-cool dwarfs with the Giant Metrewave Radio Telescope. These observations were taken at ~ 610 and ~ 1300 MHz, providing coverage of the optically-thick quiescent emission and enabling us to estimate the spectral turnover frequency. We were able to reliably identify optically thick gyrosynchrotron emission in one target, and used our measurements along with measurements from archival literature to constrain its magnetospheric properties. Seven of the targets were not detected, indicating that the radio emission from these stars predominantly occurs at frequencies higher than about 2 GHz, and only some are capable of producing low-frequency emission.

In Chapter 3, we present Australian Square Kilometre Array Pathfinder (ASKAP) observations of the prototypical flare star, UV Ceti. These observations were the longest continuous radio-frequency observations of the star to date, and were motivated by recent results showing that the bursts from this star may be periodic in nature (Lynch et al., 2017; Villadsen & Hallinan, 2019). Our observations provide the first confirmation of periodic radio pulses from an active M-dwarf, showing that the auroral activity paradigm can also apply to active main-sequence stars. Similar to Lynch et al. (2017), we also detect a linearly polarised component to the radio bursts, and use this to infer the presence of extreme density cavities within the auroral emission region.

Chapter 4 presents results from one night of an 11-night simultaneous multi-wavelength campaign targeting Proxima Centauri, a moderately active M-dwarf and the closest star to the Sun. The goal of our campaign was to probe the space weather environment around this active M-dwarf and planet host, via observations of flares and solar-like radio bursts. We detected a powerful flare with several optical facilities (bolometric energy of $\sim 2 \times 10^{32}$ erg), accompanied with a series of intense, coherent radio bursts detected with ASKAP. These include the first detections of a coincident flare and coherent radio burst, and the most compelling detection of solar-like type IV burst identified. Solar type IV bursts are strong indicators of space weather activity, such as coronal mass ejections. Our detection of this type IV burst event therefore may indicate the occurrence of a coronal mass ejection from the star.

Chapter 5 summarises the conclusions of the previous chapters and places them in the context of this thesis. We discuss future avenues of exploration which are beginning to open as ASKAP sky surveys begin, and other radio facilities such as the Low-Frequency Array (LOFAR van Haarlem et al., 2013), the Murchison Widefield Array (MWA Tingay et al., 2013), and MeerKAT (Jonas, 2009) continue to improve and approach full operations.

Chapter 2

Low-frequency GMRT observations of ultra-cool dwarfs

Andrew Zic,[1,2] Christene Lynch,[1,2] Tara Murphy,[1,2] David L. Kaplan,[3] Poonam Chandra[4]

[1] Sydney Institute for Astronomy, School of Physics, The University of Sydney, NSW 2006, Australia.
[2] ARC Centre of Excellence for All-sky Astrophysics (CAASTRO), The University of Sydney, NSW 2006, Australia.
[3] Department of Physics, University of Wisconsin–Milwaukee, Milwaukee, WI 53201, USA.
[4] National Centre for Radio Astrophysics, TIFR, Pune University Campus, Pune 411007, India.

This Chapter was published as Zic et al. (2019a), MNRAS, 483, 614. My contributions to this work include writing the text, reducing the GMRT observations, analysis of the data, production of tables and figures and performing the radiative transfer modelling. Christene Lynch carried out the 2016 GMRT observations and provided code for the radiative transfer modelling.

2.1 Abstract

Observations of radio emission in about 10% of ultra-cool dwarfs (UCDs) indicate the presence of strong, persistent magnetic fields in these stars. These results are in contrast to early theoretical expectations on fully-convective dynamos, and to other tracers of magnetic activity, such as H α and X-ray luminosity. Radio-frequency observations have been key to physically characterising UCD magnetospheres, although explaining the diverse behaviour within them remains challenging. Most radio-frequency studies of UCDs have been conducted in the 4-8 GHz band, where traditional radio interferometers are typically most sensitive. Hence, the nature of UCD radio emission at low frequencies ($\lesssim 1.4$ GHz) remains relatively unexplored, but can probe optically thick emission, and regions of lower magnetic field strengths – regimes not accessible to higher-frequency observations. In this work, we present the results from Giant Metrewave Radio Telescope observations of nine UCDs taken at ~ 610 and 1300 MHz. These are the first observations of UCDs in this frequency range to be published in the literature. Using these observations, we are able to constrain the coronal magnetic field strength and electron number density of one of the targets to $1 \lesssim B \lesssim 90$ G and $4 \lesssim \log(N_e) \lesssim 10$, respectively. We do not detect the flaring emission observed at higher frequencies, to a limit of a few millijanskys. These results show that some UCDs can produce low-frequency radio emission, and highlights the need for simultaneous multi-wavelength radio observations to tightly constrain the coronal and magnetospheric properties of these stars.

2.2 Introduction

Stellar magnetic fields influence stars through all evolutionary stages, affecting their formation, mass loss, rotation, chemical composition, and behaviour at late evolutionary stages (Donati & Landstreet, 2009). At masses below $0.3 - 0.4\,\mathrm{M}_\odot$ (spectral types later than about M3.5), stellar interiors are fully convective (Chabrier & Baraffe, 2000), and lack the tachocline generally accepted to drive solar-type dynamos (Ossendrijver, 2003). Therefore, early expectations were that these stars were incapable of generating and sustaining strong, large-scale magnetic fields (Durney et al., 1993).

However, flares observed in very late M-dwarfs in H α, UV, and X-ray (Tagliaferri et al., 1990; Linsky et al., 1995; Martín, 1999; Liebert et al., 1999; Reid et al., 1999; Fleming et al., 2000) provided indications that some very low-mass stars exhibit at least sporadic magnetic activity. More recent work (e.g. Metodieva et al., 2017; Lynch et al., 2016; Williams et al., 2015a,b; Berger et al., 2010; Antonova et al., 2008; Hallinan et al., 2008, 2006; Berger, 2002; Berger et al., 2001) on ultra-cool dwarfs (UCDs; spectral class later than ~M7) at radio frequencies have revealed that around 10% of these stars exhibit both persistent and bursty radio emission, with many violating the well-known Güdel-Benz relation (GBR) by several orders of magnitude (Williams et al., 2014). The GBR is an empirically derived relation between X-ray and radio luminosities of magnetically active FGKM stars spanning several orders of magnitude, following $L_X \sim L_{\nu,R}^{0.73}$ (Benz & Guedel, 1994), with L_X denoting X-ray luminosity and $L_{\nu,R}$ radio spectral luminosity.

Gyrosynchrotron emission from a population of mildly-relativistic electrons (e.g. Berger et al. 2005, see Dulk 1985 for a review), or the electron-cyclotron maser instability (ECMI; e.g Hallinan et al. 2008, see Treumann 2006 for a review) have both been argued to be responsible for UCD radio emission. The ECMI is generally thought to be responsible for the bursty, flare-like emission from UCDs, owing to brightness temperatures in excess of 10^{12} K, and up to 100% circularly polarised emission. On the other hand, the persistent, non-flaring emission from UCDs has been argued to originate from gyrosynchrotron (e.g. Metodieva et al., 2017; Lynch et al., 2016; Williams et al., 2015b; Berger et al., 2005) or ECMI (e.g. Llama et al., 2018; Schlieder et al., 2014; Hallinan et al., 2008) processes. In any case, the presence of this radio emission reveals that these objects can generate strong, axisymmetric and active magnetic fields, in contrast to the expectations set by early fully-convective dynamo theory (Durney et al., 1993). Despite recent progress in dynamo models of low-mass stars (e.g. Yadav et al. 2016, 2015; Christensen 2010; Browning 2008), explaining the broad phenomenology of UCD magnetic activity revealed through their radio emission remains challenging (Williams et al., 2014).

The level of magnetic activity revealed by the radio emission was also surprising, given steep declines observed for UCDs in X-ray and H α luminosity (e.g. Williams et al., 2014; Berger et al., 2008; West et al., 2004; Mohanty & Basri, 2003; Gizis et al., 2000), which are conventional tracers of coronal and chromospheric activity in FGKM stars. It is thought that the drop in H α and X-ray luminosities is indicative of the transition to cooler, more neutral atmospheres for UCDs (Mohanty et al., 2002). The declines in H α and X-rays are accompanied by a breakdown in the rotation-activity relation for UCDs (e.g. Mohanty & Basri, 2003), while the radio rotation-activity relation remains relatively constant in the UCD regime (McLean et al., 2012). These divergent trends once again highlight the need to clarify UCD dynamo and coronal properties.

Radio-frequency observations have proven to be the most effective probes of UCD magnetism. This is in part due to the difficulty encountered when attempting techniques such as Zeeman–Doppler imaging to the faint, rapidly-rotating UCDs. This technique has only recently been successfully demonstrated for a UCD (Berdyugina et al., 2017).

However, the majority of radio studies of UCDs have been conducted between 4 and 8 GHz, and low-frequency ($\lesssim$ 1.4 GHz) radio emission of UCDs remains relatively unexplored. The presence and nature of radio emission at low frequencies is therefore not well-known. For radio emission from the ECMI, low-frequency observations can give insights into electron motions driving the ECMI (Yu et al., 2012), as well as probing regions of lower magnetic field strength. Using an input magnetospheric structure, low-frequency observations can therefore be used to constrain the coronal volume where conditions are favourable for the ECMI to take place (Llama et al., 2018; Jaeger et al., 2011). For gyrosynchrotron emission, the high-frequency regime is typically characterised by a power-law spectral energy distribution (SED), where it is difficult but not impossible to uniquely constrain coronal magnetic field strength, electron density, and other coronal parameters (Metodieva et al., 2017; Lynch et al., 2016, 2015; Ravi et al., 2011; Burgasser & Putman, 2005). However, at low frequencies the SED transitions to the optically-thick regime, which, when coupled with high-frequency measurements, allows coronal properties to be determined.

Previous low-frequency studies of UCDs include that by Jaeger et al. (2011), who observed two UCDs with the VLA at 325 MHz, and placed 2.5σ upper limits around 0.8 mJy, and Burningham et al. (2016), who observed three nearby UCDs with LOFAR at around 140 MHz, placing 3σ upper limits around 0.7 mJy. Unfortunately these limits are not deep enough to provide meaningful constraints on the SEDs of the observed UCDs. Other low-frequency studies of UCDs at low frequencies include a non-detection of TVLM 513−46 at 608 and 1388 MHz by Antonova (2007); and a survey of eight UCDs at 618 and 1288 MHz by George (2009). Both of these used the Giant Metrewave Radio Telescope (GMRT), and the results were not published in the peer-reviewed literature. In this paper, we present new observations of two UCDs observed at 608 and 1388 MHz with the GMRT taken in 2016. We also present a re-analysis of the 618 and 1288 MHz GMRT observations of eight UCDs first presented in George (2009). For simplicity, where appropriate we will collectively refer to the set of observations taken at 1288 and 1388 MHz as the 1300 MHz observations, and similarly we will refer to the observations taken at 618 and 608 MHz as the 610 MHz observations.

2.3 Observations

2.3.1 Target selection and description

The UCDs we observed during the 2016 campaign (2MASS J15010818+2250020 and 2MASS J13142039+1320011) were selected on the basis of exhibiting stable radio emission over many years. For the 2008 observations first presented by George (2009), the selected UCDs were a sample of nearby L-dwarfs, as well as the M8.5 dwarf 2MASS J15010818+2250020, and the T6.5 dwarf 2MASS J00345157+0523050. Basic properties of the target UCDs, including the updated coordinates given the proper motion of each UCD, are given in Table 2.1. We give a very brief description of each source below.

2MASS J13142039+1320011 (also known as NLTT 33370 and LSPM J1314+1320; hereafter J1314+1320): this is a binary system consisting of a blended spectral type M7.0e (Law et al., 2006). Its distance of 17.249 ± 0.013 pc determined by Forbrich et al. (2016) using very long baseline interferometry. It is the most radio-luminous UCD, and has been the subject of many detailed studies at radio frequencies, for example by McLean et al. (2011) and Williams et al. (2015a).

2MASS J15010818+2250020 (otherwise known as TVLM 0513−46546; hereafter TVLM 513−46): this is an M8.5 dwarf at a distance of 10.762 ± 0.027 pc (Forbrich et al., 2013). Like J1314+1320, it has been the subject of many studies at radio frequencies (e.g. Osten et al., 2006; Lynch et al., 2015; Williams et al., 2015b), which have revealed both periodic and stochastic flares, as well as quiescent emission observed between ~ 1 and 100 GHz.

2MASS J03140344+1603056 (hereafter 2M 0314+16): this L0.0 dwarf is at a distance of 13.62 ± 0.05 pc (Gaia Collaboration et al., 2018). An upper limit on its 8.46 GHz radio luminosity was placed by McLean et al. (2012).

2MASS J07464256+2000321 (hereafter 2M 0746+20): this is a near-equal mass binary system of spectral type L0.5 at a distance 12.21 ± 0.04 pc (Faherty et al., 2009). It was first detected at radio frequencies by Antonova et al. (2008), and follow-up studies have detected quiescent and periodic pulsating emission (Berger et al., 2009; Lynch et al., 2015).

2MASS J08283419−1309198 (hereafter 2M 0828−13): this L2.0 dwarf is at a distance of 11.69 ± 0.02 pc (Gaia Collaboration et al., 2018). Upper limits on its radio luminosity have been placed by Antonova et al. (2013) and McLean et al. (2012) at 4.9 and 8.4 GHz respectively.

2MASS J00361617+1821104 (hereafter 2M 0036+18): this is an L3.5 dwarf at a distance of 8.74 ± 0.01 pc (Gaia Collaboration et al., 2018). It is a well-studied object at radio frequencies, having been detected, for example, by Berger (2002), Berger et al. (2005), and Metodieva et al. (2017).

2MASS J03552337+1133437 (hereafter 2M 0355+11): this L6 dwarf is at a distance of 9.12 ± 0.06 pc (Gaia Collaboration et al., 2018). An upper limit on its radio luminosity was placed by Antonova et al. (2013).

2MASS J04234858−0414035 (hereafter 2M 0423−04): this is a binary system consisting of an L6.5 and a T2 dwarf (Dupuy & Liu, 2012) at a distance of 14.7 ± 0.3 pc (Gaia Collaboration et al., 2018). Radio pulses from this object were detected by Kao et al. (2016).

2MASS J	Short Name	SpT	Epoch	RA (h:m:s)	Dec (d:m:s)	Distance (pc)	Reference
13142039+1320011	J1314+1320	M7.0e	2016-05-19 2016-05-01	13:14:20.1	+13:19:57.9	17.249 ± 0.013	F16
15010818+2250020	TVLM 513−46	M8.5	2016-09-25 2016-08-18 2008-01-19	15:01:08.1 15:01:08.1 15:01:08.2	+22:50:01.1 +22:50:01.1 +22:50:01.7	10.762 ± 0.027	F13
03140344+1603056	2M 0314+16	L0.0	2008-01-26 2008-01-25	03:14:03.3	+16:03:05.1	13.62 ± 0.05	GDR2
07464256+2000321	2M 0746+20	L0.5	2008-01-21 2008-01-19	07:46:42.3	+20:00:31.5	12.21 ± 0.04	F09
08283419−1309198	2M 0828−13	L2.0	2008-01-21 2008-01-19	08:28:33.9	−13:09:19.6	11.69 ± 0.02	GDR2
00361617+1821104	2M 0036+18	L3.5	2008-01-28 2008-01-22	00:36:16.6	+18:21:11.4	8.74 ± 0.01	GDR2
03552337+1133437	2M 0355+11	L6	2008-01-26 2008-01-25	03:55:23.5	+11:33:38.6	9.12 ± 0.06	GDR2
04234858−0414035	2M 0423−04	L7.5	2008-01-24 2008-01-18	04:23:48.6	−04:14:03.5	14.7 ±0.3	GDR2
00345157+0523050	2M 0034+05	T6.5	2008-01-28 2008-01-22	00:34:51.9	+05:23:06.4	9.5 ± 0.7	F12

Table 2.1: Properties of the UCDs analysed in this work. From left to right, the columns indicate: the UCD 2MASS name; the shortened name adopted for this work; spectral type (SpT); the observation epoch UT date; J2000 right ascension and declination at each epoch; distance; and the reference used for the distance, and to calculate updated coordinates. These references are: F16: Forbrich et al. (2016); F13: Forbrich et al. (2013); GDR2: Gaia Collaboration et al. (2018); F12: Faherty et al. (2012)

2MASS J00345157+0523050 (hereafter 2M 0034+05): this is a T6.5 dwarf at a distance of 9.5 ± 0.7 pc (Faherty et al., 2012). No radio observations of this object are reported in the literature to date.

2.3.2 Observing strategy

We observed J1314+1320 and TVLM 513−46 with the GMRT in a campaign spanning from May – September 2016. We conducted observations at two central observing frequencies – 1388 MHz and 608 MHz – each with an instantaneous bandwidth of 33.3 MHz. These observations were taken using the GMRT Software Backend (GSB). We observed the primary calibrators in scans lasting approximately 15 minutes at the beginning and end of each observation. Scans centred on the target object lasted approximately 30 minutes and were interleaved between 5-minute duration scans on the secondary calibrator. Primary instrumental polarisation products were recorded. Note that the GMRT feeds in the L-band ($\nu = 1 - 1.45$ GHz) receiver are linear, and all feeds in lower frequency receivers are circular. In practice, this means that XX and YY instrumental polarisations were recorded for 1300 MHz, where as the 618 MHz observations have RR and LL instrumental polarisations.

In addition, we also re-analysed observations of eight UCDs presented in the PhD thesis of George (2009). These observations were carried out in January 2008 using the GMRT Hardware Backend (GHB). Similarly to our 2016 observations, each UCD was observed at 1288 MHz and 618 MHz. polarisation products were recorded in GHB USB-Polar mode, where RR and LL (618 MHz; circular feeds) or XX and

Name	Observation start (UT)	ν (MHz)	τ (h)	Primary calibrator	Secondary calibrator
J1314+1320	2016-05-19 13:00:18	1388	4.85	3C 286	J1309+1104
	2016-05-01 15:12:31	608	5.15		
TVLM 513−46	2016-09-25 12:05:00	1388	3.97	3C 286	1513+236
	2016-08-18 12:50:03	608	2.60	3C 468	
	2008-01-19 12:00:00	1288	5.43	3C 147	
2M 0314+16	2008-01-26 14:48:04	1288	1.05	3C 147	0321+123
	2008-01-25 11:13:00	618	2.55		
2M 0746+20	2008-01-21 14:04:33	618	3.03	3C 147	0738+177
	2008-01-19 14:10:23	1288	2.54		
2M 0828−13	2008-01-21 18:29:04	618	2.65	3C 147	0902−142
	2008-01-19 17:56:02	1288	2.62		
2M 0036+18	2008-01-28 09:15:45	618	1.67	3C 48	0029+349
	2008-01-22 07:33:27	1288	2.52		
2M 0355+11	2008-01-26 10:18:47	1288	1.99	3C 48	0321+123
	2008-01-25 11:21:23	618	2.55		
2M 0423−04	2008-01-24 13:19:50	618	3.52	3C 147	0423−013
	2008-01-18 13:56:33	1288	1.87		
2M 0034+05	2008-01-28 12:18:37	618	3.07	3C 48	0022+002
	2008-01-22 11:29:26	1288	2.54		

Table 2.2: Summary of observations presented in this work. Left to right, the columns indicate: the shortened name (as in Table 2.1); the observation start time; central observing frequency ν; total time spent on-source τ; the primary calibrator, and secondary calibrator used during observations.

YY (1288 MHz; linear feeds) correlations were both recorded only in the upper 16 MHz of the available bandwidth, and stored in separate `lta` files. The observing strategy for these observations was very similar to our observing strategy for the 2016 observations.

The details of all observations analysed in this work, including the observing frequency, the total time spent on source, and the calibrator sources used, are listed in Table 2.2.

2.4 Data Reduction

We calibrated and imaged the data using the Source Peeling and Atmospheric Modeling (SPAM) Pipeline (Intema, 2014; Intema et al., 2009). A detailed description of the SPAM pipeline is given by Intema et al. (2017), but we include a brief description of the pipeline here for completeness. In the first stage of the SPAM pipeline (the 'pre-calibration' stage), we performed basic iterative RFI excision, bandpass and complex gain calibration, and flux density scaling. Following this, we performed several rounds of phase-only self-calibration, using an input sky model as an approximate flux density and astrometric reference. We imaged the target field using several facets to account for wide-field imaging effects, and applied several RFI excision routines to the data between rounds of self-calibration and imaging. Following self-calibration, we performed source peeling, and in case of improved signal-to-noise, we saved the self-calibration solutions in facets containing the peeled sources. Following the peeling procedure for the brightest field sources, we used the derived solutions to model the time-dependent ionospheric phase delay across the field of view. We subtracted the modelled phase delays from the visibilities, before performing additional rounds of self-calibration to correct any residual phase variations.

We applied the SPAM pipeline to all observations to produce Stokes I continuum images, as well as images for the primary instrumental polarisations. In the case of the archival observations, each instrumental polarisation was stored in separate `lta` files. We processed each instrumental polarisation separately with SPAM, but supplied a sky model when processing the LL (YY) polarisation, by running the AEGEAN source finder (Hancock et al., 2018, 2012) on the RR (XX) primary beam-corrected image produced by SPAM at 618 MHz (1288 MHz). This step is justified given that the majority of compact radio continuum sources are unpolarised, meaning that flux densities of most sources from the LL/XX image should be consistent with the RR/YY image. We found that performing this step improved the quality of phase calibrations in some LL data, and at worst did not cause noticeable degradation of the quality of the calibration solutions. Similar phase calibration issues were not identified in the RR data, which is why we chose to calibrate the LL data using the sky model created with RR images. Stokes I continuum images were produced by simply co-adding the images produced for each of the primary instrumental polarisations.

In the 1300 MHz observations (both from 2008 and 2016), there were not enough bright sources in the smaller fields of view to successfully perform the peeling routine with SPAM. In this case, we disabled the peeling process with SPAM. We note that this is not likely to have a significant impact on the quality of the overall calibration, because ionospheric effects are not as significant at frequencies around and higher than 1300 MHz.

In the case of the 2016 observations, we produced Stokes I continuum images directly. If a UCD was detected in the 608 MHz Stokes I images, we split the corresponding LL and RR instrumental polarisations into separate files after the SPAM 'pre-calibration' stage. UCDs are well known to exhibit highly polarised bursts of radio emission. To determine if any of the detected UCDs were significantly circularly polarised, we processed the RR and LL instrumental polarisations individually with SPAM. We used the method implementing a sky model with SPAM as outlined above, but for the 2016 observations the sky model was produced from the full Stokes I continuum image rather than a single instrumental polarisation.

All observations were imaged with robust weighting. The centrally condensed GMRT array can lead to strong, broad sidelobes around bright sources in the field. We set the briggs parameter to -1, being closer to uniform weighting, therefore reducing the impact of sidelobe confusion and large-scale sidelobe artefacts in the final images.

2.5 Results

2.5.1 Non-flaring emission

In each of the continuum images, we used CASA task `imfit` to determine the integrated flux density at the expected location of each UCD, given measurements of proper motion reported in the literature. In the case of a detection, we report

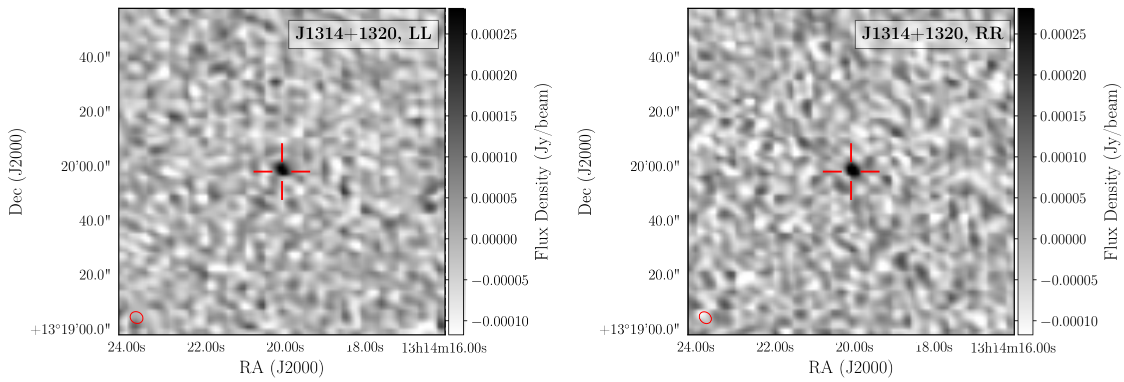

Figure 2.1: Postage stamp images of J1314+1320, in LL (left sub-figure) and RR (right sub-figure) instrumental polarisations, at an observing frequncy of 608 MHz. The expected location of the UCD, given its proper motion, is indicated by the red crosshairs. The shape of the synthesised beam is indicated by the red ellipse in the lower left corner. A detection of a point source at the expected location of J1314+1320 is clear in both the LL and RR images.

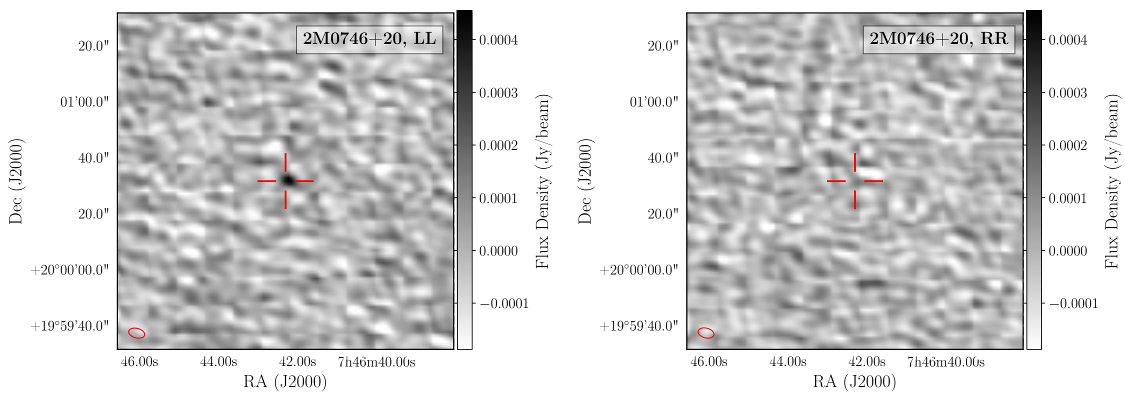

Figure 2.2: Same as Figure 2.1, but for 2M 0746+20 at 618 MHz. The high degree of left-circular polarisation is revealed by the strong detection ($481 \pm 69\,\mu$Jy) in the LL instrumental polarisation, and non-detection in RR, with a 3σ upper limit of $241\,\mu$Jy.

Name	S_{610} (μJy)	S_{1300} (μJy)	$T_{b,610}$ (10^{10}K)	$T_{b,1300}$ (10^{10}K)
J1314+1320	391 ± 26	908 ± 65	19 ± 1	8.8 ± 0.6
TVLM 513−46	< 148 [a]	< 194 [b] < 201 [c]	< 2.8 [a]	< 0.85 [b] < 0.76 [c]
2M 0314+16	< 200	< 728	< 6.3	< 5.1
2M 0746+20	319 ± 58	355 ± 65	8.0 ± 1.5	2.0 ± 0.4
2M 0828−13	< 160	< 165	< 3.7	< 0.85
2M 0036+18	< 800	< 1040	< 10	< 3.0
2M 0355+11	< 184	< 1020	< 2.6	< 3.2
2M 0423−04	< 150	< 1360	< 5.5	< 11
2M 0034+05	< 245	< 243	< 3.8	< 0.83

Table 2.3: Summary of detections and 3σ upper limits of the observed UCDs. Left to right, the columns indicate the shortened UCD name; the flux density at 610 MHz; flux density at 1300 MHz; and the corresponding brightness temperatures at 610 and 1300 MHz. Notes: (a): Epoch 2016-08-18; (b): Epoch 2008-01-19; (c): Epoch 2016-09-25

uncertainties in flux density as computed in the `imfit` process. Where there was no detection, we calculated the RMS noise in the local region around the UCD using CASA task `imstat`, and used this to set 3σ upper limits on the flux density. A summary of the results for non-flaring emission for each UCD is given in Table 2.3. Of the nine UCDs, we detect radio emission from two: J1314+1320, and 2M 0746+20. These objects are detected both at $\sim$ 610 and 1300 MHz. Postage-stamp images showing the detections of J1314+1320 and 2M 0746+20 at 610 MHz, in LL and RR instrumental polarisations, are shown in Figures 2.1 (J1314+1320) and 2.2 (2M 0746+20).

2.5.2 Variable emission

To search for any variable or flaring emission, we imported the SPAM-calibrated Stokes I visibilities into CASA v5.1.2 (McMullin et al., 2007) and imaged the full length of the observations. We subtracted the CLEAN model components for all field sources except for the target UCD from the visibilities using CASA task `uvsub`. We imaged the residual uv-subtracted data on 2, 5, and 10-minute time-scales using CASA task `tclean`. Similarly to the continuum images we produced using SPAM, we produced short-time-scale images using robust weighting with a briggs factor of −1. We created light-curves by taking the peak flux density in a box centred at the expected location of each UCD, with dimensions equal to 2.5 times the semi-major axis of the restoring beam in the image. The dimensions of the fitting box were slightly enlarged to account for any potential spurious astrometric offsets produced during SPAM processing. We calculated the local RMS noise by taking the standard deviation in a large box around the expected location of the source, clipping out pixels with flux densities deviating by more than 3σ, and evaluating the standard deviation of the residual pixels. We set a detection threshold of 5σ for any flaring or variable emission. We did not find any emission above this threshold over 2, 5, and 10-minute time-scales, indicating a lack of flaring activity of these UCDs at these frequencies, at levels above a few millijanskys. We did not fold the light-curves at the expected rotational period of each UCD. This is because our observations are only long enough to cover approximately two periods at best, meaning that phase-folding only provides a modest gain in sensitivity.

2.5.3 Characterising the radio emission

Brightness temperatures

To further characterise the observed radio emission, we calculated the corresponding brightness temperatures using the expression

$$T_b = 2.5 \times 10^9 \left(\frac{S_\nu}{\mathrm{mJy}}\right) \left(\frac{\nu}{\mathrm{GHz}}\right)^{-2} \left(\frac{d}{\mathrm{pc}}\right)^2 \left(\frac{R}{R_{\mathrm{Jup}}}\right)^{-2} \mathrm{K}, \tag{2.1}$$

with flux density S_ν at frequency ν, measured from a source of distance d, and emission region of radius R. Here, $R_{\mathrm{Jup}} = 7.0 \times 10^9$ cm is the radius of Jupiter, which is thought to be the typical radius of UCDs (Burrows et al., 2001). There have been no direct measurements of the radio emission region size of UCDs. We therefore adopted an emission region radius of $2\,R_*$ ($= 2\,R_{\mathrm{Jup}}$), thought to be the size of M-type stellar coronae (Leto et al., 2000). We find that the measured flux densities and upper limits yield brightness temperatures in the range of $(0.76 - 19) \times 10^{10}$ K. For the detected UCDs, these brightness temperatures rule out thermal bremsstrahlung emission as the source of the radio emission, favouring non-thermal emission processes instead. In a following section (Section 2.5.4), we describe modelling of the corona of J1314+1320. When performing this modelling, we allowed the total radio emission region size L (where $L = 2R$) to vary between $1.0-12.0\,R_*$. Adopting these values alters the brightness temperatures by factors between 16 and 1/9 relative to our brightness temperature calculated with $R = 2\,R_*$. Regardless, the brightness temperatures of the detected UCDs remain greater than 2.2×10^9 K, inconsistent with thermal emission.

Polarisation

For the detections made at 610 MHz, we were able to determine the degree of circular polarisation by calibrating and imaging the LL and RR instrumental polarisations independently, as described in Section 2.4. Because SPAM does not perform any polarisation calibration, our detections may be subject to leakage on the order of 5% (Farnes, 2014). We used CASA task `imfit` to determine the flux density of the target source in each instrumental polarisation.

For J1314+1320, we find that the LL flux density at 608 MHz is $357 \pm 44\,\mu$Jy, and the RR flux density is $523 \pm 46\,\mu$Jy. Because our target source is close to the phase centre, the corresponding leakage should be relatively small (Farnes, 2014).

To estimate the polarisation leakage, we measured the flux density of two nearby bright sources in the LL and RR images. Using these flux densities, we calculated polarisation fractions of $2 \pm 2\%$. We add a conservative leakage estimate of 5% in quadrature with the relevant measurement uncertainties. This implies a circular polarisation fraction $\pi_c = (S_{\mathrm{RR}} - S_{\mathrm{LL}})/(S_{\mathrm{RR}} + S_{\mathrm{LL}})$ of $+19 \pm 12\%$. Here, S_{RR} and S_{LL} are the RR and LL flux densities, respectively.

For 2M 0746+20, we measure a flux density in the 618 MHz LL instrumental polarisation of $481 \pm 69\,\mu$Jy, but in RR, we make no detection, with a 3σ upper limit of $241\,\mu$Jy. We calculate a 3σ upper limit on the polarisation fraction as follows. We take the 3σ upper limit of $241\,\mu$Jy as the fiducial measured value of the RR flux density, for the purpose of calculating the appropriate uncertainty only. We then apply standard error propagation using the measured uncertainties and flux densities to calculate an uncertainty in the fiducial polarisation fraction of 24.5%. Multiplying this by -3 (where the minus sign indicates a left-handed sense of circular polarisation, following convention) gives a 3σ upper limit of $\pi_c < -76\%$. We note that because there is no detection in the RR instrumental polarisation, there is no need to take leakage into account for this lower limit.

Radio emission mechanism

As mentioned in Section 2.5.3, the high brightness temperatures of the detected UCDs rule out thermal emission being responsible for the observed radio emission. However, they do not exceed the 10^{12} K limit for the inverse-Compton catastrophe (Kellermann & Pauliny-Toth, 1969). Although some (e.g. Hallinan et al., 2008) have argued that steady emission from UCDs may be generated by the ECMI, the inferred brightness temperatures do not favour coherent emission processes (unless the source size has been over-estimated). We therefore cannot rule out incoherent emission processes such as gyrosynchrotron radiation from a non-thermal electron population.

For J1314+1320, the modest level of circular polarisation (approximately 19%) also disfavours coherent emission processes which can have polarisation fractions up to 100%. Furthermore, the detection of persistent radio emission across a very broad frequency range, from 608 MHz to 22.5 GHz (McLean et al., 2011) suggests that the ECMI is not the source of the observed emission, since ECMI emission is expected to be strongly peaked around the cyclotron frequency and its harmonics, with a sharp spectral cut-offs. Finally, the positive spectral index at low frequencies is suggestive of optically-thick gyrosynchrotron radiation, and we conclude that this is likely to be the source of the persistent emission observed from this source.

For 2M 0746+20, the upper limit on the fractional circular polarisation of -76% is quite strong, but is still consistent with gyrosynchrotron radiation (e.g. Dulk, 1985; Pandya et al., 2016). The perceived lack of variability, along with the broad frequency range over which flux densities have been recorded (610 MHz to 8.5 GHz) do not favour ECMI as the emission source. Therefore, we conclude that these observations mildly favour gyrosynchrotron radiation as the emission mechanism, though we cannot strongly rule out ECMI as being the emission mechanism, primarily due to the strong upper limit of fractional circular polarisation $\pi_c < -74\%$. Future broad-band, simultaneous radio observations of this star would assist in clarifying

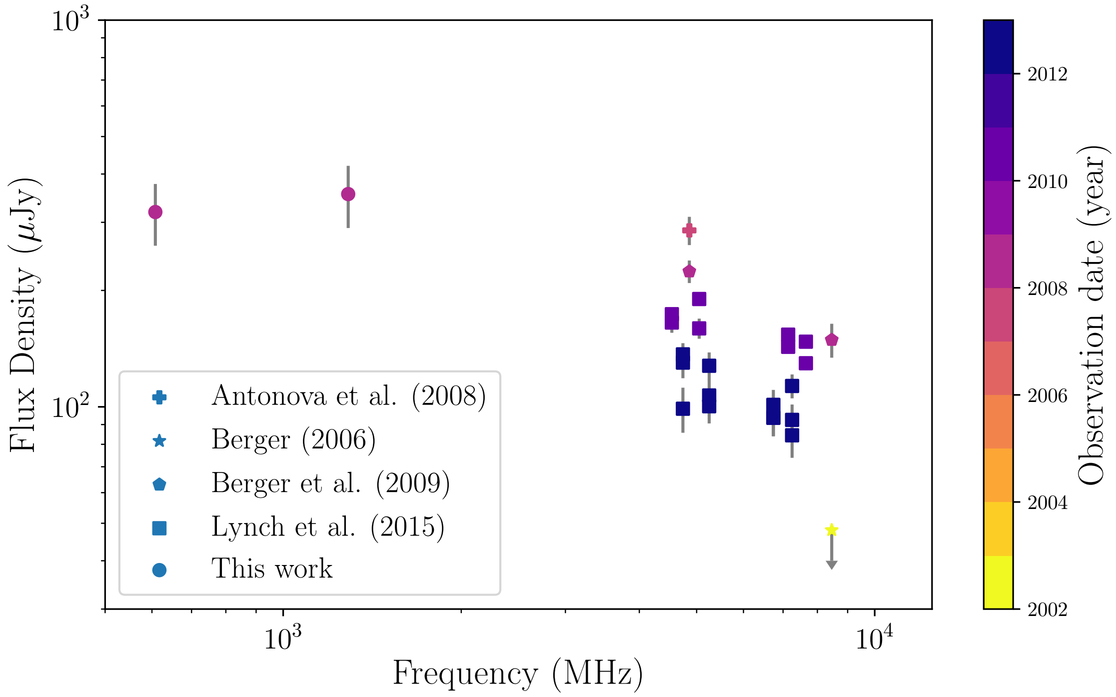

Figure 2.3: Non-simultaneous SED of 2M 0746+20, with flux densities as measured in this work, and taken from Antonova et al. (2008); Berger (2006); Berger et al. (2009), and Lynch et al. (2015). A high degree of long-term variability at high frequencies, along with an unclear turnover frequency, means that we cannot use the spectral turnover frequency as an additional constraint on the coronal parameters of this UCD. We therefore do not attempt to model the coronal parameters of this UCD.

the nature of its radio emission mechanism.

2.5.4 Coronal modelling

The flux density measurements across the SED of each UCD are non-simultaneous, with gaps of months or years between individual observations. It is well-known that the non-flaring emission from UCDs can vary significantly over long time-scales (e.g Antonova et al., 2007). Therefore, care should be taken when estimating coronal properties of UCDs using non-simultaneous spectral flux density measurements. Figure 2.3 shows that the spectral flux densities of 2M J0746+20 vary by factors of a few over long time-scales. Moreover, while our low-frequency flux density measurements hint at a rising spectrum (increasing flux density with increasing observing frequency), the location of the turnover frequency is not clear. For instance, the difference in flux densities at 618 and 1288 MHz is sufficiently small to be fully explained by long-term variability of the quiescent emission. We therefore cannot use the spectral turnover frequency as an additional constraint on this UCD's coronal properties, and so we refrain from modelling its coronal properties in this work.

On the other hand, as shown in Figure 2.4, long-term variability of the persistent emission from J1314+1320 appears to be more mild than that of 2M 0746+20.

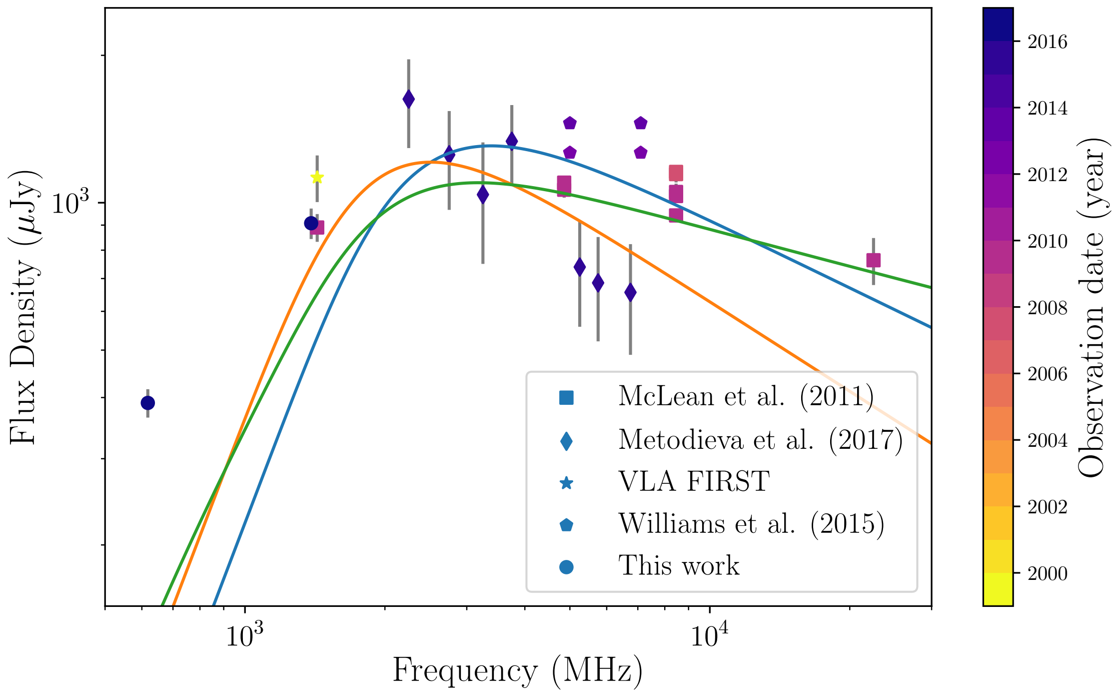

Figure 2.4: Non-simultaneous SED of J1314+1320, with flux densities as measured in this work, and taken from McLean et al. (2011); Williams et al. (2015a) and Metodieva et al. (2017). Using these measurements, we produced model gyrosynchrotron SEDs, varying the radio emission region size L, electron energy power-law index δ, coronal magnetic field strength B, and electron number density N_e. Some example model SEDs for coronal parameters consistent with the observed flux densities are shown as blue, orange, and green solid lines. Respectively, these correspond to coronal parameters of: $L = 5.0\,R_*, \delta = 1.91, B = 1.5\,\mathrm{G}, N_e = 2 \times 10^8\,\mathrm{cm}^{-3}$ (blue); $L = 8.0\,R_*, \delta = 2.19, B = 2.8\,\mathrm{G}, N_e = 9 \times 10^7\,\mathrm{cm}^{-3}$ (orange); $L = 11.0\,R_*, \delta = 1.47, B = 18.0\,\mathrm{G}, N_e = 4 \times 10^4\,\mathrm{cm}^{-3}$ (green). These example model SEDs are qualitatively consistent with the observed spectral flux densities, and illustrate that a wide range of coronal parameters are plausible for J1314+1320.

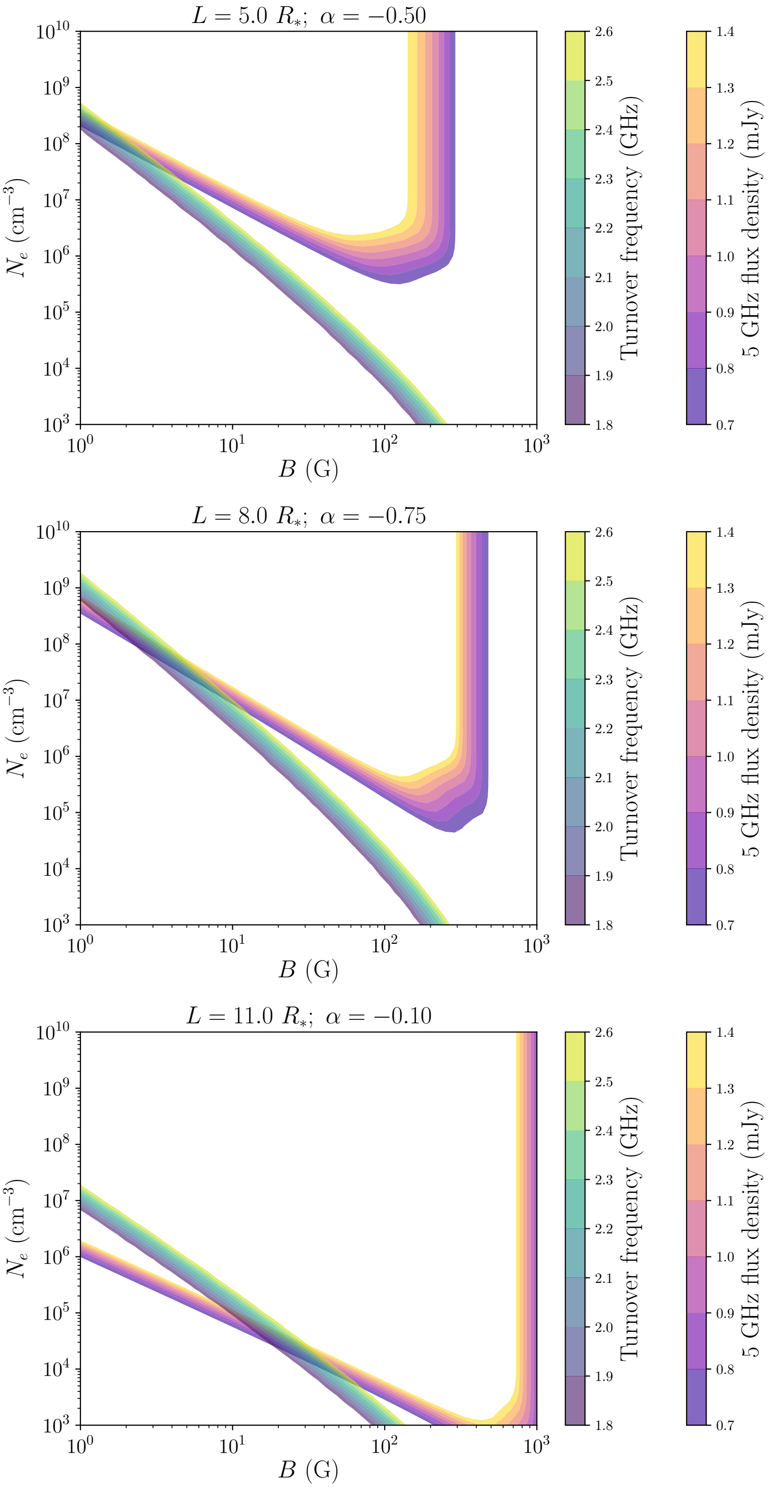

Figure 2.5: Representative plots showing regions of N_e and B parameter space consistent with criteria on the spectral turnover of J1314+1320 being close to 2.2 GHz, and 5 GHz flux density around 1 mJy. The region of parameter space where the two sets of contours overlap is where the parameters are consistent with our observations. The shaded contours represent turnover frequencies and 5 GHz flux densities for $L = 5.0\,R_*,\ \alpha_{\rm thin} = -0.5$; $L = 8.0\,R_*,\ \alpha_{\rm thin} = -0.75$; $L = 11.0\,R_*,\ \alpha_{\rm thin} = -0.1$ from top to bottom, respectively.

Work	α_{thick}	α_{thin}	S_{br} (mJy)	ν_{br} (GHz)
M17	$1.04^{+0.12}_{-0.13}$	$-0.90^{+0.27}_{-0.32}$	$1.57^{+0.17}_{-0.18}$	$2.36^{+0.30}_{-0.26}$
W15	$1.01^{+0.12}_{-0.13}$	0.00 ± 0.02	1.36 ± 0.03	$2.1^{+0.3}_{-0.2}$
M11	1.0 ± 0.1	-0.10 ± 0.03	1.21 ± 0.04	$1.93^{+0.16}_{-0.13}$
All data	1.0 ± 0.1	-0.17 ± 0.02	1.52 ± 0.03	$2.30^{+0.16}_{-0.13}$

Table 2.4: Results from the MCMC fit of a broken power-law to the non-simultaneous flux density measurements across the SED of J1314+1320. Each row indicates the results from a fit to the low frequency GMRT measurements paired with the measurements from the works cited in the first column. The final row shows the results from combining all measurements to use in MCMC fitting. From left to right, the columns indicate the work where measurements are taken from; the optically thick (low-frequency) spectral index (α_{thick}); the optically-thin (high-frequency) spectral index (α_{thin}); the flux density at the spectral turnover S_{br}; and the spectral turnover frequency ν_{br}. Works used: M17: Metodieva et al. (2017); W15: Williams et al. (2015a); M11: McLean et al. (2011)

Additionally, the 608 MHz flux density unambiguously shows a rising spectrum at low frequencies. These features allow us to make order-of-magnitude estimates of the coronal properties of J1314+1320. Nonetheless, because of the uncertainty introduced by long-term variability, we used a simple coronal model, containing a uniform power-law electron density within a homogeneous magnetic field. We used the expressions for gyrosynchrotron emission and absorption coefficients given in Robinson & Melrose (1984) for a population of electrons with a power-law energy distribution of the form

$$N_e(\gamma) = N_0(\delta - 1)E_0^{\delta-1}(\gamma - 1)^{\delta}, \tag{2.2}$$

where γ is the electron Lorentz factor, δ is the electron power-law index, $N_0 = \int_1^\infty N(\gamma)d\gamma$ is the total non-thermal electron population, and E_0 is the low-energy cutoff ($N(\gamma) = 0$ when $(\gamma - 1) < E_0$). We performed radiative transfer simulations by calculating the emission and absorption coefficients along the propagation paths to calculate the corresponding spectral flux density for a given choice of model parameters. We varied the coronal magnetic field strength B, electron number density N_e, and emission region size L of the toy model. Note that δ depends on the optically-thin spectral index α_{thin} through

$$\delta = -\frac{\alpha_{\text{thin}} - 1.22}{0.9}, \tag{2.3}$$

(Dulk, 1985). Figure 2.4 shows that the optically-thin spectral index of J1314+1320 varies over long timescales. Therefore, we also varied the electron power-law index δ in the radiative transfer modelling. We found that the modelled flux densities depend weakly on the viewing angle θ between the line of sight and the magnetic field, for values between $10 - 80°$. Therefore, to simplify the modelling procedure, we chose to keep θ fixed at 25°, within the range of acceptable values reported by Metodieva et al. (2017), ignoring the sense of polarisation.

We empirically determined the spectral turnover frequency by running a Markov Chain Monte Carlo (MCMC) sampler, from the EMCEE package (Foreman-Mackey et al., 2013), to fit a broken power law of the form

$$S_\nu = \begin{cases} S_{\rm br}(\nu/\nu_{\rm br})^{\alpha_{\rm thick}} & \text{if } \nu \leq \nu_{\rm br} \\ S_{\rm br}(\nu/\nu_{\rm br})^{\alpha_{\rm thin}} & \text{if } \nu > \nu_{\rm br} \end{cases}, \tag{2.4}$$

where $\alpha_{\rm thick}$ is the optically-thick spectral index, and $S_{\rm br}$ is the flux density at the spectral break frequency $\nu_{\rm br}$, representing the transition frequency from optically thick to optically thin emission. We used a uniform prior on the break frequency, setting bounds of $1.0 \leq \nu_{\rm br} \leq 4.86\,\text{GHz}$.

We fit the broken power law to the flux density measurements reported in this work, and from Metodieva et al. (2017), Williams et al. (2015a), and McLean et al. (2011). Because the measurements reported in Metodieva et al. (2017) and Williams et al. (2015a) were taken simultaneously, we paired our low-frequency measurements with the measurements from these two works, as well as from McLean et al. (2011), separately. We fit the data independently for each pairing, as well as producing an overall fit using all measurements. This enabled us to account for long-term spectral variability in our analysis. The best-fitting parameters using measurements from each work are given in Table 2.4.

To qualitatively assess the goodness of fit of a model to the measured flux densities, we allow models that give turnover frequencies between 1.8 and 2.6 GHz, corresponding with the extreme upper and lower bounds of all measurements of $\nu_{\rm br}$. The modelled turnover frequencies were determined by finding where the optical depth was equal to 1. For comparison of our modelled flux densities to the measurements at around 5 GHz, we allow models producing 5 GHz flux densities between 0.7 and 1.4 mJy. We chose not to compare the model to our low-frequency measurements because the numerical expressions for emission and absorption coefficients given in Robinson & Melrose (1984) break down when the ratio of the observing frequency to the plasma cyclotron frequency is of order unity or less. This occurs for observing frequencies of a few hundred megahertz, with magnetic field strengths of a few hundred gauss.

Some representative plots showing regions of parameter space agreeing with our criteria on the turnover frequency and 5 GHz flux density are shown in Figure 2.5. For a fixed value of emission region size L and electron power-law index δ we are able to constrain N_e and B to within one or two orders of magnitude. However, these constraints on N_e and B are sensitive to the choice of L and δ, so overall we are only able to constrain these parameters to a wide range. For an emission size $3.0 < L < 12.0\,R_*$ and $1.36 < \delta < 2.47$ (corresponding to $-1.0 < \alpha_{\rm thin} < 0.0$), we are able to constrain $1 \lesssim B \lesssim 90\,\text{G}$ and $4 \lesssim \log(N_e) \lesssim 10$. These results are consistent with those found by Metodieva et al. (2017). We find that for $L < 3\,R_*$, $B \ll 1\,\text{G}$ and $\log(N_e) \gg 8$, which we rule out as physically unrealistic parameter combinations. Our parameter estimates are clearly degenerate – general trends we find between the parameters are that larger emission region sizes and shallower spectral indices tend to correspond with higher magnetic field strengths and lower electron number density. Some example model SEDs for coronal parameters consistent with the observed spectral flux densities are shown overlaid with the flux density measurements in Figure 2.4. Our results none the less re-illustrate (as in Metodieva et al. 2017) that precise coronal parameters can be determined with simultaneous low and high-frequency radio measurements, and if the source emission size can be determined independently.

2.6 Summary and future work

We have analysed observations of nine UCDs at ~ 610 and 1300 MHz taken with the GMRT, in order to characterise the low-frequency radio emission of UCDs. We find no evidence for flaring activity at a level above a few millijanskys. However, we observe persistent radio emission from J1314+1320 and 2M 0746+20 at ~ 610 and 1300 MHz, making these the lowest-frequency detections of these sources to date. We find no evidence for significant variability of the persistent emission.

The high brightness temperature and moderate polarisation indicate that gyrosynchrotron radiation from a power-law distribution of mildly-relativistic electrons is the most likely source of the radio emission observed from these UCDs. We apply radiative transfer modelling to J1314+1320, using the expressions for the emission and absorption coefficients for gyrosynchrotron radiation from Robinson & Melrose (1984). The resulting estimates of coronal magnetic field strength and electron density are highly degenerate with emission region sise and electron power-law index, but are none the less consistent with those presented in Metodieva et al. (2017). Future simultaneous observations with a low-frequency array (such as the upgraded GMRT, now with 300 MHz instantaneous bandwidth), and high-frequency array (e.g. the Karl G. Jansky Very Large Array or Australia Telescope Compact Array) will obtain instantaneous snapshots covering the optically thick and thin parts of the SED, yielding more accurate estimates of coronal properties responsible for the radio emission.

Acknowledgements

We extend our thanks to Ian Stevens and Samuel George for informing us about their archival GMRT observations of UCDs re-analysed in this work. AZ thanks Huib Intema and Emil Lenc for helpful discussions regarding data reduction for this work. AZ acknowledges support from an Australian Government Research Training Program (RTP) Scholarship. TM acknowledges the support of the Australian Research Council through grant FT150100099. DLK was supported by NSF grant AST-1412421. PC acknowledges support from the Department of Science and Technology via a SwaranaJayanti Fellowship award (file no. DST/SJF/PSA-01/2014-15). This research was conducted by the Australian Research Council Centre of Excellence for All-sky Astrophysics (CAASTRO), through project number CE110001020. We thank the staff of the GMRT that made these observations possible. GMRT is run by the National Centre for Radio Astrophysics of the Tata Institute of Fundamental Research. This research has made use of NASA's Astrophysics Data System Bibliographic Services. This research has made use of the SIMBAD database, operated at CDS, Strasbourg, France. This research has made use of the VizieR catalogue access tool, CDS, Strasbourg, France (Wenger et al., 2000). The original description of the VizieR service was published in Ochsenbein et al. (2000). This research made use of the following Python software packages: APLpy, an open-source plotting package for Python hosted at http://aplpy.github.com; Matplotlib (Hunter, 2007); NumPy (van der Walt et al., 2011); and Astropy, a community-developed core Python package for Astronomy (Astropy Collaboration et al., 2013).

Chapter 3

ASKAP detection of periodic and elliptically polarised radio pulses from UV Ceti

Andrew Zic,[1,2] Adam Stewart,[1] Emil Lenc,[2] Tara Murphy,[1]
Christene Lynch,[3,4] David L. Kaplan,[5] Aidan Hotan,[6]
Craig Anderson,[6] John D. Bunton,[2] Aaron Chippendale,[2]
Stacy Mader,[7] Chris Phillips[2]

[1]Sydney Institute for Astronomy, School of Physics, University of Sydney, NSW 2006, Australia.
[2]CSIRO Astronomy and Space Science, PO Box 76, Epping, NSW 1710, Australia.
[3]International Centre for Radio Astronomy Research - Curtin University, 1 Turner Avenue, Bentley, WA 6102, Australia.
[4]ARC Centre of Excellence for All Sky Astrophysics in 3 Dimensions (ASTRO 3D).
[5]Department of Physics, University of Wisconsin - Milwaukee, Milwaukee, Wisconsin 53201, USA.
[6]CSIRO Astronomy and Space Science, 26 Dick Perry Avenue, Kensington, WA 6151, Australia.
[7]CSIRO Astronomy and Space Science, Parkes Observatory, PO BOX 276, Parkes NSW 2870, Australia.

This Chapter was published as Zic et al. (2019b), MNRAS, 488, 559. My contributions to this work include writing the majority of the text, leading the data analysis, interpretation of the detections, and producing most figures. Adam Stewart produced Figure 3.1, contributed the Introduction text and part of the description of the observations. Emil Lenc reduced the data, provided code to produce dynamic spectra, and contributed to the description of data reduction.

3.1 Abstract

Active M-dwarfs are known to produce bursty radio emission, and multi-wavelength studies have shown that Solar-like magnetic activity occurs in these stars. However, coherent bursts from active M-dwarfs have often been difficult to interpret in the Solar activity paradigm. We present Australian Square Array Pathfinder (ASKAP) observations of UV Ceti at a central frequency of 888 MHz. We detect several periodic, coherent pulses occurring over a timescale consistent with the rotational period of UV Ceti. The properties of the pulsed emission show that they originate from the electron cyclotron maser instability, in a cavity ~ 7 orders of magnitude less dense than the mean coronal density at the estimated source altitude. These results confirm that auroral activity can occur in active M-dwarfs, suggesting that these stars mark the beginning of the transition from Solar-like to auroral magnetospheric behaviour. These results demonstrate the capabilities of ASKAP for detecting polarised, coherent bursts from active stars and other systems.

3.2 Introduction

Magnetic reconnection events in stellar atmospheres drive powerful flare events causing sudden increases in luminosity from radio through to X-ray bands. Usually these occur in M dwarf stars, and the activity is caused by strong (kilogauss) magnetic fields (Johns-Krull & Valenti, 1996) that can produce flare energies up to 10^3 times that of the Sun (Haisch, 1989). Radio observations of flare stars were first performed in 1958 at megahertz frequencies (Lovell, 1964a), followed by a shift to gigahertz frequencies during the following decades.

Below 5 GHz, radio emission from active M-dwarfs is dominated by coherent emission generated by instabilities in the electron velocity distribution (Dulk, 1985; Bastian, 1990; Melrose, 2017). This coherent emission can be used to probe features such as the structure of the electron velocity distributions (Melrose & Dulk, 1993), and other properties of the emission region such as the density and magnetic field strength (Dulk, 1985; Benz & Güdel, 2010).

UV Ceti is the prototype source of the flare star class (spectral type M5.5), and is part of a binary star system located at a distance of 2.7 pc (Gaia Collaboration et al., 2018). Radio emission from UV Ceti was first reported by Lovell (1963) at a frequency of 240 MHz with flares lasting for 1–10s of minutes that occurred coincidentally with minor optical flares. Subsequent studies, mostly at megahertz frequencies, linked radio flares to flares seen at optical wavelengths, with radio emission following optical outbursts by tens of minutes (Lovell, 1964b; Lovell et al., 1974; Nelson et al., 1979).

With the advent of modern radio interferometers, observations at gigahertz frequencies became dominant in the following decades. Quiescent emission from UV Ceti was detected at millijansky levels at 4.9 GHz, along with a fractional circular polarisation value of 30–50% (Linsky & Gary, 1983). The first dynamic spectra of stellar flares other than those from the Sun were obtained by Bastian & Bookbinder (1987) by observing two flares from UV Ceti at 1.4 GHz, each lasting for approximately 10 minutes with peak flux densities of 200 and 100 mJy. The two coherent flares detected were highly circularly polarised (100 and 70%) with one flare showing evidence of variation within the 41 MHz bandwidth (also see Jackson et al. 1987 for further dynamic spectra).

The longest continuous interferometric observation of UV Ceti was taken by Guedel et al. (1996) for ∼9 h on two occasions at 4.9 and 8.5 GHz, with simultaneous coverage in soft X-rays. The authors found several weakly polarised radio events that began within a few minutes of X-ray flares and then peaked and decayed as the X-ray flares developed gradually, suggesting that the magnetic activity on M-dwarfs is analogous to Solar activity.

Most recently, Lynch et al. (2017) observed UV Ceti at 154 MHz detecting four bursts each lasting ∼30 min and flux densities of between 10–65 mJy. These bursts were only detected in circular polarisation (as well as linear polarisation for the brightest burst), and have estimated brightness temperatures between 10^{13}–10^{14} K. These burst characteristics also led the authors to conclude that the emission was due to the electron cyclotron maser instability, and that the bursts may occur periodically on a time-scale consistent with the rotational period of UV Ceti. Villadsen

Obs. Date (UTC)	Duration (h)	C. Freq. (MHz)	BW (MHz)	Integration Time (s)	Num. of Antennas
2018 Oct 02 12:02	10	888	288	10	28
2019 Mar 07 01:41	10.5	888	288	10	33

Table 3.1: The details of the observations of UV Ceti with ASKAP used in this work. 'C. Freq.' is the central frequency of the observation and 'BW' is the bandwidth.

& Hallinan (2019) have also recently reported the detection of several coherent bursts from UV Ceti in wide-band dynamic spectra. Similarities in the complex morphologies of bursts detected months apart led Villadsen & Hallinan (2019) to suggest that these bursts may be due to periodic pulses of electron cyclotron maser emission. Coherent bursts from active M-dwarfs have proven difficult to interpret within the paradigm of Solar activity (Bastian, 1990; Villadsen & Hallinan, 2019), but these recent results suggest that auroral processes, prevalent in brown dwarfs (Pineda et al., 2017) and magnetised planets (Zarka, 1998) may also be relevant to these stars.

In this paper we present results of two ∼10 hr observations of UV Ceti, separated by ∼5 months, at 888 MHz using the Australian Square Kilometre Array Pathfinder telescope (ASKAP; Johnston et al., 2008; DeBoer et al., 2009). We demonstrate the variability and polarisation capabilities of the telescope by analysing the dynamic spectra of each observation over the 288 MHz ASKAP bandwidth, where we detect periodic coherent bursts associated with UV Ceti recurring on timescales consistent with the rotational period of the star. We investigate the bursts to determine the emission mechanism, and conclude that rotationally-modulated (i.e. pulsed) emission from the electron cyclotron maser instability is the most likely origin. We argue that the time-frequency structure and polarisation properties of the pulses show that they originate along localised magnetic loops within extreme density cavities in the magnetosphere of UV Ceti.

Villadsen & Hallinan (2019) showed that the duty cycle of luminous coherent bursts from active M-dwarfs peaks at 25% at 1–1.4 GHz, a frequency range that is fully observable with ASKAP. This highlights the potential for numerous detections of coherent bursts from active M-dwarfs in future surveys such as the ASKAP Variables and Slow Transients (VAST) survey (Murphy et al., 2013).The excellent data quality from ASKAP will enable detailed analyses of these bursts, allowing these surveys to probe the magnetospheric processes occurring in the population of active M-dwarfs.

3.3 Observations & data reduction

We observed UV Ceti on two epochs (2018-10-02 and 2019-03-07) during ASKAP commissioning tests, with details summarised in Table 3.1. We reduced the data using the Common Astronomy Software Applications package (CASA, McMullin et al., 2007). We observed the primary calibrator PKS B1934 − 638 prior to each observation to calibrate the flux scale, the instrumental bandpass, and polarisation leak-

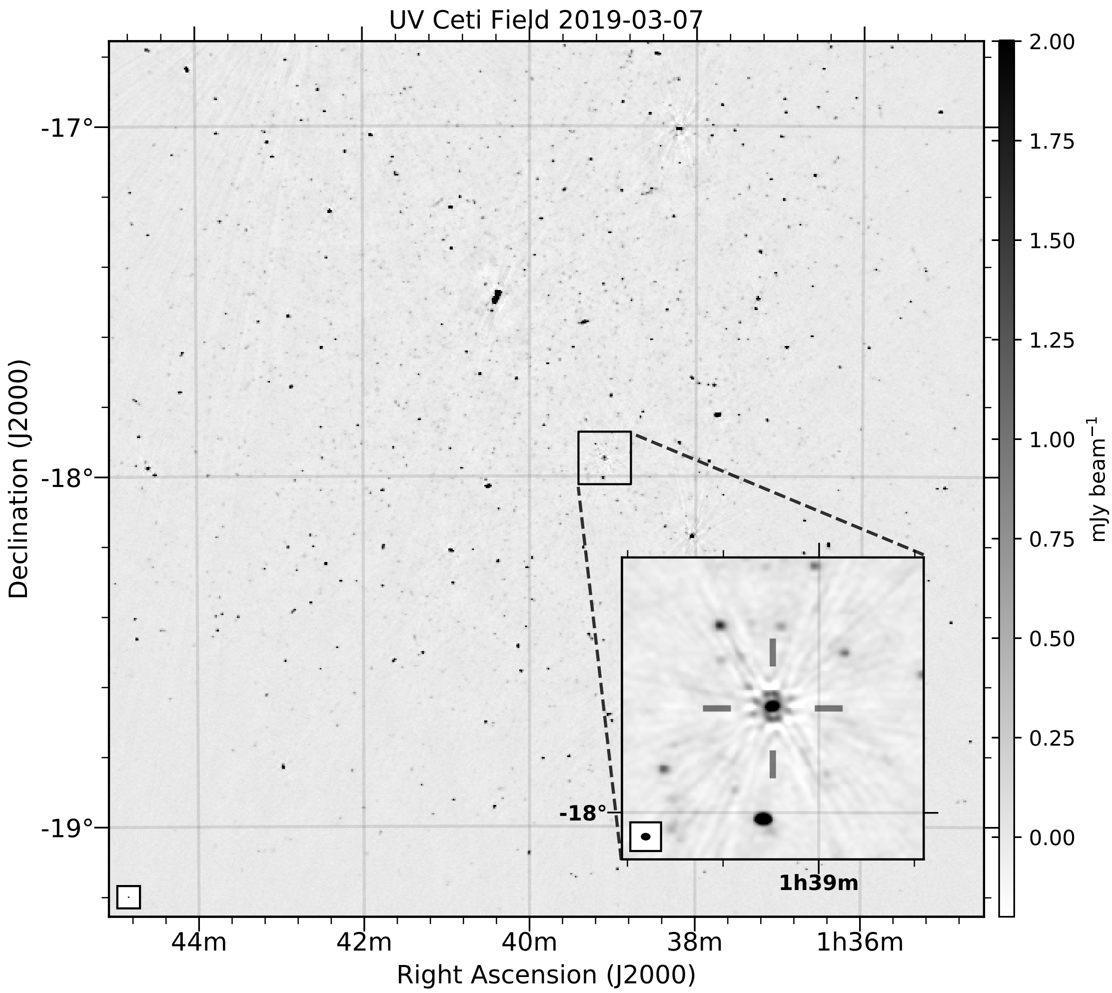

Figure 3.1: Image showing the continuum field containing UV Ceti as observed by ASKAP on 2019-03-07. Note that UV Ceti, which is shown centred in the 'zoom-in' section of the map, has been excluded from the deconvolution process. The synthesised beam is $17\farcs4 \times 13\farcs6$ FWHM at a position angle of 88°. The image peak flux density is 342 mJy beam^{-1} and the image RMS noise is 24 μJy beam^{-1}.

age. On-dish calibrators were used to calibrate the frequency-dependent XY-phase for the 2019-03-07 observation, allowing us to correct for leakage between Stokes Q and V. The observation on 2018-10-02 was not configured to allow correction of frequency-dependent XY-phase, which results in substantial leakage between Stokes Q and Stokes V for this observation. We performed basic flagging to remove radio-frequency interference that affected approximately 6% of the visibility data. We shifted the phase centre of the 2018-10-02 visibility data to the pointing centre for beam 20 (RA=$01^{\mathrm{h}}39^{\mathrm{m}}47\overset{\mathrm{s}}{.}742$ and Dec= $-18°00'30\overset{''}{.}34$) using the task `fixvis`. This was not needed for the 2019-03-07 observation, because we enabled fringe tracking per beam. For each observation, we performed an initial shallow stage of deconvolution using the `clean` task (with briggs weighting and a robustness of 0.5) to assess phase stability. We used the task `gaincal` to perform phase-only self-calibration. The resulting phase corrections were stable as a function of time with only slow variations associated with the longest baselines.

We constructed a mask excluding a $1.5'$ square region centred on UV Ceti using the initial field image. This allowed subsequent deconvolution to model the field sources without removing the time- and frequency-dependent effects of UV Ceti. We then performed a deep clean (20000 iterations) using this mask. We used the multi-scale algorithm (with scales of 0, 5, and 15 pixels and a cell size of $2.5''$) to account for slightly extended sources and two Taylor terms to model sources with non-flat spectra. We excluded baselines shorter than 200λ ($\sim 70\,\mathrm{m}$) to avoid contamination from diffuse emission. Figure 3.1 shows the restored image of the 2019-03-07 observation that achieves a sensitivity of $24\,\mu\mathrm{Jy\,beam}^{-1}$ with a $17.4'' \times 13.6''$ restoring beam. UV Ceti is visible in the continuum image with a peak flux density of $6.3\,\mathrm{mJy\,beam}^{-1}$.

To generate dynamic spectra for UV Ceti, we subtracted the Stokes I field model from the Stokes I visibilities with the CASA task `uvsub` and then phase rotated from the beam centre to the location of UV Ceti at the respective epochs based on GAIA DR2 (RA= $01^{\mathrm{h}}39^{\mathrm{m}}05\overset{\mathrm{s}}{.}8156$ and Dec= $-17°56'50\overset{''}{.}021$, Gaia Collaboration et al., 2018) with the task `fixvis`. We baseline-averaged the subtracted visibilities, using only baselines greater than 200 m to avoid contamination from diffuse emission, for each of the instrumental polarisations.

To produce dynamic spectra for the four Stokes parameters (I, Q, U, V), we combined the complex visibilities for each instrumental polarisation as follows:

$$I = (XX + YY)/2 \tag{3.1}$$
$$Q = -(XY + YX)/2 \tag{3.2}$$
$$U = -(XX - YY)/2 \tag{3.3}$$
$$V = j(XY - YX)/2, \tag{3.4}$$

where (XX, YY, XY, YX) are the instrumental polarisations, and j is the imaginary unit, $\sqrt{-1}$.

The unconventional definitions of Stokes parameters given above arise due to the 45 degree angle of the X and Y feeds relative to the vertical axis at transit (Sault, 2014) and other instrumental factors revealed during commissioning. With the above definitions, the Stokes parameters follow the IAU standard of polarisation.

We verified the polarisation properties of the array with a short observation of the Vela pulsar with the same correlator settings as used in the UV Ceti observations.

Due to the lack of XY-phase calibration for the 2018-10-02 epoch, we can only consider Stokes Q and V in quadrature for this observation, i.e. $\sqrt{Q^2 + V^2}$. Full polarimetric calibration (leakage and frequency-dependent XY-phase) for the observation on 2019-03-07 was possible, which enabled us to generate dynamic spectra for each Stokes parameter. We also generated dynamic spectra of the total fractional (elliptical) polarisation by computing

$$f_p = \frac{\sqrt{Q^2 + U^2 + V^2}}{I} \tag{3.5}$$

for the dynamic spectra from both observing epochs. To avoid spuriously high polarisation fractions generated by noise in the dynamic spectra, we masked any values corresponding with Stokes I flux densities below a 4σ threshold.

To increase the signal to noise in our dynamic spectra, we averaged over 4 frequency channels, giving our dynamic spectra a resolution of 10 s in time, and 4 MHz in frequency. We calculated the RMS noise in our dynamic spectra by taking the standard deviation of their imaginary parts for each Stokes parameter. The average RMS noise of the dynamic spectra across all Stokes parameters was 9.7 mJy for 2018-10-02, and 7.4 mJy for 2019-03-07.

3.4 Results

The dynamic spectra for the 2018-10-02 and 2019-03-07 epochs are shown in Figures 3.3 and 3.5 respectively, and their frequency-averaged light-curves are shown in Figure 3.2. To measure the flux density uncertainties for each 10 s light-curve sample, we took the standard deviation of the imaginary part of the complex light-curve. We detect several highly polarised pulses in both observing epochs, with a peak flux density in the dynamic spectra of 160 ± 10 mJy in the 2018-10-02 epoch, and 139.7 ± 7.6 mJy in the 2019-03-07 epoch.

3.4.1 Emission properties

2018-10-02: Temporal and spectral structure

We detected three pulses in the 2018-10-02 epoch: a faint pulse with a peak flux density of 59 ± 10 mJy (labelled 18-1A), followed by a 160 ± 10 mJy pulse occurring $\sim$ 45 min after the first faint pulse (labelled 18-1B). Another 70 ± 10 mJy pulse (labelled 18-1C) occurs $\sim$ 5.4 h after 18-1A. In addition, the light-curve appears to show the tail end of a pulse that peaked just before the observation started, and about 5.4 hours before the tail of 18-1B. Hereafter, we refer to the pulses by their labels, which are shown in the Stokes I panel of Figure 3.3.

All three fully-detected pulses have a double-peaked profile, with more complex sub-structure evident within the dynamic spectrum of 18-1B. There is a gradual increase in flux density from $t \sim 8$ h until 18-2A peaks at $t \sim 9.4$ h. Preceding

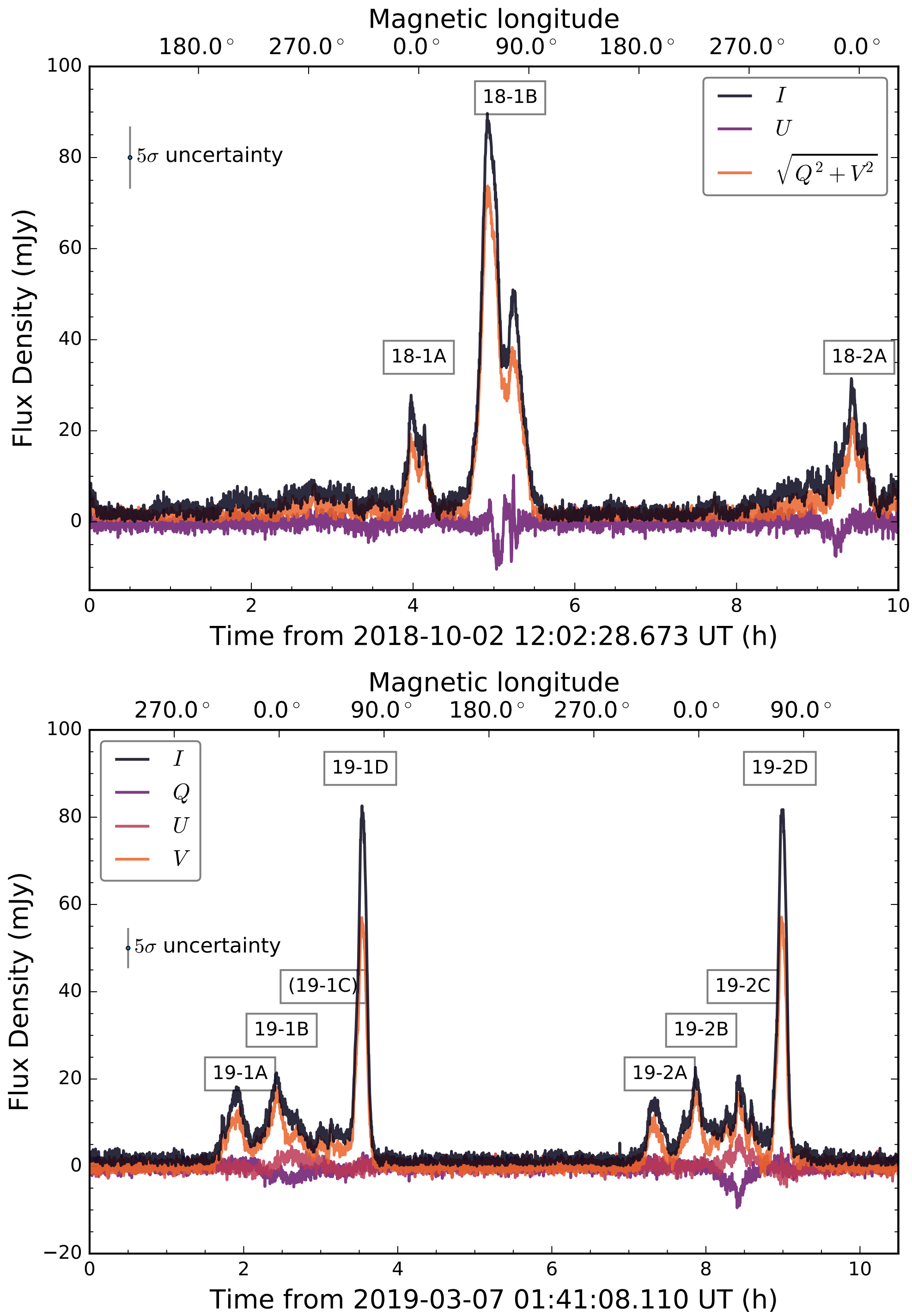

Figure 3.2: Frequency-averaged light-curve for UV Ceti in the 2018-10-02 epoch (top panel) and 2019-03-07 epoch (bottom panel). Sub-structure in total intensity and in the Stokes parameters are evident in the pulses. Typical 5σ uncertainties are labelled in each plot. The lower abscissae show the time in hours from the observation start, and the upper abscissae show the relative magnetic longitude, as described in Section 3.4.3.

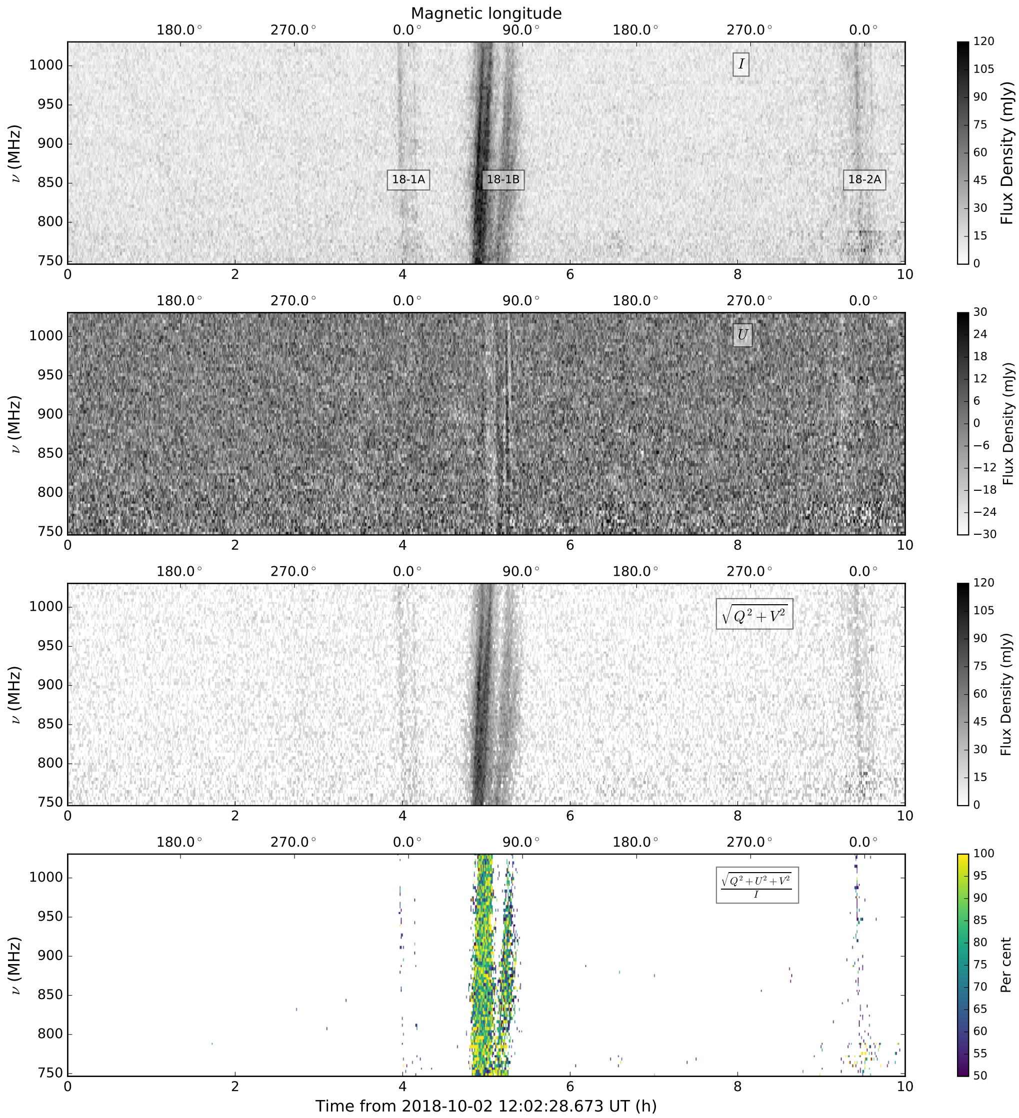

Figure 3.3: Dynamic spectrum of UV Ceti in Stokes I, U, $\sqrt{Q^2 + V^2}$, and total fractional polarisation $\sqrt{Q^2 + U^2 + V^2}/I$. The dynamic spectra have been averaged to 4 MHz in frequency to improve the signal-to-noise. Total fractional polarisations that correspond with Stokes I flux densities below a 4σ threshold have been blanked. To aid clarity, the pulses have been labelled 18-1A, 18-1B, and 18-2A. The similar drift rate and flux density of pulses 18-1A and 18-2A is evident. As in Figure 3.2, the lower abscissae show the time in hours from the observation start, and the upper abscissae show the relative magnetic longitude, as described in Section 3.4.3.

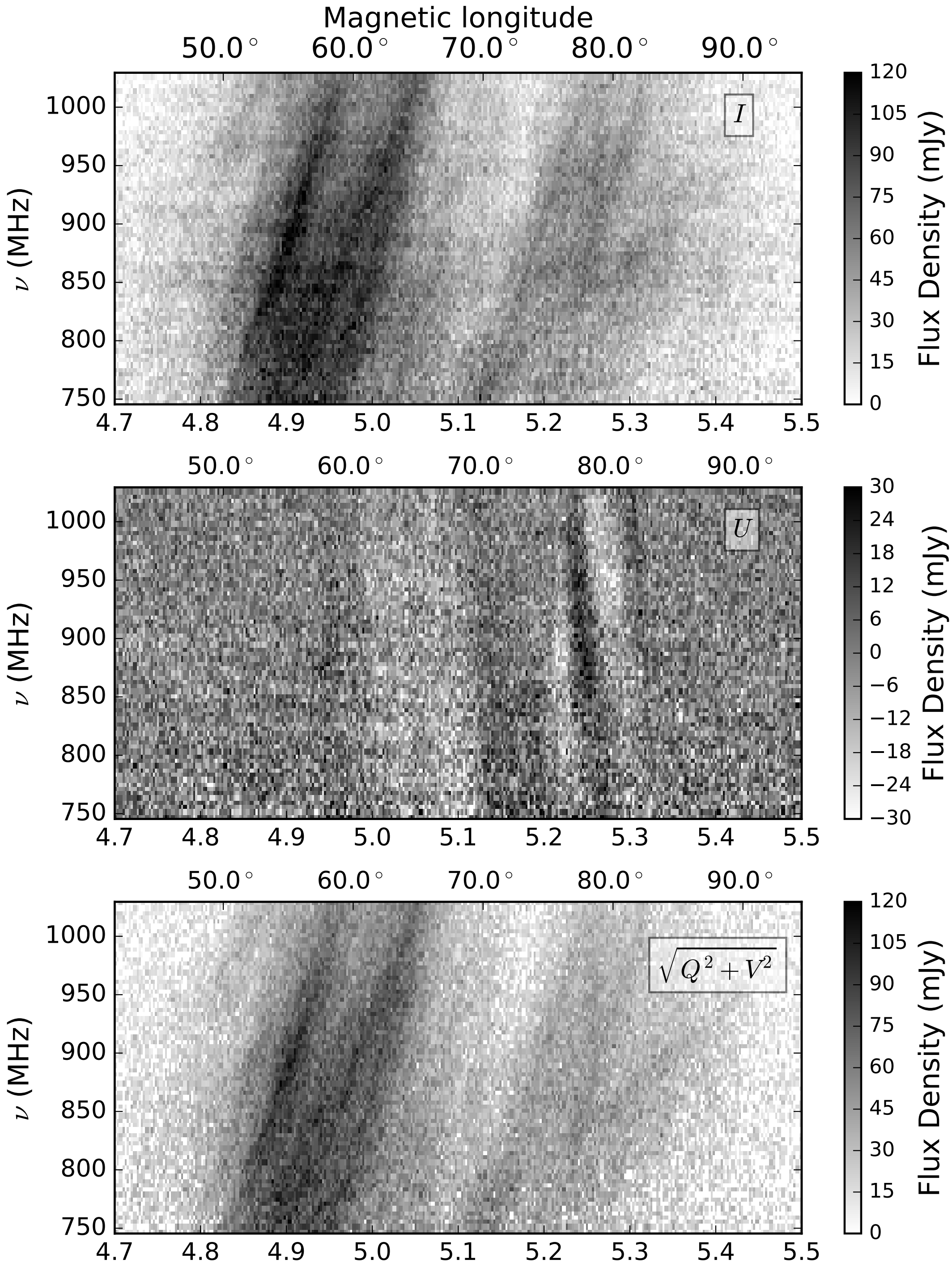

Figure 3.4: Detail of the pulse 18-1B in the 2018-10-02 epoch, in Stokes I, U, and $\sqrt{Q^2 + V^2}$. Complex sub-structure in total intensity, and in polarisation is evident. Particularly notable is the banding present in Stokes U, which appears to be drifting in an opposite direction to the bulk frequency drift of the pulse. As in Figure 3.3, upper abscissae show the relative magnetic longitude.

18-1A, there is only a marginal flux density enhancement at $t \sim 2.8\,\mathrm{h}$. Apart from the preceding behaviour, 18-1A and 18-2A show a similar temporal profile.

All three pulses exhibit a bulk frequency drift across the bandwidth of our observations. To determine the bulk frequency drift rates of the pulses, we fit a simple model of a series of drifting top-hat pulses to the observed dynamic spectra using a Markov Chain Monte Carlo (MCMC) sampler (EMCEE[1]; Foreman-Mackey et al., 2013). We set uniform priors on the parameters of each pulse (central time, duration, amplitude, drift rate, and periodicity), within conservative large ranges determined by visual inspection.

We found that 18-1B was best fit by two components: the earlier component with a drift rate of $\dot{\nu} = 0.75 \pm 0.03\,\mathrm{MHz\,s^{-1}}$, and the later component with $\dot{\nu} = 0.60^{+0.03}_{-0.02}\,\mathrm{MHz\,s^{-1}}$. We find that 18-1A and 18-2A have consistent drift rates of $-1.30^{+0.03}_{-0.02}\,\mathrm{MHz\,s^{-1}}$ and $-1.30 \pm 0.03\,\mathrm{MHz\,s^{-1}}$ respectively.

2019-03-07: Temporal and spectral structure

We detect eight clearly separated pulses in the 2019-03-07 epoch. These pulses appear to be within two distinct sets separated by about 5.4 h. We label the pulses in the first set as 19-1A, 19-1B, (19-1C), 19-1D, and 19-2A, 19-2B, 19-2C, 19-2D in the second set. Each set of pulses has three faint pulses with peak flux densities ranging from $16.2 - 51.6 \pm 7.6\,\mathrm{mJy}$, followed by a bright pulse with a peak flux density of $136.4 \pm 7.6\,\mathrm{mJy}$ in the first set, and $139.7 \pm 7.6\,\mathrm{mJy}$ in the second set. (19-1C) is not clearly detected in the high-resolution dynamic spectra, but becomes apparent after further averaging in time and frequency. We label it within brackets to indicate its marginal status.

Each of the three faint pulses in each set shows different temporal structure to each other. There is some change in the temporal structure of 19-1A, C and their corresponding pulses 19-2A, C, although 19-1B appears to maintain a more steady, sharply-peaked temporal profile in the corresponding pulse 19-2B. The faint pulses in each set (19-1A, B, C and 19-2A, B, C) appear to be regularly separated, by approximately 32 min.

Following the MCMC procedure outlined in Section 3.4.1, we measured the drift rates and other parameters of the pulses. All faint pulses (19-1A, B, C and 19-2A, B, C) show a drift rate consistent with $-1.300\,\mathrm{MHz\,s^{-1}}$, with typical uncertainties in the range of $0.003 - 0.005\,\mathrm{MHz\,s^{-1}}$. Pulse 19-2A shows quasi-periodic striations that repeat approximately once every $1.8 - 1.9\,\mathrm{min}$, similar to quasi-periodic oscillations from active M-dwarfs reported by Gary et al. (1982); Lang & Willson (1986), and Bastian et al. (1990). The oscillations in 19-2A are evident in Figure 3.6.

Pulses 19-1D and 19-2D are very similar in their peak flux densities, and in their temporal sub-structure, both containing two closely-spaced components with slightly differing frequency drift rates. The bulk drift rates of 19-1D and 19-2D are both consistent with a value of $1.000\,\mathrm{MHz\,s^{-1}}$, with uncertainties in the range of $0.002 - 0.004\,\mathrm{MHz\,s^{-1}}$.

[1] http://dfm.io/emcee/

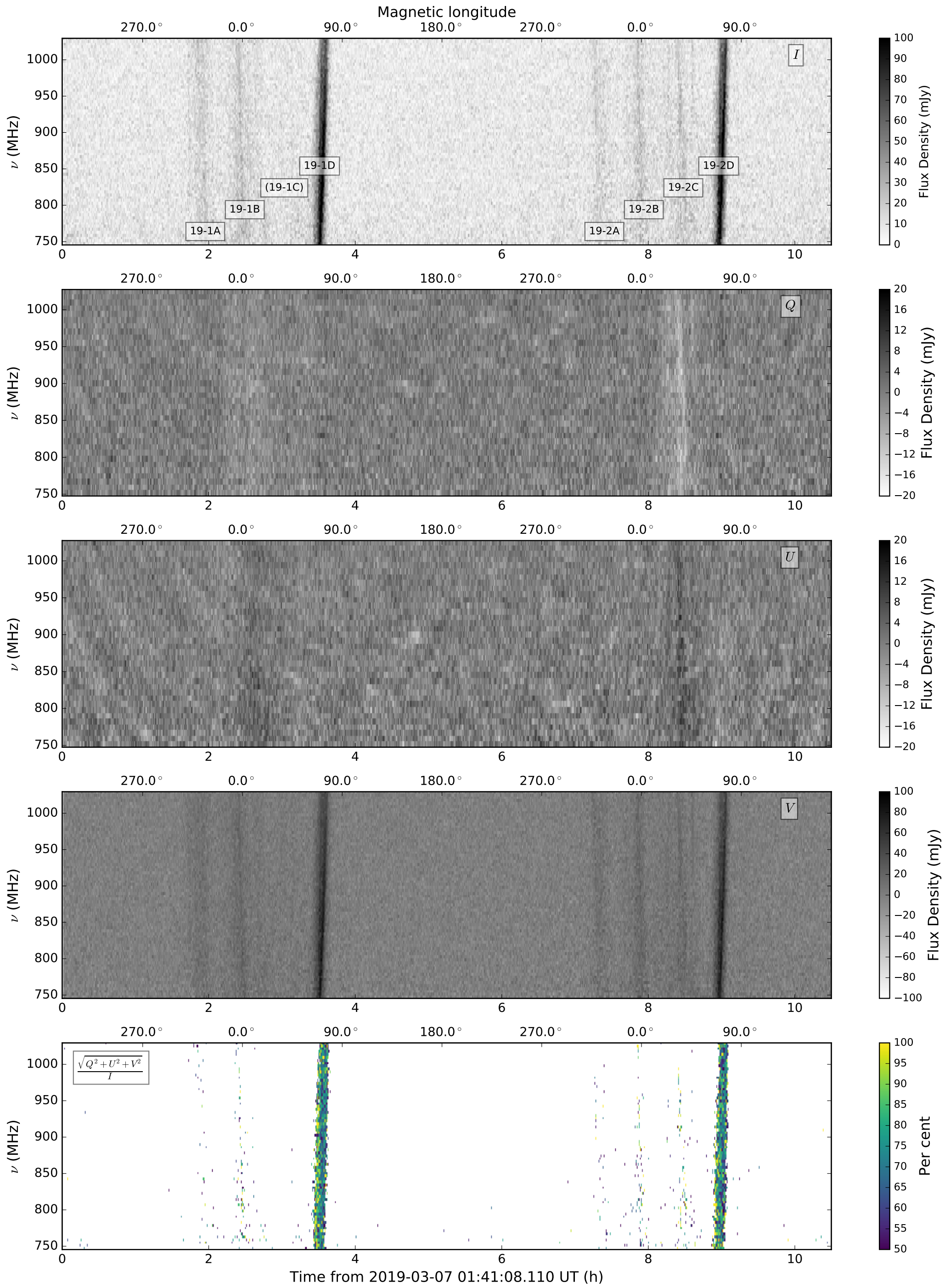

Figure 3.5: Full-Stokes dynamic spectrum of UV Ceti. The dynamic spectra have been averaged to 4 MHz in frequency in Stokes I and V, and to 60 s and 16 MHz in Stokes Q and U to improve sensitivity. The bottom panel shows total fractional polarisation similarly to Figure 3.3. The pulses have been labelled 19-1A, 19-1B, (19-1C), 19-1D, 19-2A, 19-2B, 19-2C, 19-2D. Pulse (19-1C) is within brackets to indicate its marginal status, but becomes evident after further averaging of the dynamic spectrum. Upper abscissae show relative magnetic longitude as described in Section 3.4.3.

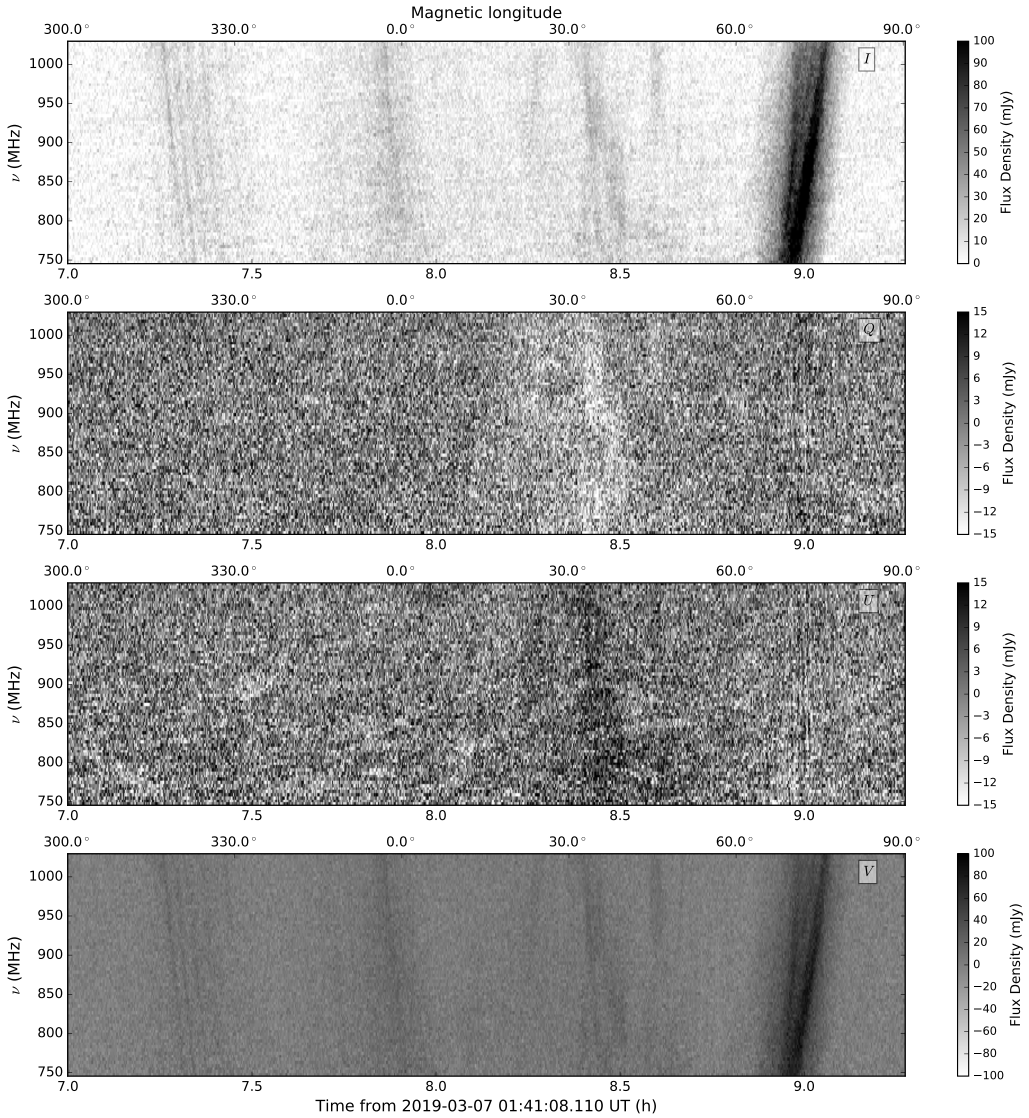

Figure 3.6: Detail of the pulses 19-2A, 19-2B, 19-2C, and 19-2D in Stokes I, Q, U, and V. The varying sub-structure, but similar overall drift rate of 19-2A, B, and C is evident. Pulse 19-2C exhibits linear polarisation with little dependence on frequency. As in Figure 3.5, upper abscissae show relative magnetic longitude.

Polarisation

In each epoch, the detected pulses are highly circularly polarised, averaging about 70% circular polarisation and reaching up to 100%. Unfortunately due to the lack of cross-hand phase calibration in the 2018-10-02 epoch, determining the sense of circular polarisation is difficult. However, in the 2019-03-07 epoch, the Stokes V emission is consistently positive-valued, indicating that it is RCP. This is consistent with the majority of coherent bursts reported from UV Ceti in the literature (e.g. Villadsen & Hallinan, 2019; Lynch et al., 2017; Bastian & Bookbinder, 1987); however, some LCP bursts have been reported (Lynch et al., 2017).

We detect linearly polarised emission associated with some of the pulses, at an average level of about 15% of the total intensity. Inspection of the Stokes U dynamic spectrum shows two linearly-polarised components in pulse 18-1B. The first Stokes U component of 18-1B is largely positive-valued, exhibiting very little dependence on frequency. The second component in Stokes U exhibits striations drifting in frequency in an opposite direction to the enveloping pulse. This behaviour is most evident in Figure 3.4. There is also a weak, negative Stokes U signal associated with 18-2A near $t = 9.4\,\mathrm{h}$ that also shows little dependence on frequency.

In the 2019-03-07 epoch, we detect weak linearly polarised emission associated with pulses 19-1B and 19-2C. Like the linear polarisation in 18-2A, the linear polarisation in 19-1B and 19-2C show little dependence on frequency. There is also some marginal, rapidly-striating linear polarisation associated with pulses 19-1D and 19-2D (evident in Figures 3.5 and 3.6).

The detection of pulses in Stokes Q and U along with V implies that the emission is elliptically polarised – a rare occurrence in nature that is generally only seen in pulsars (e.g. Melrose, 2017) and magnetised planets (e.g. Zarka, 1998; Dulk et al., 1994; Boudjada & Lecacheux, 1991; Fischer et al., 2009). We are aware of two other reports of elliptically polarised stellar radio emission from the literature: Lynch et al. (2017) also detected elliptically polarised emission from UV Ceti with the Murchison Widefield Array at 154 MHz, and Spangler et al. (1974) detected elliptically polarised emission from AD Leo at 430 MHz.

The differing structure of the linearly polarised emission compared with the Stokes I and V emission strongly suggests that these polarisation components are not instrumental in origin. Nonetheless we conducted a number of checks to verify that the linear polarisation is legitimate.

We inspected bright sources around the UV Ceti field, and found that in general, within $40'$ of the field centre (corresponding with the half-width at half-maximum of the primary beam), leakage from Stokes I to V is $\sim 0.1\%$, Q to I is $\lesssim 0.5\%$, and U to I is $\lesssim 1.5\%$. Towards the pointing centre, the leakage values decrease below the noise floor. These leakage fractions are at least 10 times lower than the measured degree of linear polarisation from UV Ceti ($\sim 15\%$). We obtain similar results with the short Vela observation reported above.

We also imaged the UV Ceti field during times of apparent linearly polarised emission. These images show a linearly-polarised point source associated with UV Ceti, and show that the emission is not an artefact associated with radio-frequency interference, or sidelobe confusion from a bright field source. At these times, other field sources show no spurious deviations from their baseline leakage values reported

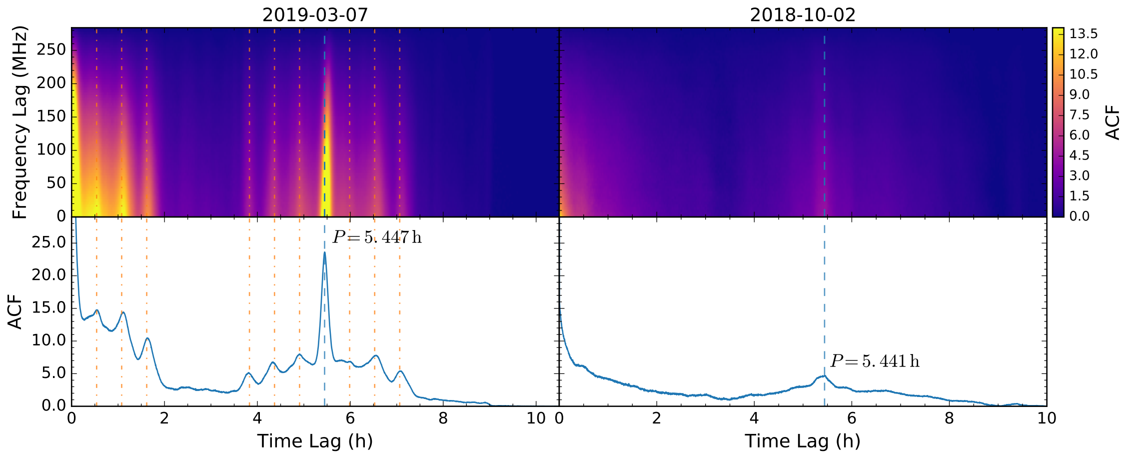

Figure 3.7: Two-dimensional autocorrelation function, and the corresponding zero frequency-lag components for the 2019-03-07 (left panels) and 2018-10-02 epochs (right panels). Dashed lines indicate the time lag of the major peak in the autocorrelation, which measures the periodicity of the pulses. The dash-dotted lines in the autocorrelation of 2019-03-07 are spaced every 0.539 h from the zero time lag component, and around the major peak at a time lag of 5.447 h, and show the quasi-periodic nature of the pulses 19-1A, B, C and 19-2A, B, and C.

above. With the results of these tests, we are confident that the linearly polarised emission is intrinsic to UV Ceti, and not instrumental in origin.

3.4.2 Derived pulse period

The repetitive nature of the detected emission over the rotational period of UV Ceti strongly suggests that the emission is rotationally-modulated, pulsed, emission from highly-beamed radio sources, as opposed to stochastic bursts or flares. To test the periodicity of the pulses, we computed the two-dimensional autocorrelation function of the Stokes I dynamic spectra, and measured the time lag at the peak along the zero frequency-lag component of the autocorrelation.

The 2018-10-02 observation is dominated by the central bright burst, which does not repeat in our observation. To avoid this dominating the autocorrelation function, we masked the region from $t = 4.6 - 5.8\,\mathrm{h}$ and replaced it with artificial complex Gaussian noise with the same properties as measured in the region of the dynamic spectrum with no detectable emission $t = 0.3 - 1.5\,\mathrm{h}$. The resulting autocorrelation function (right panels of Figure 3.7) shows a significant peak at $5.441 \pm 0.035\,\mathrm{h}$, in the zero frequency-lag component. Similarly, the autocorrelation of the (unfiltered) 2019-03-07 epoch (left panels of Figure 3.7) shows a strong zero frequency-lag peak centred at $5.447 \pm 0.008\,\mathrm{h}$. Note that the quoted uncertainties are derived from the marginalised distribution of the pulse period from the top-hat pulse model described in Section 3.4.1.

The pulse periods measured between the two epochs are consistent with one another, and consistent with the $5.4432 \pm 0.0072\,\mathrm{h}$ period measured by Barnes et al. (2017). We note that this disambiguates which component of the L726-8AB binary the emission originates from – the primary component BL Ceti (L726−8A) is also known to be active at radio frequencies (e.g. Gary et al., 1982), and is separated from UV Ceti by $\sim 4''$, well below the $\sim 15''$ resolution of our ASKAP observations. However, BL Ceti has a rotational period of 5.832 ± 0.012 h (Barnes et al., 2017).

Along with the 5.447 ± 0.008 h periodicity revealed by the autocorrelation of the 2019-03-07 observation, there are also three minor peaks in the autocorrelation spaced every 0.539 h from the zero time-lag component, and to either side of the primary period of 5.447 ± 0.008 h. This gives strong evidence for the quasi-periodic nature of the faint pulses 19-1A, B, C and 19-2A, B, C.

3.4.3 Comparison of the two epochs

We find notable similarities between the pulses occurring in both epochs when inspecting the dynamic spectra side by side. Most striking are the faint pulses occurring in both epochs: 18-1A, 18-2A, and 19-1A, B, C, 19-2A, B, C – these pulses all have very similar drift rates ($\sim 1.3 - 1.4\,\mathrm{MHz\,s^{-1}}$, virtually indistinguishable within the bandwidth of our observations), durations (~ 12 min), and are similar in their average flux densities ($\sim 40 - 50$ mJy). However, in the 2019-03-07 epoch, three faint pulses with equal drift rates occur every rotation, where as in 2018-10-02 only one faint, negative-drifting pulse occurs per rotation. Pulses 19-1B and 19-2B are morphologically most similar to the faint pulses 18-1A and 18-2A occurring once per rotation in the 2018-10-02 epoch, 18-1A and 18-2A. Furthermore, the time difference between 19-1B and 19-1D, and 19-2B and 19-2D (~ 60 min) is similar to the time difference between 18-1A and 18-1B (~ 50 min).

While there are some morphological similarities between the bright pulses in both epochs, the bright burst in 2018-10-02 has a slower bulk drift rate, a longer duration, and overall a more complex morphology to the bright pulses present in 2019-03-07. Nonetheless, similarities between the pulses in both epochs suggests that some of the pulses originate from source regions that have remained relatively stable over timescales of several months. This suggestion was also made by Villadsen & Hallinan (2019) to explain the similar morphologies of several bursts detected from UV Ceti, despite months-long separation between observations. In particular, we suggest that the similar morphology, flux density, and drift rate of pulses 18-1/18-2A and 19-1/19-2B, along with their similar time gap from the subsequent bright pulses 18-1B, and 19-1/19-2D, indicates that they originate from the same source region along a stable magnetic loop.

Under the assumption that they are the from same source region, and that their host magnetic loop has not drifted significantly in magnetic longitude, we can set the peak times of 18-1A and 19-1B as our reference time for zero longitude for the 2018-10-02 and 2019-03-07 epochs, respectively. We use the 5.447 ± 0.008 h periodicity measured from the 2019-03-07 epoch to calculate the relative magnetic longitude from the set reference time. This enables us to more closely analyse the similarities and differences of the sets of pulses we detect in our two observing epochs. Relative magnetic longitudes are shown in the upper abscissae of Figures 3.2, 3.3, 3.4, 3.5, 3.6, and 3.8.

Figure 3.8 gives a comparison of the pulses 18-1A, B with 19-1A, B, C and 19-2A,

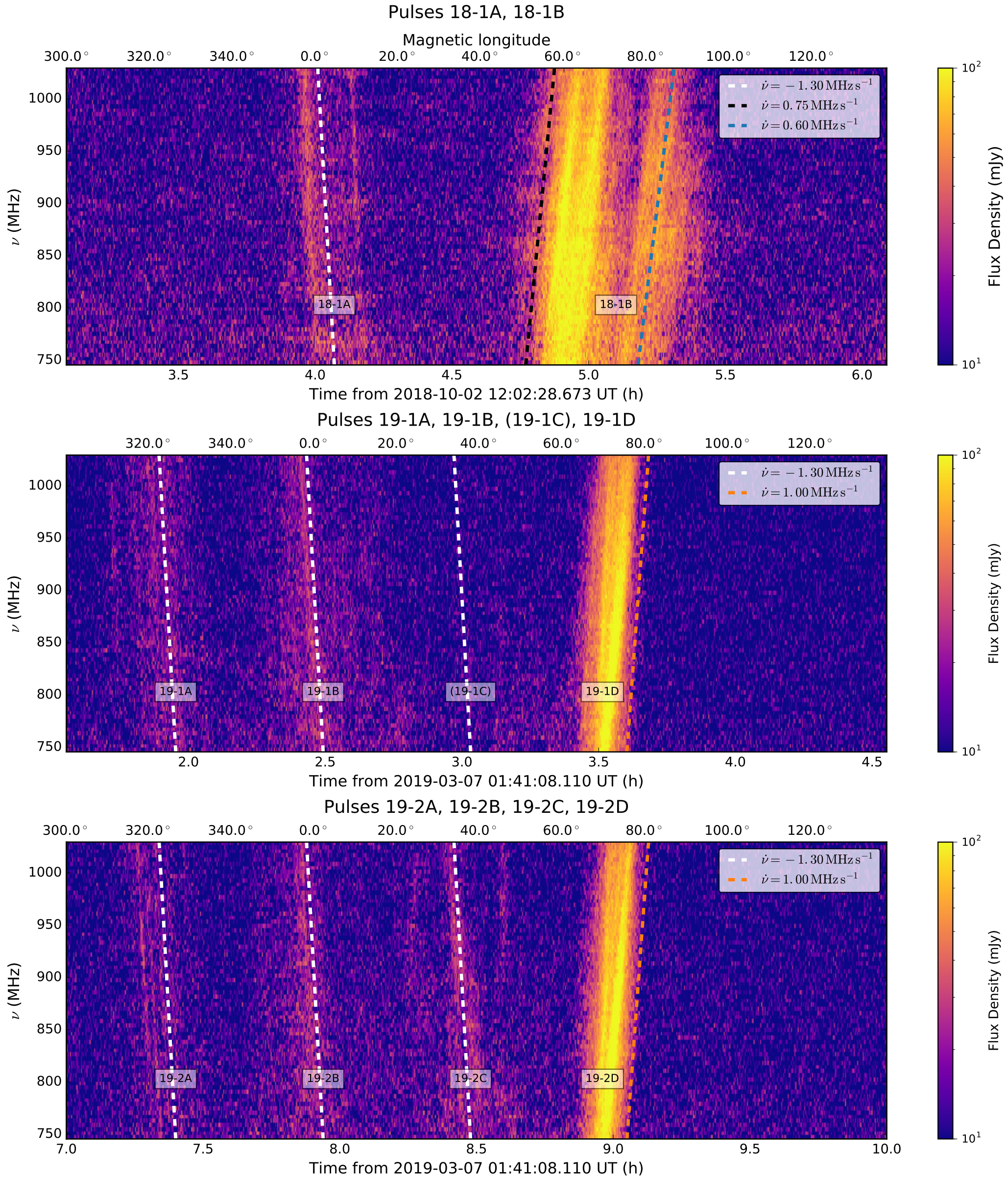

Figure 3.8: Comparison of pulses from 2018-10-02 and 2019-03-07, at the same magnetic longitude (rotational phase). The pulses are labelled according to their labels designated in Section 3.4.1. The dashed lines indicate the locations and drift rates of the pulses. The white dashed lines are spaced every 0.539 h in the 2019-03-07 panels, consistent with the periodicity of these pulses demonstrated by the autocorrelation function shown in Figure 3.7. The similar structure and arrangement of the pulses between the 2018-10-02 and 2019-03-07 epochs is evident. Upper abscissae show relative magnetic longitude for each of the pulses, assuming a fiducial zero-point at the high-frequency peak of 19-1/19-2B, and 18-1A. To highlight pulse structure on different flux density scales, the colourmap has been logarithmically scaled between 10–100 mJy.

B, C. Dashed lines in this figure indicate the location and drift rates of the pulses. This figure highlights the similar drift rates of the faint pulses in both epochs. The evolution in drift rate and relative magnetic longitude from 18-1B to 19-1D and 19-2D is also evident, along with the quasi-periodic nature of pulses 19-1A, B, C and 19-2A, B, C.

3.5 Discussion

3.5.1 Origin of the emission

Incoherent emission has a maximum brightness temperature of $10^{11} - 10^{12}\,\mathrm{K}$ due to inverse Compton scattering (Kellermann & Pauliny-Toth, 1969), and so any radio emission with a brightness temperature persistently exceeding this limit must be coherent in nature (disregarding relativistic Doppler boosting). We used Equation 14 from Dulk (1985) to calculate the brightness temperature T_b as follows:

$$T_b = \frac{1}{2k_B} S_\nu \left(\frac{c}{\nu}\right)^2 \left(\frac{d}{l}\right)^2, \tag{3.6}$$

where k_B is the Boltzmann constant, S_ν is the flux density in Jy, c is the speed of light, ν is the observing frequency, d is the distance to the source, and l is the emission region size. Assuming the radio emission is beamed and rotationally modulated (see Section 3.4.2) we can use the projected rotational velocity of $32.2\,\mathrm{km\,s^{-1}}$ of UV Ceti (Barnes et al., 2017), and an upper limit on the duration of all pulses of 20 min, to set an upper limit on the emission region size for each pulse of $3.6 \times 10^9\,\mathrm{cm} = 0.50\,R_{\mathrm{Jup}}$, where R_{Jup} is a Jupiter radius. Using this upper limit on the source size, we calculated a lower limit of the brightness temperature on the pulses from both epochs.

We find that the brightness temperature lower limits are in the range of $0.22 - 4.3 \times 10^{13}\,\mathrm{K}$, exceeding the $10^{12}\,\mathrm{K}$ inverse-Compton limit (Kellermann & Pauliny-Toth, 1969), therefore indicating that the emission is coherent. This conclusion is also supported by the high degree of circular and elliptical polarisation (up to 100%), and the complex temporal and spectral structure of the pulses.The periodicity shows that the pulses originate from persistent, highly beamed sources whose emission crosses our line of sight as the star rotates, confirming suggestions by Lynch et al. (2017) and Villadsen & Hallinan (2019).

The two emission mechanisms that are generally invoked to explain stellar coherent radio bursts are plasma emission (Dulk, 1985) and the electron cyclotron maser instability (ECMI; Treumann, 2006). The ECMI operates most efficiently when $\nu_p/\nu_c \ll 1$ i.e. in low-density, highly magnetised plasmas. Here, ν_c is the electron cyclotron frequency, given by

$$\nu_c = eB/2\pi m_e c \approx 2.8B\,\mathrm{MHz}. \tag{3.7}$$

The emission is expected to be very narrow-band, centred around the electron cyclotron frequency and possibly its harmonics. In favourable conditions for the ECMI, when the ratio of the plasma frequency

$$\nu_p = \sqrt{n_e e^2/\pi m_e} \approx 9\sqrt{n_e}\,\mathrm{kHz}, \tag{3.8}$$

to the cyclotron frequency is small (i.e. $\nu_p/\nu_c \ll 1$), the emission is expected to be polarised in the free-propagating extraordinary mode of the birefringent plasma (x-mode), and is beamed at angles nearly perpendicular to the magnetic field (Treumann, 2006). However, the ECMI can also operate with reduced efficiency when a weaker condition, $\nu_p/\nu_c \leq 1$, is met. In this instance, polarisation in the ordinary mode (o-mode) is possible. When the line-of-sight component of the magnetic field is directed towards the observer, then x-mode corresponds with RCP and o-mode with LCP. In the opposite orientation, x-mode corresponds with LCP and o-mode with RCP. Therefore, with knowledge of the magnetic field geometry, the observed sense of polarisation can be used to determine the magneto-ionic mode of the emission.

Plasma emission occurs at the local plasma frequency and its second harmonic; higher frequencies/harmonics are expected to be absorbed via gyroresonance or free-free absorption (Dulk, 1985). Plasma emission at the fundamental mode is expected to be polarised in the o-mode, and mildly polarised at the second harmonic (Melrose et al., 1978; Melrose & Dulk, 1993).

In Section 3.5.3, we use the presence of linear polarisation in the pulses to place an upper limit on the electron number density of $n_e \lesssim 41\,\mathrm{cm}^{-3}$. This density limit corresponds to plasma frequencies less than 54 kHz, well below our observing frequency. Furthermore, all the detected pulses in 2019-03-07 are RCP, indicating emission consistently from either the x or o-mode. Kochukhov & Lavail (2017) showed that the magnetic north pole of UV Ceti is inclined towards Earth, meaning that the emission is most likely to be from the northern hemisphere of the UV Ceti magnetosphere i.e. where the line-of-sight magnetic field component is directed towards the observer. This indicates that the emission is in the x-mode.

Elliptical polarisation is also indicative of radiation in the x-mode, as argued in the case of elliptically polarised Jovian decametric radiation (Melrose & Dulk, 1991, 1993; Dulk et al., 1994). The presence of elliptically polarised emission in both epochs gives further evidence that the emission is emitted in the x-mode.

Together, polarisation properties of the pulses in both epochs favour emission in the x-mode from the northern magnetic hemisphere of UV Ceti, showing that the emission is from the ECMI. This is consistent with recent detections of bursts from UV Ceti by Lynch et al. (2017) and Villadsen & Hallinan (2019), and more broadly with the nature of periodic radio pulses from other auroral emitters (e.g. Lynch et al., 2017; Hallinan et al., 2007; Trigilio et al., 2000; Zarka, 1998).

Using Equation 3.7, and assuming emission in the second harmonic, the local magnetic field strength at the emission regions is in the range of $133 - 184\,\mathrm{G}$, or $266 - 368\,\mathrm{G}$ assuming the emission is in the fundamental mode. Assuming a purely dipolar magnetospheric geometry with mean surface magnetic field strength of 6.7 kG as a first order approximation, based on Zeeman Doppler Imaging of UV Ceti, (Kochukhov & Lavail, 2017), then this implies source altitudes of $\sim 3.3 - 3.7\,R_*$ (or $2.6 - 2.9\,R_*$ if the emission is in the fundamental mode), where R_* is the stellar radius ($1R_* = 0.159 \pm 0.006\,R_\odot$; Kervella et al., 2016).

3.5.2 Origin of frequency drift

Wide-band dynamic spectra of the ultra-cool dwarfs (UCDs) TVLM 513−46, and 2M 0746+20 presented by Lynch et al. (2017) exhibited periodic radio pulses with a linear frequency drift, similar to our observations of pulses from UV Ceti. Lynch et al. (2017) explained that the drifting features in their dynamic spectra are caused by ECMI emission along a few localised magnetic loops in the stellar magnetospheres. This frequency drift arises due to the fact that ECMI emission emits in a narrow frequency range about the electron cyclotron frequency, determined by the local magnetic field strength (see Equation 3.7). Source regions at different altitudes along an active magnetic loop will have differing local magnetic field strengths and therefore different emission frequencies. As the star rotates, the frequency-dependent ECMI emission beam will cross the line of sight at different orientations which depend on the emission altitude, and therefore on observing frequency. We suggest that a similar geometrical effect is responsible for the observed frequency drifts in our dynamic spectra, although a detailed modelling procedure of the magnetospheric geometry responsible for the pulses is beyond the scope of this work.

3.5.3 Interpretation of linear polarisation

Melrose & Dulk (1991) discussed possible causes for the linear polarisation in Jovian decametric emission observed e.g. by Dulk et al. (1994) and Boudjada & Lecacheux (1991). They concluded that the presence of elliptically polarised emission implies extremely low plasma densities in the emission region. Equation 14 from Melrose & Dulk (1991) gives an upper limit on the electron density when the emission is elliptically polarised:

$$n_e \lesssim \alpha(\nu/25\,\mathrm{MHz}), \tag{3.9}$$

where α is a geometrical factor of order unity and ν is the observing frequency. For our highest observing frequency (1030 MHz), and taking $\alpha = 1$, this gives an approximate upper limit on the electron density of $41\,\mathrm{cm}^{-3}$.

We can compare this density to an order-of-magnitude estimate of the expected density at a source altitude of $\sim 3.7\,R_*$ (see Section 3.5.1) as follows. We assume a simple exponential coronal density model, adopting a scale height of $0.48\,R_*$ calculated by Villadsen & Hallinan (2019) using a constant-gravity hydrostatic equilibrium model, and take an average coronal base density of $10^{10.5}\,\mathrm{cm}^{-3}$ (similar to densities inferred for other active M-dwarfs; Ness et al., 2004). This gives an expected electron density on the order of $10^8\,\mathrm{cm}^{-3}$ at the source altitudes.

Our upper limit of $n_e \lesssim 41\,\mathrm{cm}^{-3}$ is much lower than this order-of-magnitude estimate of the electron density, and is unlikely to be explained by permitting a more complex model (e.g. removing the assumption that the magnetosphere is strictly dipolar). A plausible explanation for our strong upper limit on electron density is that the emission arises from an extreme density cavity, analogous to the cavities present around the emission regions of Earth's auroral kilometric radiation (AKR), generated by powerful magnetic field-aligned electric fields (Zarka, 1998; Ergun et al., 2000). Melrose & Dulk (1991) concluded that densities low enough to permit elliptically polarised emission from active stars or the Sun are highly unlikely to occur due to high average coronal electron densities, highlighting the remarkable nature of this emission. While the extremely low density of the source region can be inferred from present theory, further theoretical investigation is required to justify (or avoid) the extraordinary density contrast between the source region and the ambient corona that is required.

Although ECMI has often been the favoured mechanism to explain stellar coherent bursts, a common difficulty encountered is the expected absorption of ECMI emission by the overlying plasma in the gyroresonance harmonic layers (Dulk, 1985). Assuming a dipolar magnetosphere and emission in the second harmonic, our emission region is at altitudes between $\sim 3.3 - 3.7\,R_*$ (see Section 3.5.1) – a radial extent of $\sim 0.4\,R_*$. The third gyroresonance layer, where $B = 2B_{\rm src}/3$, spans altitudes of $\sim 3.8 - 4.2\,R_*$. Here, $B_{\rm src}$ is the source magnetic field strength. The presence of elliptical polarisation across the entire bandwidth of some pulses requires that the associated cavity extends at least $0.4\,R_*$. It therefore seems plausible that the cavity may extend an additional $0.5\,R_*$ in altitude, such that it reaches the third gyroresonance harmonic layer for the lowest emission frequency. This is supported by the observation of elliptically polarised emission from UV Ceti by Lynch et al. (2017) at 154 MHz, which corresponds to a dipolar magnetospheric altitude of $\sim 6.2\,R_*$. If the inferred cavity does extend to the third, or possibly even the second gyroresonance harmonic layer (where $B = B_{\rm src}/2$, which strongly absorbs emission in the fundamental mode), then the extremely low densities should result in an optical depth sufficiently small for the emission to escape.

Earth's auroral kilometric radiation (AKR) has been observed to escape the plasma via multiple reflections from within the auroral density cavities, to a height where the ambient x-mode cutoff frequency is equal to the emission frequency (e.g. Zarka, 1998; Ergun et al., 2000). The extremely low-density cavity inferred by the presence of linear polarisation should be surrounded by the high-density plasma of the stellar corona, suggesting that ECMI emission observed here may also escape the stellar magnetosphere through a similar process. These reflections would be likely to modify the intrinsically elliptically polarised emission via mode-coupling, potentially removing any linearly polarised component of the emission. A possible solution is to require that the cavity has a sufficiently large volume so that radiation can escape without reflecting off the cavity walls. Another solution may be that the elliptical polarisation is generated by partial conversion of x-mode into o-mode after reflections on the cavity wall (Zarka, 1998), removing any strong requirements on the minimum size of the cavity. We note that elliptically polarised emission has also been observed from AD Leo (Spangler et al., 1974), suggesting that the auroral processes generating these magnetospheric cavities may also occur in other active M-dwarfs.

Finally, assuming intrinsically elliptically polarised emission, we can use the observed elliptical polarisation to determine the emission angle of the ECMI emission relative to the local magnetic field. Melrose & Dulk (1993) gave a simple relation between the ECMI emission angle relative to the magnetic field, θ, and the axial ratio of elliptically polarised emission, T (not to be confused with temperature, or brightness temperature T_b), to first order:

$$T \approx \cos(\theta). \tag{3.10}$$

Using the expression for the axial ratio from Dulk et al. (1994),

$$T = \tan\left(\frac{1}{2}\arcsin\left(\frac{V}{I_p}\right)\right), \tag{3.11}$$

where $I_p = \sqrt{Q^2 + U^2 + V^2}$, we can derive the angle of ECMI emission for our 2019-03-07 observation, where full polarisation calibration was possible. For pulses 19-1B and 19-2C, which are detected significantly in linear polarisation, we derive an ECMI emission angles of $60 \pm 4°$ and $58 \pm 5°$ to the magnetic field respectively.

3.5.4 Transition from solar-type to auroral activity

The multi-wavelength flare activity of UV Ceti (along with other active M-dwarfs) has been largely interpreted within the framework of solar flares. For example, the observations of UV Ceti performed by Benz et al. (1996), described in Section 3.2, confirmed the operation of the Neupert effect on active M-dwarfs. The Neupert effect is believed to be driven by the process of chromospheric evaporation, where accelerated non-thermal electrons stream downwards along magnetic loops, impacting and heating the chromospheric plasma, which then 'evaporates' and rises to the upper corona. Chromospheric evaporation has been observed in other active M-dwarfs (e.g. Güdel et al., 2002a), suggesting that Solar-like magnetospheric processes may be prevalent among active M-dwarfs, although several counter-examples exist (e.g. Osten et al., 2005; Lim et al., 1996).

Another paradigm of magnetospheric activity that may be relevant to active M-dwarfs is auroral-type magnetic activity. Auroral processes, revealed by periodic, highly polarised radio pulses, are known to occur on magnetised planets (Zarka, 1998), brown dwarfs (Hallinan et al., 2007; Pineda et al., 2017), and magnetic chemically peculiar stars (Trigilio et al., 2000). Auroral processes are driven by large, powerful field-aligned current systems occurring in stellar and sub-stellar magnetospheres (Treumann, 2006; Zarka, 1998). Our detection of periodic, elliptically polarised pulses from UV Ceti, confirming suggestions by Lynch et al. (2017) and Villadsen & Hallinan (2019), shows that this type of magnetic activity also applies to active M-dwarfs. This shows that auroral emitters extend further up along the main sequence than previously realised.

Our detection of elliptically polarised emission from UV Ceti (and previously by Lynch et al. 2017) implies that extreme density cavities exist within the magnetosphere of UV Ceti (see Section 3.5.3). This shows that the auroral processes operating in the magnetosphere of UV Ceti are closely analogous to those occurring in the magnetospheres of Jupiter and Saturn, where elliptically polarised emission from extremely low densities is also observed (Melrose & Dulk, 1991; Dulk et al., 1994; Boudjada & Lecacheux, 1991; Fischer et al., 2009). Elliptically polarised emission was also detected from AD Leo by Spangler et al. (1974), which, like UV Ceti, hosts a large-scale, axisymmetric magnetic field (Kochukhov & Lavail, 2017; Morin et al., 2008), hinting that auroral-type magnetic activity may apply to other active M-dwarfs with large, axisymmetric magnetic fields. We note, however, that no other M-dwarf has shown evidence of periodic radio emission (Villadsen & Hallinan, 2019). This indicates that such behaviour may only be intermittent, or it could also be due to incomplete observational coverage of the rotational periods of these stars (e.g. AD Leo has rotational period of 2.2399 ± 0.0006 d; Morin et al., 2008).

Together, the observation of both Solar-like (Guedel et al., 1996) and auroral activity in UV Ceti, and potentially other active M-dwarfs (Spangler et al., 1974), suggests that these active stars may mark the beginning of the transition from Solar-like activity to auroral activity that becomes prevalent in substellar objects (Pineda et al., 2017; Zarka, 1998). Further detailed studies of coherent bursts from active M-dwarfs across a range of spectral types and magnetospheric geometries, along with simultaneous multi-wavelength information may assist in clarifying the stellar parameters and magnetospheric conditions which drive this transition.

3.6 Summary & conclusions

We report the detection of several coherent, highly polarised pulses from the active M-dwarf UV Ceti. The pulses are periodic in nature, with a period of 5.447 ± 0.008 h – consistent with the measured rotational period of UV Ceti (Barnes et al., 2017). The brightness temperature, polarisation, and time-frequency structure of the pulses are consistent with highly-beamed ECMI emission originating along magnetic loops, which cross the line of sight every rotation of the star. Some of the pulses show elliptical polarisation – a rare occurrence in nature, which implies very low plasma densities ($\lesssim 41\,\mathrm{cm}^{-3}$) around the source region. This can be explained if the emission originates from an extreme density cavity in the magnetosphere of UV Ceti, analogous to the terrestrial auroral cavities (Zarka, 1998; Ergun et al., 2000). We suggest that the density cavity is key to the escape of the radiation at the first and second harmonic of the cyclotron frequency, by a reduced optical depth at the gyroresonance harmonic layers, and/or by multiple reflections along the cavity wall. The presence of periodic and elliptically polarised radio emission from UV Ceti shows that auroral-type magnetic activity can also manifest in active M-dwarfs, along with Solar-like activity as indicated by the presence of the Neupert effect (Guedel et al., 1996). This indicates that M-dwarfs may mark the beginning of the transition from Solar-like activity to auroral activity which becomes prevalent in brown dwarfs and magnetised planets (Pineda et al., 2017; Zarka, 1998).

We have demonstrated the capabilities of ASKAP for studying polarised variable radio sources. We note that our best RMS noise in our 4 MHz, 10 s dynamic spectrum bins is ~ 7 mJy. This RMS noise value is competitive with the RMS noise for dynamic spectra taken with the Karl G. Jansky Very Large Array (1-7 mJy) reported by Villadsen & Hallinan (2019), with similar spectral and temporal resolution.

The quality of the dynamic spectra, and the wide field of view of ASKAP presents a strong opportunity for future large-scale surveys for coherent bursts from stellar and sub-stellar objects, along with detailed, targeted studies as presented in this work. Villadsen & Hallinan (2019) estimated that the active M-dwarf transient density should be one per 10 deg^2, meaning ASKAP surveys such as VAST (Murphy et al., 2013) will probe the population of coherent bursts from M-dwarfs, giving a more complete insight into the processes operating in the magnetospheres of these stars.

Acknowledgements

We thank Donald Melrose, Mohammad Rafat, Michael Wheatland and George Heald for useful discussions and suggestions which strengthened this work. TM acknowledges the support of the Australian Research Council through grant FT150100099. AZ acknowledges support from an Australian Government Research Training Program (RTP) Scholarship. DK was supported by NSF grant AST-1816492. The Australian SKA Pathfinder is part of the Australia Telescope National Facility which is managed by CSIRO. Operation of ASKAP is funded by the Australian Government with support from the National Collaborative Research Infrastructure Strategy. ASKAP uses the resources of the Pawsey Supercomputing Centre. Establishment of ASKAP, the Murchison Radio-astronomy Observatory and the Pawsey Supercomputing Centre are initiatives of the Australian Government, with support from the Government of Western Australia and the Science and Industry Endowment Fund. We acknowledge the Wajarri Yamatji people as the traditional owners of the Observatory site. Parts of this research were supported by the Australian Research Council Centre of Excellence for All Sky Astrophysics in 3 Dimensions (ASTRO 3D), through project number CE170100013. This research made use of the following PYTHON software packages: APLPY[2], an open-source plotting package for PYTHON (Robitaille & Bressert, 2012); MATPLOTLIB[3] (Hunter, 2007); NUMPY[4] (van der Walt et al., 2011); and ASTROPY[5], a community-developed core PYTHON package for Astronomy (Astropy Collaboration et al., 2013, 2018).

[2] http://aplpy.github.io/
[3] https://matplotlib.org/
[4] https://www.numpy.org/
[5] http://www.astropy.org

Chapter 4

A Flare–Type IV Burst Event From Proxima Centauri and Implications for Space Weather

ANDREW ZIC,[1,2] TARA MURPHY,[1,3] CHRISTENE LYNCH,[4,5] GEORGE HEALD,[6] EMIL LENC,[2] DAVID L. KAPLAN,[7] IVER H. CAIRNS,[8] DAVID COWARD,[9] BRUCE GENDRE,[9] HELEN JOHNSTON,[1] MEREDITH MACGREGOR,[10] DANNY C. PRICE,[11,12] MICHAEL S. WHEATLAND[1]

[1]Sydney Institute for Astronomy, School of Physics, University of Sydney, NSW 2006, Australia
[2]CSIRO Astronomy and Space Science, PO Box 76, Epping, NSW 1710, Australia
[3]ARC Centre of Excellence for Gravitational Wave Discovery (OzGrav), Hawthorn 3122, VIC, Australia
[4]International Centre for Radio Astronomy Research (ICRAR), Curtin University, Bentley, WA, Australia
[5]ARC Centre of Excellence for All Sky Astrophysics in 3 Dimensions (ASTRO3D), Bentley, WA, Australia
[6]CSIRO Astronomy and Space Science, PO Box 1130, Bentley, WA 6102, Australia
[7]Department of Physics, University of Wisconsin - Milwaukee, Milwaukee, Wisconsin 53201, USA
[8]School of Physics, University of Sydney, NSW 2006, Australia
[9]OzGrav-UWA, University of Western Australia, Department of Physics, M013, 35 Stirling Highway, Crawley, WA 6009, Australia
[10]Department of Astrophysical and Planetary Sciences, University of Colorado, 2000 Colorado Avenue, Boulder, CO 80309, USA
[11]Department of Astronomy, University of California Berkeley, Berkeley CA 94720
[12]Centre for Astrophysics & Supercomputing, Swinburne University of Technology, Hawthorn, VIC 3122, Australia

This Chapter was published as Zic et al. (2020), ApJ, 905, 23. My contributions include planning the observing campaign, carrying out observations and reducing data from the ANU 2.3-m Telescope, reducing data from the Zadko 1-m Telescope, writing the majority of the text, production of all figures and tables, and data analysis and interpretation. Emil Lenc reduced the ASKAP observations, and contributed to the description of ASKAP data reduction. David Coward and Bruce Gendre organised and carried out observations with the Zadko 1-m Telescope, and Bruce Gendre contributed to the description of Zadko 1-m Telescope observations.

4.1 Abstract

Studies of solar radio bursts play an important role in understanding the dynamics and acceleration processes behind solar space weather events, and the influence of solar magnetic activity on solar system planets. Similar low-frequency bursts detected from active M-dwarfs are expected to probe their space weather environments and therefore the habitability of their planetary companions. Active M-dwarfs produce frequent, powerful flares which, along with radio emission, reveal conditions within their atmospheres. However, to date, only one candidate solar-like coherent

radio burst has been identified from these stars, preventing robust observational constraints on their space weather environment. During simultaneous optical and radio monitoring of the nearby dM5.5e star Proxima Centauri, we detected a bright, long-duration optical flare, accompanied by a series of intense, coherent radio bursts. These detections include the first example of an interferometrically detected coherent stellar radio burst temporally coincident with a flare, strongly indicating a causal relationship between these transient events. The polarisation and temporal structure of the trailing long-duration burst enable us to identify it as a type IV burst. This represents the most compelling detection of a solar-like radio burst from another star to date. Solar type IV bursts are strongly associated with space weather events such as coronal mass ejections and solar energetic particle events, suggesting that stellar type IV bursts may be used as a tracer of stellar coronal mass ejections. We discuss the implications of this event for the occurrence of coronal mass ejections from Proxima Cen and other active M-dwarfs.

4.2 Introduction

M-dwarfs are the most populous type of star in the Galaxy (Henry et al., 2006) and have a high rate of close-in terrestrial exoplanets, ~ 1.2 per star (Hardegree-Ullman et al., 2019). Active M-dwarfs frequently produce flares several orders of magnitude more energetic than solar flares (Lacy et al., 1976). Associated increases in ionising radiation, along with frequent impacts of space weather events, such as coronal mass ejections (CMEs), are expected to result in magnetospheric compression and atmospheric erosion of close-in planetary companions, threatening their habitability (Khodachenko et al., 2007; Lammer et al., 2007). While the radiative components of M-dwarf flares are routinely detected and characterised across all wavelengths, their phenomenology arises from processes confined to the stellar atmosphere. As a result, the space weather environment around these stars cannot be assessed from flare observations alone. Nonetheless, there have been promising developments in observational signatures of stellar CMEs in recent years. For example, Argiroffi et al. (2019) reported the first confirmed stellar CME, detected via X-ray spectroscopy of a flare on the giant star HR 9024. Candidate CME events from active M-dwarfs have been inferred through signatures such as prolonged X-ray absorption (Moschou et al., 2019, 2017), and blue-shifted Balmer line components (Vida et al., 2019a; Leitzinger et al., 2011; Houdebine et al., 1990). However, these may be solely flare-related phenomena, such as chromospheric evaporation or as a result of limited diagnostic ability of low-resolution X-ray spectroscopy (Argiroffi et al., 2019; Osten & Wolk, 2017).

Another promising route toward characterising space weather around active M-dwarfs is the detection of solar-like type II, III, and IV bursts (Wild & McCready, 1950; Boischot, 1957; White, 2007; Osten & Wolk, 2017; Vedantham, 2020). These low-frequency radio bursts ($\lesssim 1\,\mathrm{GHz}$) trace distinct particle acceleration processes within and beyond the corona that contribute to space weather, and are classified according to their morphologies in dynamic spectra (e.g. Wild et al., 1963; White, 2007).

4.2.1 Characteristics of Space Weather-Related Radio Bursts

Solar type II, type III, and type IV bursts have the following characteristics and interpretations: type II bursts last several minutes up to a few hours, exhibiting a relatively slow drift from high to low frequencies. They are produced by CME shock fronts or flare blast waves propagating outward through the corona – see Cairns et al. (2003) and Cairns (2011) for a review of type II bursts in the context of solar system shocks. There have been several efforts toward detecting stellar type II bursts, with no positive detections (Crosley et al., 2016; Crosley & Osten, 2018b,a; Villadsen & Hallinan, 2019). Type III bursts are short-lived (0.1–10 s), rapidly drifting bursts driven by relativistic electron beams escaping from the corona along open magnetic field lines – see (Reid & Ratcliffe, 2014) for a review. Type IV bursts are long-duration bursts that occur during and after the decay phase of large flares (Takakura, 1963), and are thought to be driven by continuous injection of energetic electrons into post-flare magnetic structures following CMEs (Cliver et al., 2011; Salas-Matamoros & Klein, 2020). We do not expand upon solar type I and type V bursts here as they are not relevant to space weather studies (White, 2007), but refer the reader to texts such as Kundu (1965) and Wild et al. (1963) for overviews and detailed definitions of solar radio bursts and other emissions.

Type IV bursts are particularly important in solar space weather studies, because they are associated with space weather events such as CMEs and solar energetic particle (SEP) events, and because they indicate ongoing electron acceleration following large flares (e.g. Kahler & Hundhausen, 1992). For example, Robinson (1986) argued that CMEs are a *necessary* condition for the generation of type IV bursts, and Cane & Reames (1988a) also argued that type IV bursts occur with CMEs, which also explains their association with SEPs (Kahler, 1982). Cane & Reames (1988b) found that 88% of type IV bursts are associated with type II bursts, with almost all interplanetary type II bursts associated with CMEs (Cairns et al., 2003). In addition, solar type II and type IV bursts are strongly associated with Hα flares (Cane & Reames, 1988b). Type IV bursts show a wide range of features, and consist of several subclasses (Pick, 1986). Of particular interest here are the "decimetric type IV bursts" (type IVdm) (Benz & Tarnstrom, 1976), which have a frequency range spanning $\sim$ 200–2000 MHz (Cliver et al., 2011), covering the frequency range accessible with current low and mid-frequency radio facilities. These bursts have long delays ($>$ 30 minutes) from the microwave continuum emission peak, and are composed of several subcomponents lasting tens of minutes to several hours (Pick, 1986). The early component is often complex, showing a variety of frequency drifts (Takakura, 1967). In addition, they often exhibit high degrees of circular polarisation (up to 100%), fractional bandwidths $\Delta\nu/\nu \sim 0.1$–1 (Benz & Tarnstrom, 1976; Cliver et al., 2011), and intensities reaching up to 10^6 sfu (10^{10} Jy), making them among the most intense solar radio bursts recorded (Cliver et al., 2011). The associated brightness temperatures are very high (between 10^8 K and 10^{15} K), with brightness temperatures in excess of 10^{12} K requiring a coherent mechanism (Kellermann & Pauliny-Toth, 1969). At the lower range of brightness temperatures ($\lesssim 10^{11}$ K) additional properties such as narrow spectral features and high degrees of circular polarisation may indicate a coherent emission mechanism, though incoherent gyrosynchrotron emission is regularly invoked for bursts at this lower range of brightness temperatures lacking these indicators of coherence (Morosan et al., 2019). If the bursts exhibit a frequency drift, it is usually small (drift rates $|\dot{\nu}| \leq 100\,\mathrm{kHz\,s^{-1}}$), and may indicate a gradually-expanding source region with decreasing magnetic field strength and/or plasma density (Takakura, 1963).

4.2.2 Stellar Radio Bursts in the Solar Paradigm

The detection of solar-like radio bursts holds great potential for understanding coronal particle acceleration processes in M-dwarf flares, and for diagnosing the space weather environment around these stars. For example, solar type IV bursts are associated with space weather events such as CMEs and SEP events (Robinson, 1986; Cane & Reames, 1988b; Salas-Matamoros & Klein, 2020), and probe ongoing electron acceleration in magnetic structures following large flares (Salas-Matamoros & Klein, 2020; Cliver et al., 2011; Wild et al., 1963).

However, there have been few unambiguous identifications of solar-like low-frequency bursts from M-dwarfs or other stellar systems to date. Kahler et al. (1982) detected a strong radio burst from the dM4.0e star YZ Canis Minoris in time-series data with the Jodrell Bank interferometer at 408 MHz, beginning ~ 17 minutes after flaring activity in optical and X-ray wave bands. Owing to the delayed onset of the burst, Kahler et al. (1982) identified this radio event as a type IV burst. Other early low-frequency detections were made with time-series data from single-dish telescopes, making them susceptible to terrestrial interference (Bastian, 1990; Bastian et al., 1990). For example, Spangler & Moffett (1976) and Lovell (1969) detected several M-dwarf radio bursts with intensities ranging from hundreds of millijansky to several jansky, coincident with optical flaring activity. However, low-frequency interferometric observations of active M-dwarfs have struggled to detect bursts of similar intensities or at similar rates as recorded in early single-dish observations (Villadsen & Hallinan, 2019; Lynch et al., 2017; Davis et al., 1978), casting doubt on the reliability of these early detections. A recent exception to this trend of faint, low-duty cycle bursts at low radio frequencies is the detection of a 5.9 Jy burst from dM4e star AD Leonis at 73.5 MHz reported by Davis et al. (2020). Although the signal-to-noise ratio of this detection is fairly low, future interferometric detections at these very low frequencies (< 100 MHz) may provide some validation for early single-dish detections.

Coherent radio bursts from M-dwarfs detected with modern interferometric facilities have shown properties at odds with solar observations. Foremost, the majority of observations show poor association between radio bursts and multiwavelength flaring activity (Crosley & Osten, 2018b; Bastian, 1990; Kundu et al., 1988; Haisch et al., 1981), with the exception of the results from Kahler et al. (1982) described above. Another key contrast is that there have been no morphological classifications of solar-like radio bursts to date, although some stellar radio bursts have shown spectro-temporal features consistent with solar radio bursts — e.g., "sudden reductions"[1] or "quasi-periodic pulsations"[2] (Bastian et al., 1990). A final point of difference is that coherent radio bursts from M-dwarfs consistently exhibit high de-

[1]Abrupt decreases in burst intensity.

[2]Pulsations occurring at similar, but irregular time intervals.

grees of circular polarisation ($f_C \sim 50$–100%; (Villadsen & Hallinan, 2019)), whereas only some solar radio bursts, such as type I, type IV, and decimetric spike bursts, are highly polarised (Kai, 1962, 1965; Aschwanden, 1986) – other solar radio bursts exhibit only mild degrees of polarisation.

These differences have hampered efforts to understand M-dwarf radio activity based on our more complete understanding of the Sun (Villadsen & Hallinan, 2019). In addition, recent studies have shown that the low-frequency variability of active (Zic et al., 2019b) and inactive (Vedantham et al., 2020) M-dwarfs may arise from auroral processes in their magnetospheres. These phenomena are driven by ongoing field-aligned currents in the strong, large-scale magnetic field of the star, rather than flaring activity associated with localised active regions. This suggests that in general, the physical driver of many low-frequency radio bursts from M-dwarfs may be decoupled from the flares probed by optical and X-ray wave bands—in stark contrast to the Sun.

4.2.3 Outline of This Chapter

In this Chapter, we report the detection of several radio bursts from Proxima Centauri (hereafter Proxima Cen) associated with a large optical flare. In Section 4.3 we detail the multiwavelength observations and data reduction. In Section 4.4 we describe the detections of the flare and radio bursts. We discuss these detections in light of the solar paradigm, and possible implications for space weather around Proxima Cen. In Section 4.5 we summarise our findings.

4.3 Multiwavelength Observations and Data Reduction

To search for space weather signatures from an active M-dwarf, we observed Proxima Cen simultaneously at multiple wavelengths over 11 nights. This star is suitable for our study because it is close to the Sun (1.3 pc; Gaia Collaboration et al., 2018), is magnetically active, and hosts a terrestrial-size planet within its habitable zone (Anglada-Escudé et al., 2016), along with a recently discovered planet candidate at 1.5 AU (Damasso et al., 2020). Proxima Cen is also an interesting target because its slower rotation and slightly more mild activity levels (Kiraga & Stepien, 2007; Reiners & Basri, 2008b) differentiate it from more active and rapidly rotating M-dwarfs that have been previously targeted in search of space weather events (Crosley & Osten, 2018b,a; Crosley et al., 2016; Villadsen & Hallinan, 2019).

Before providing details on observations and data reduction for the facilities used in this work, we note that all local observatory times have been converted to the barycentric dynamical timeframe (TDB), to ensure consistency between ground- and space-based facilities.

4.3.1 Transiting Exoplanet Survey Satellite (TESS)

NASA's TESS (Ricker et al., 2015) observed Proxima Cen during the period of 2019 April–May in its Sector 11 observing run. Observations were taken through the broad red bandpass spanning 5813–11159 Å on the TESS instrument (the TESS band). We downloaded the calibrated TESS light-curves for Proxima Centauri from the Mikulski Archive for Space Telescopes[3]. Light-curves are available in a Simple Aperture Photometry (SAP) or Pre-search Data Conditioning Simple Aperture Photometry (PDCSAP) formats. Because PDCSAP light-curves are optimised to detect transit and eclipse signals, and remove other low-level variability that may be astrophysical in origin, we opted instead to use the SAP light-curve. We normalised the SAP light-curve by dividing by the median value long after the flare decay (MBJD 58605.6–58605.7).

4.3.2 Zadko Telescope

The Zadko Telescope (Coward et al., 2017) is a 1 m f/4 Cassegrain telescope situated in Western Australia. For this campaign, its main instrument, an Andor IkonL camera, was replaced by a MicroLine ML50100 camera from Finger Lakes Instrumentation. The new camera allowed for a faster readout and thus a better temporal resolution of the light-curve. The CCD is 8k×6k, but we used it with a binning of 2×2 to increase the signal-to-noise ratio, giving a pixel scale of $1.39''$ pixel^{-1}.

We used the Sloan g' filter (spanning 3885–5640Å) for the observations, which started as soon as possible after dusk, and lasted until Proxima Cen was too low on the horizon to safely operate the telescope. Each image was taken with a 10,s exposure, and needed 13.32 s for the readout and preparation of the next exposure. Thus, our observation cadence for that night was about 23.3 s. We took 20 bias and dark frames prior to the beginning of observations for calibration. During the observation night the conditions were good, with no visible clouds on the images. The stable temperature and calm wind allowed for fair observations.

We applied standard photometric data reduction procedures using `ccdproc` (Craig et al., 2015). Twenty 10 ,s dark exposures were bias corrected and median combined to remove effects of cosmic rays in the calibration frame. Bias and dark correction were applied to 180 s flat-field exposures taken several nights after the observing campaign, and these flat-field frames were median combined. Raw target exposures were dark and bias corrected, and the corrected flat-field image was used to correct for spatial variations in the CCD sensitivity. Images were aligned using `astroalign` (Beroiz et al., 2020) to correct for slight drifts in the telescope pointing throughout the night. We used SExtractor (Bertin & Arnouts, 1996) to perform aperture photometry on Proxima Cen and nearby reference stars using a 12 pixel diameter ($16.7''$) aperture. We corrected the raw Proxima Cen light-curve for systematic variations in flux over the course of the night by median normalising the raw light-curves of nearby neighbouring stars around Proxima Cen, with similar colours (Gaia $B_p - R_p > 2$; $B_p - R_p = 3.796$ for Proxima Cen). We median combined these normalised light-curves to produce a systematic reference light-curve, and divided

[3] https://archive.stsci.edu/

the Proxima Cen light-curve by the systematic trend to produce a corrected light-curve. Finally, we divided the Proxima Cen light-curve by its median post-flare (MBJD 58605.6–58605.7) value to produce a light-curve in relative intensity.

4.3.3 ANU 2.3m Telescope

We performed time-resolved spectroscopy with the Wide-Field Spectrograph (WiFeS) on board the ANU 2.3m Telescope at Siding Spring Observatory (Dopita et al., 2007). WiFeS is an integral-field spectrograph that uses an image slicer with 25 $1'' \times 38''$ slitlets, resulting in a field of view of $25'' \times 38''$. Conditions at the observatory on 2019 May 02 were poor, resulting in high levels of cloud absorption and intermittent observational coverage during rainy periods. Seeing varied between $1.3''$ and $2.0''$. We took spectra with the U7000 and R7000 gratings in the blue and red arms of the instrument, respectively, using the RT480 dichroic. We took 90 s exposures of Proxima Cen using half-frame exposures, which resulted in a faster readout time of ∼30 s, and resulted in a reduced field of view of $12.5'' \times 38''$. The corresponding wavelength ranges after calibration were 3500 Å-4355 Å and 5400 Å-7000 Å, at a resolution of $R \sim 7000$.

For the calibration, we took bias, internal flat field (with a Quartz-Iodine lamp), wire, and arc frames (with a neon-argon lamp), using 5×5 s exposures for the red arm and 5×90 s exposures for the blue arm where appropriate. We took 3×90 s exposures of the standard star LTT4364 to calibrate for the bandpass response across wavelength for each grating.

We used the PyWiFeS pipeline (Childress et al., 2014) to derive and apply calibrations to each exposure. To summarise the PyWiFeS calibration process, we performed overscan subtraction, bad pixel repair and cosmic ray rejection, and co-addition of bias frames, which we then subtracted from science frames. We co-added the internal flat-field frames, and derived wavelength and spatial (y-axis) zero-point solutions using the arc and wire frames respectively. To derive the spectral flat-field response, we used the wavelength solution and the co-added flat-field frames, and applied the derived flat-field correction to each sky exposure. To derive the bandpass sensitivity response and flux scale, we extracted the spectrum of the standard star LTT4364 from a rectified (x, y, λ) grid, and determined the corrections by comparing the extracted spectrum to a spectro-photometrically calibrated reference spectrum. We applied the flux and bandpass corrections to each of the corrected Proxima Cen data cubes, before converting the telescope-frame (x, y, λ) cubes to the sky frame (α, δ, λ), where α, δ denote J2000 R.A. and decl., respectively. To preserve the temporal resolution of our observation, we did not co-add any of the Proxima Cen exposures during the data reduction process. We extracted sky-subtracted spectra from the final calibrated spectral cubes using a custom script adapted from the internal PyWiFeS code.

Due to cloudy conditions, accurately determining the continuum and line fluxes was not possible. We divided each exposure with the R7000 grating by the median value between 6000 and 6030 Å, selected because it was free of any prominent emission or absorption features that may vary significantly with flaring activity. Prominent [OI] sky lines could not be readily subtracted due to the cloudy conditions. Similarly, we divided each exposure with the U7000 grating by the median value between 4150 and 4300 Å. However, significantly higher cloud absorption in the 3500–4355 ÅU7000 band, and the intrinsically lower flux of Proxima Cen in this band means that the continuum estimates are even more uncertain than the R7000 band.

We used the `specutils` package[4] to measure line equivalent widths in the extracted calibrated spectra.

4.3.4 Australian Square Kilometre Array Pathfinder (ASKAP)

We observed Proxima Cen with ASKAP (McConnell et al., 2016) on 2019 May 02 09:00 UTC (scheduling block 8612) for 14 hours with 34 antennas, a central frequency of 888 MHz with 288 MHz bandwidth, 1 MHz channels, and 10 s integrations. We observed the primary calibrator PKS B1934−638 for 30 minutes (scheduling block 8614) immediately following the Proxima Cen observation. To calibrate the frequency-dependent XY-phase, an external noise source (the "on-dish calibrator" system) is employed on each of the ASKAP antennas. This system measures the XY phase of each dual-polarisation pair of phased-array feed beams, and adjusts the phase of the Y-polarisation beamformer weights so that the XY phase approaches zero. Further details of the ASKAP on-dish calibration system are provided in Chippendale & Anderson (2019) and Hotan et al. (submitted).

We reduced the data using the Common Astronomy Software Applications (CASA) package version 5.3.0-143 (McMullin et al., 2007). We used PKS B1934−638 to calibrate the flux scale, the instrumental bandpass, and polarisation leakage. We performed basic flagging to remove radio-frequency interference that affected approximately 20% of the data, primarily from known mobile phone bands.

We used a mask excluding a $4'$ square region centered on Proxima Cen to allow modelling of the field sources without removing the time- and frequency-dependent effects of Proxima Cen. The large exclusion window around the target also ensured that the flux density present in strong point-spread function (PSF) sidelobes during burst events were not modelled as point sources and removed during deconvolution, ensuring that its total flux density was preserved. We used the task TCLEAN to perform deconvolution with a Briggs weighting and a robustness of 0.0. We used the MTMFS algorithm (with scales of 0, 5, 15, 50, and 150 pixels and a cell size of $2.5''$) to account for complex field sources, and used two Taylor terms to model sources with non-flat spectra. We imaged a 6000×6000 pixel field ($250' \times 250'$) to include the full primary beam and first null, and deconvolved to a residual of $\sim$3 mJy beam^{-1} to minimise PSF side-lobe confusion at the location of Proxima Cen. We subtracted the field model from the visibilities with the task UVSUB, and vector-averaged all baselines greater than 200 m to generate the dynamic spectra for each of the instrumental polarisations. We show a deconvolved image of the full $250'$ field over the 14 ,hr ASKAP observation in Figure 4.1.

We formed dynamic spectra for the four Stokes parameters (I, Q, U, V) following Zic et al. (2019b), such that they were consistent with the IAU convention of polar-

[4] https://specutils.readthedocs.io/

isation. To improve the signal-to-noise ratio in the dynamic spectra, we averaged the Stokes I and V products by a factor of 3 in frequency to produce final dynamic spectra with a resolution of 3 MHz in frequency and 10 s in time. Similarly, we averaged the Stokes Q and U dynamic spectra by a factor of 6 in frequency, giving these products a resolution of 6 MHz in frequency and 10 s in time. We produced radio light-curves by averaging the dynamic spectra across frequency. The rms sensitivity of our dynamic spectra is 12 mJy for Stokes I, and 11 mJy for Stokes Q, U, and V, calculated by taking the standard deviation of the imaginary component of the dynamic spectra visibilities. In a similar way, we calculated the rms sensitivity of the light-curves, finding 1.4 mJy for Stokes I, and 1.1 mJy for Stokes Q, U, and V.

4.4 Detection of Flare and Radio Burst Events

4.4.1 Photometric Flare Detection, Energy, and Temporal Modeling

We present the photometric light-curves in the bottom panel of Figure 4.2. These observations show the large, long-duration flare on MBJD 58605, which had a duration of approximately 1 hr.

We determined the radiated flare energy as follows. The flare energy $E_{f,p}$ through a photometric passband p is given by $E_{f,p} = \mathrm{ED} \times L_p$, where ED is the 'equivalent duration' of the flare, and L_p is the total quiescent luminosity of the star in passband p. The equivalent duration is given by

$$\mathrm{ED} = \int_{t_0}^{t_1} \left(\frac{I_f(t) - I_0}{I_0} \right) dt, \tag{4.1}$$

which we evaluate using Simpson's rule. Here, t_0 and t_1 are the start and end times of the flare, estimated by visual inspection of the light-curve, $I_f(t)$ is the intensity of the flare as a function of time, and I_0 is the median quiescent intensity. To compute the quiescent luminosity of the star, we obtained the flux-calibrated spectrum of Proxima Cen presented in Ribas et al. (2017), multiplying by $4\pi d^2$ to obtain the spectral luminosity L_λ. We estimate the total quiescent luminosity through passband p as $L_p \approx \langle L_{\lambda,p} \rangle \Delta\lambda_p$, where $\langle L_{\lambda,p} \rangle$ is the mean quiescent spectral luminosity in passband p, and $\Delta\lambda_p$ is the bandwidth of passband p. We evaluated the mean quiescent spectral luminosity using

$$\langle L_{\lambda,p} \rangle = \frac{\int_0^\infty L_\lambda T_p(\lambda) \lambda d\lambda}{\int_0^\infty T_p(\lambda) \lambda d\lambda}, \tag{4.2}$$

where $T_p(\lambda)$ is the filter transmission curve for passband p. This quantity is independent of any global scaling factors of the transmission curve, enabling a more reliable estimate of the total quiescent luminosity through passband p. To measure the the bandwidth $\Delta\lambda_p$, we computed the equivalent rectangular width,

$$W = \frac{\int_0^\infty T_p(\lambda) d\lambda}{\max(T_p(\lambda))}, \tag{4.3}$$

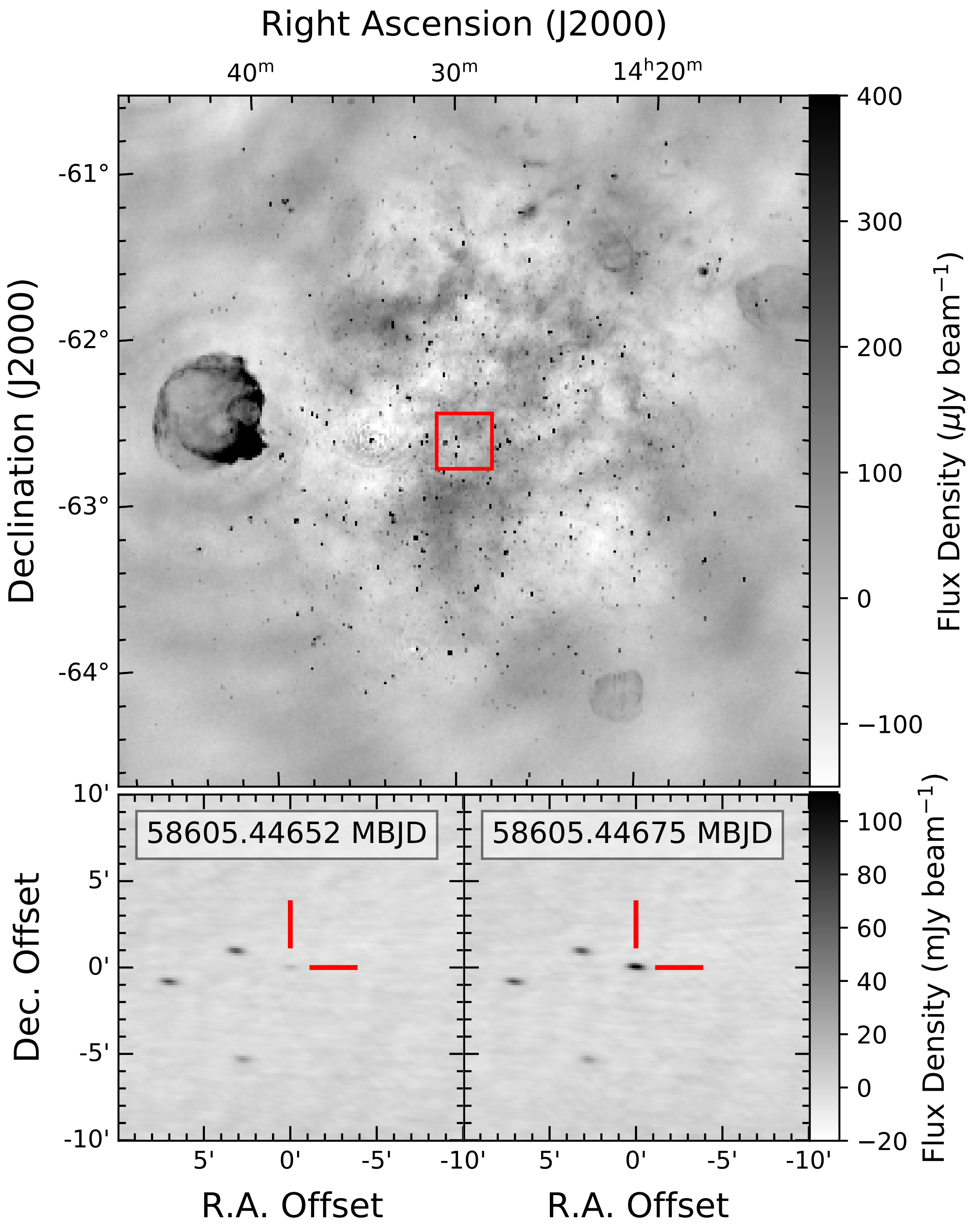

Figure 4.1: ASKAP Stokes I continuum images. Top panel: overview of the Proxima Cen field, imaged over the 14-hour observation. The grayscale intensity ranges from -150 to $400\,\mu$Jy beam^{-1}. This shows the presence of multiple strong point and extended sources, along with diffuse galactic emission. Bottom panel: 10 s deconvolved snapshot images of the local $20' \times 20'$ region around Proxima Cen, taken 20 s before (58605.44652 MBJD; left), and around the peak of AB1 (58605.44675 MBJD; right). The region shown in the snapshot images is indicated by the red square in the top sub-figure. The grayscale intensity ranges from -20 to $110\,$mJy beam^{-1} for the 10 s snapshot images.

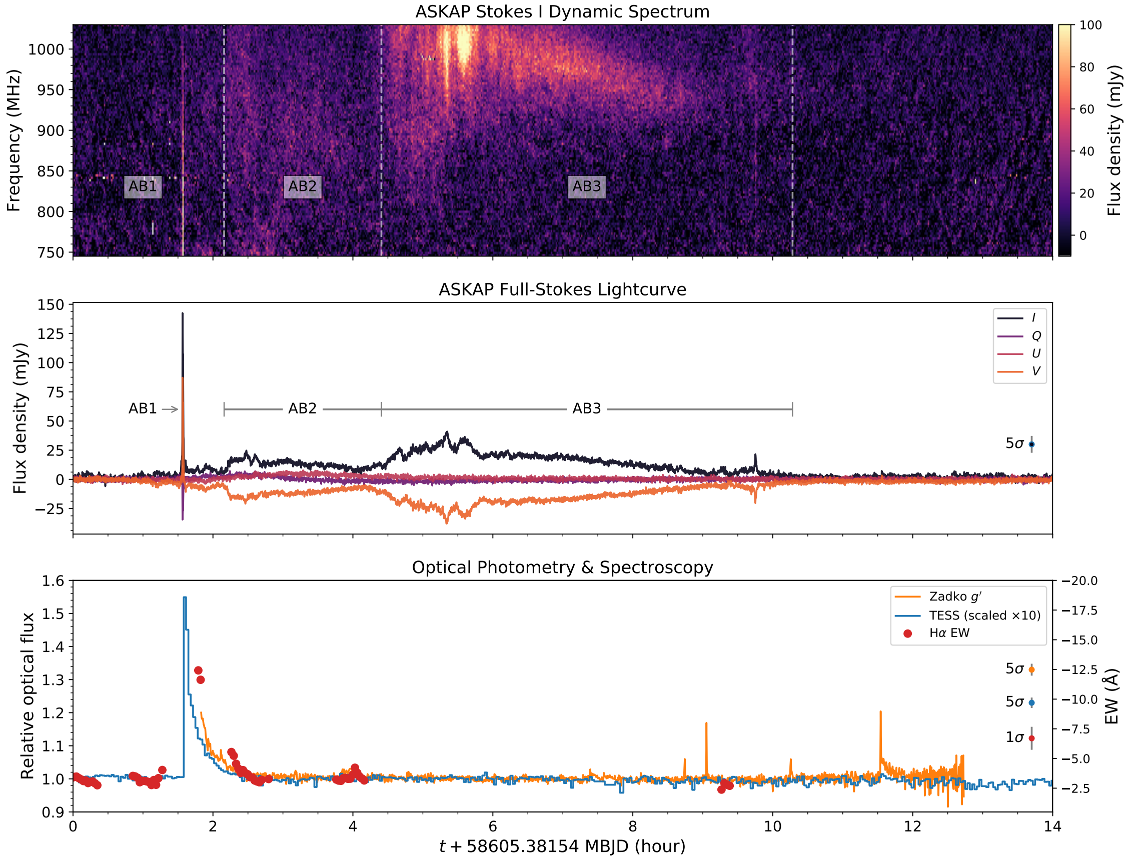

Figure 4.2: Multiwavelength overview of 2019 May 2 observations. Top panel: ASKAP Stokes I dynamic spectrum, showing intensity as a function of frequency and time. The resolution is 10 s in time and 3 MHz in frequency. The short timescale and broadband morphology of AB1, complex morphology of AB2, and long-duration, slow-drift morphology of AB3 are evident. Dashed vertical lines indicate the time intervals for AB2 and AB3. The burst labels AB1, AB2, and AB3 are indicated in the figure. Middle panel ASKAP light-curves in Stokes I, Q, U, and V, coloured in purple-black, dark purple, light purple, and orange, respectively. Burst labels are as in the top panel. Bottom panel: median-normalised photometric light-curves from TESS (blue curve) and the Zadko Telescope g' band (orange curve), both with values shown on the left abscissa, and Hα equivalent width from WiFeS on board the ANU 2.3m Telescope (red dots, values shown on right abscissa). Gaps in the equivalent width measurements are due to poor weather at the Siding Spring Observatory. For visual clarity, the TESS light-curve has been scaled by a factor of 10. Typical uncertainties are indicated in the figure on the right.

which is the width of a rectangle of height 1 and area equal to the total area beneath the filter transmission curve $T_p(\lambda)$. Applying these calculations to the TESS and Sloan g' passbands, we obtain quiescent luminosities of $1.1 \times 10^{30}\,\mathrm{erg\,s^{-1}}$ and $2.3 \times 10^{28}\,\mathrm{erg\,s^{-1}}$ respectively. TESS observations cover the full duration of the flare, albeit with relatively low temporal resolution (2 minute cadence), enabling us to compute a TESS-band flare equivalent duration of 31.2 ± 0.3 s, yielding a TESS-band flare energy $E_{f,\mathrm{TESS}} = 3.38 \pm 0.03 \times 10^{31}$ erg. To estimate the bolometric flare energy, we follow Osten & Wolk (2015) and adopt a 9000 K flare blackbody profile, and evaluate the fraction of energy radiated within the TESS and Sloan g' passbands, respectively, finding $E_{f,\mathrm{TESS}}/E_{\mathrm{bol}} = 0.21$ and $E_{f,g'}/E_{\mathrm{bol}} = 0.22$. Using the TESS observation, which covers the full duration of the flare, we calculate a bolometric flare energy of $1.64 \pm 0.01 \times 10^{32}$ erg. We note that the quoted uncertainties in this section are statistical only, and factors such as the light-curve normalisation, accurate determination of quiescent luminosity, and choice of flare blackbody temperature introduce systematic uncertainties, which we estimate contribute to errors on the order of 10% of the quoted values.

The 2 minute cadence of the TESS light-curve undersamples the impulsive rise phase of the flare. To obtain a more informed estimate of the flare onset time, we modelled the temporal morphology of the flare using the following piecewise model, adapted from the empirical flare template presented in Davenport et al. (2014):

$$\Delta I = \frac{I_f - I_0}{I_0} \tag{4.4}$$

$$= A \times \begin{cases} A_0^{(t-t_p)/(t_0-t_p)} & t < t_p \\ (1.0 - A_g)e^{(t-t_p)/\tau_i} & \\ +A_g e^{(t-t_p)/\tau_g} & t \geq t_p \end{cases}, \tag{4.5}$$

where A is the peak fractional amplitude above quiescence, t_p is a the time at flare peak relative to the ASKAP observation start time MBJD 58605.38154, A_0 is the relative pre-flare amplitude in the last TESS exposure at a set time MBJD $t_0 =$ 58605.44678 (93.94 minutes after the beginning of the ASKAP observation at MBJD 58604.38154), τ_i is the impulsive decay timescale, and A_g and τ_g are the gradual decay amplitude and timescales. We model the impulsive rise with an exponential rather than the quartic model of Davenport et al. (2014) to reduce the number of free parameters to determine from the low-resolution TESS light-curve. We used `emcee` to estimate the parameters and sample their posterior probability distributions, first evaluating each candidate model on a high-resolution time grid before resampling the candidate model onto the lower-resolution (2 minute cadence) TESS time series. We set uniform priors on each parameter, constraining $A_0 > 0$, $\tau_i, \tau_g < 0$, and $A > 0.03$. The resulting central parameter estimates and 64% confidence limits are as follows: $t_p = 96.61^{+0.23}_{-0.17}$ minutes, $A = 0.26^{+0.19}_{-0.08}$, $A_0 = 2.2^{+1.9}_{-1.3} \times 10^{-3}$, $A_g = 0.13^{+0.06}_{-0.05}$, $\tau_g = -12.6 \pm 0.2$ minutes, $\tau_i = -0.5 \pm 0.2$ minutes. The best-fitting model is shown in Figure 4.3, alongside the photometric light-curve from TESS and the radio light-curve from ASKAP.

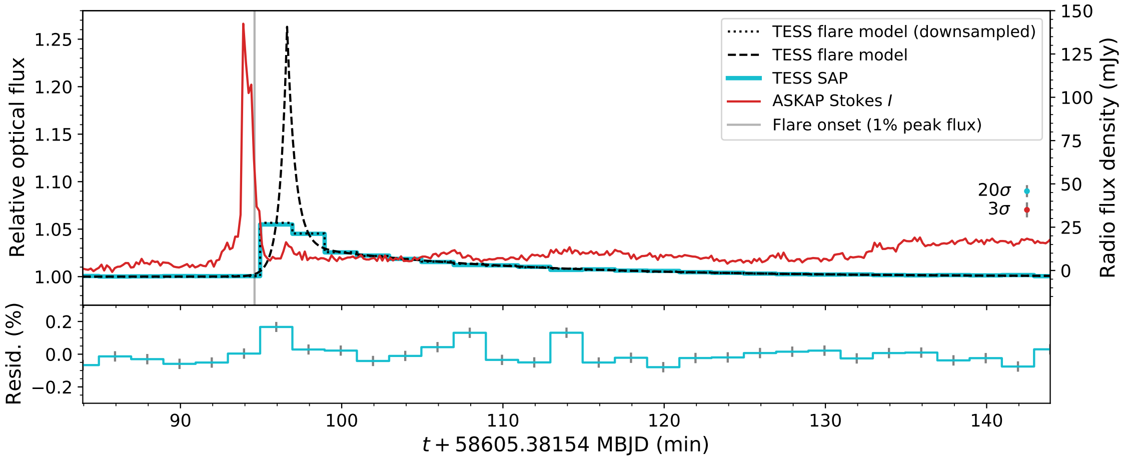

Figure 4.3: Top: relative timing of ASKAP Burst 1 (AB1), shown in red, and the main optical flare observed with TESS, shown in blue. The black dashed curve shows the best-fitting empirical model to the flare observed by TESS. The black dotted line shows the best-fitting model down-sampled onto the 2 minute resolution time series of the TESS observations. The vertical gray line shows the flare onset time, at which the intensity first reaches 1% of the flare peak. The right abscissa shows the ASKAP flux densities, and the left abscissa shows the relative flux from TESS-band photometry. Typical uncertainties are shown toward the figure right, upscaled for visual clarity. The radio peak and the estimated flare onset are separated by 42 s. Bottom: percentage residuals after subtracting the best-fitting flare model from the TESS light-curve. Error bars on the residuals are 1σ.

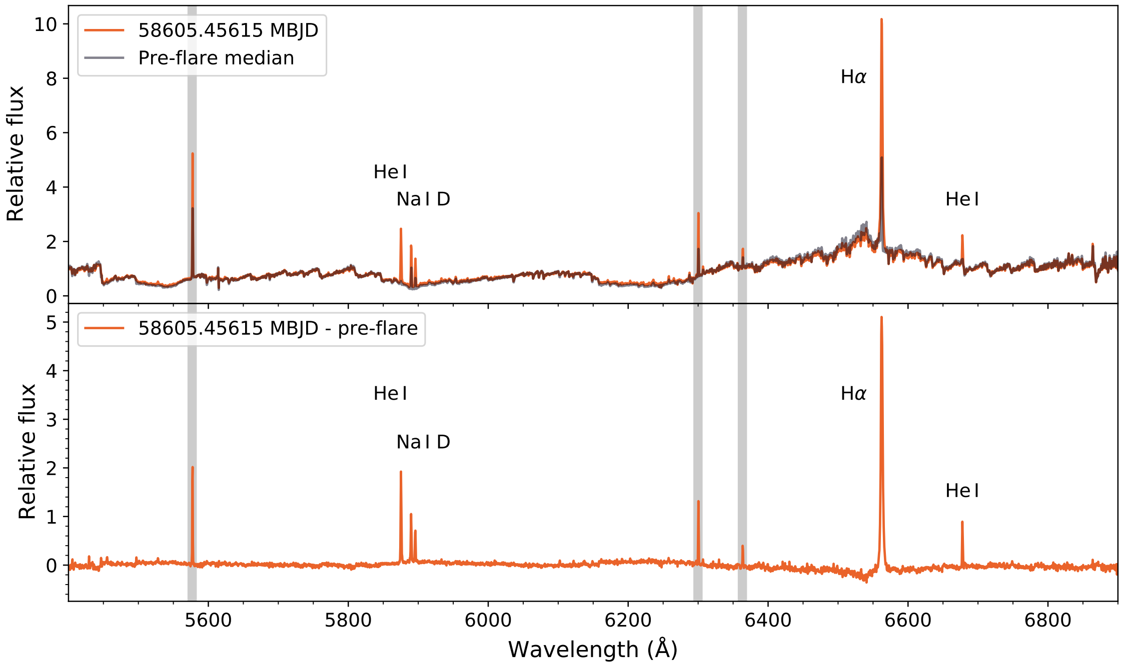

Figure 4.4: *Top*: WiFeS R7000 (λ5400–7000 Å) normalised spectra, showing a median of 10 exposures before the main flare (gray curve), and one 90 s exposure taken at MBJD 58605.45615 during the decay phase of the flare (orange curve). *Bottom*: quiescent-subtracted flare decay spectrum. Brightening of chromospheric emission lines, such as Hα, He I, and the Na I doublet (labelled in diagram) are clearly visible. Due to cloud cover, atmospheric [O I] lines at 5577, 6300, and 6363 Å , indicated in gray-shaded regions, could not be subtracted and should be ignored.

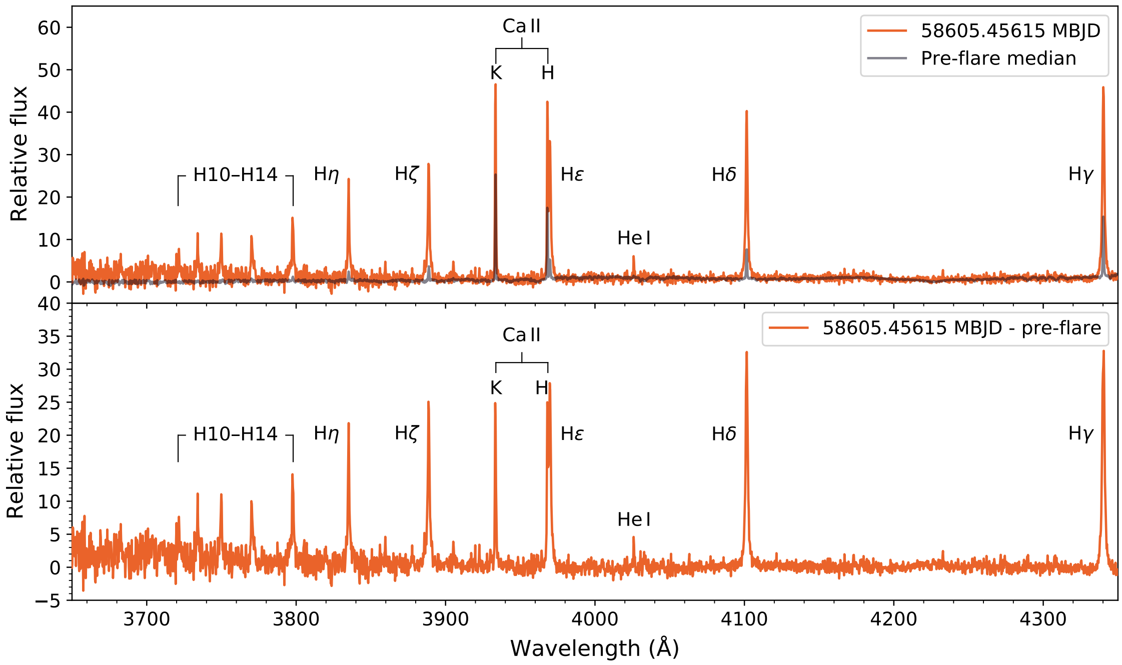

Figure 4.5: Same as Figure 4.4, but for the WiFeS B7000 (λ3500–4355 Å) spectra. Brightening and broadening of Balmer lines, from Hγ through to H14 are evident, along with an enhancement of the continuum toward the blue end of the spectrum.

4.4.2 WiFeS Time-Resolved Spectroscopy

Spectroscopic monitoring with the WiFeS on board the ANU 2.3m Telescope (Dopita et al., 2007) shows broadening and intensification of the Balmer lines, and the appearance of other chromospheric emission lines (e.g., He I $\lambda\lambda 4026, 5876, 6678$ Å) during this flare (Figures 4.4 and 4.5). This indicates substantial energy deposition by accelerated particles into the stellar chromosphere. Unfortunately, these observations were affected by poor weather, making it difficult to reliably detect variability in chromospheric emission line strength over the whole night. Along with the appearance of higher-order Balmer lines (up to H14 λ3721 Å), Figure 4.5 also shows a continuum enhancement toward the blue end of the spectrum. Figure 4.2 shows that the equivalent width of the Hα line is well correlated with the gradual decay of the flare continuum, consistent with previous observational results (e.g. Hawley & Pettersen, 1991).

4.4.3 Radio Bursts Detected with ASKAP

Observations with the ASKAP (McConnell et al., 2016)) centered at 888 MHz show three successive bursts, which we denote as ASKAP Bursts 1, 2, and 3 (AB1, AB2, and AB3 respectively). Figure 4.2 shows the total intensity (Stokes I) dynamic spectrum and full-Stokes light-curves in their multiwavelength context, and the full-Stokes dynamic spectra of the bursts are shown in Figures 4.6 and 4.7. Figure 4.1 shows two 10 s snapshot images, taken 20 s prior to (bottom left) and at the peak

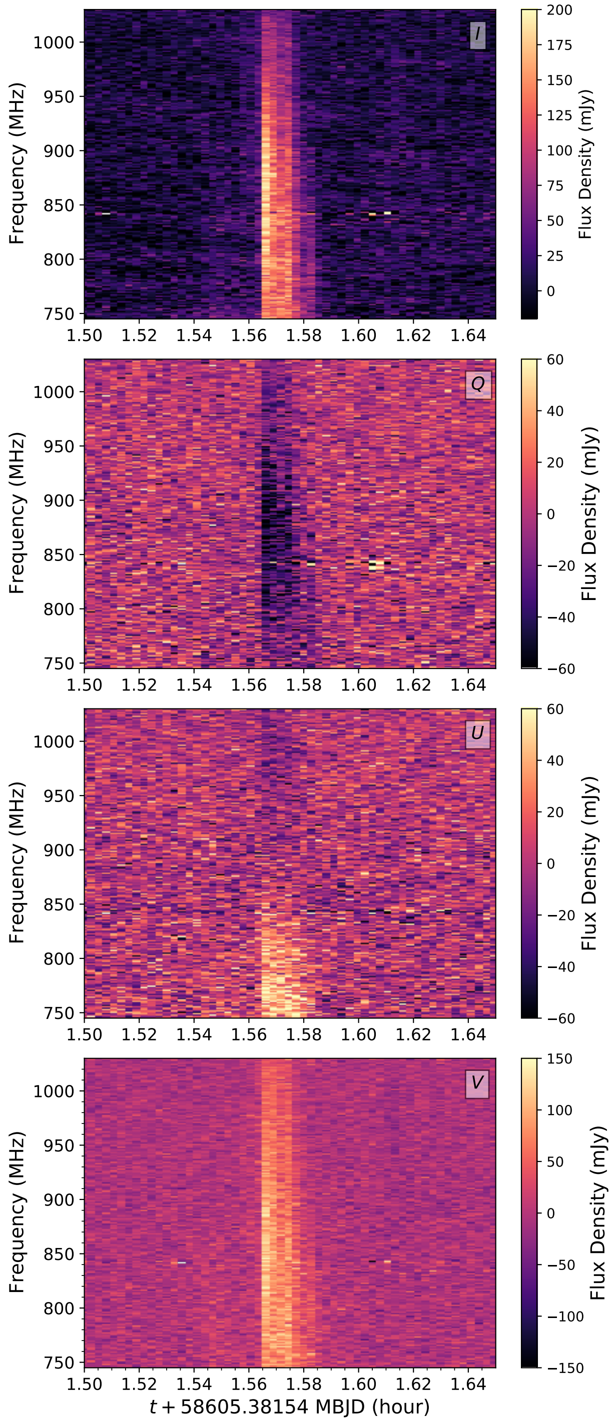

Figure 4.6: Dynamic spectrum of AB1 in Stokes I, Q, U and V (top to bottom), showing the rapid onset (rise time $\lesssim$ 10 s) linear polarisation, and downward-drifting upper envelope of AB1. The temporal and spectral resolution are 10 s and 1 MHz, respectively.

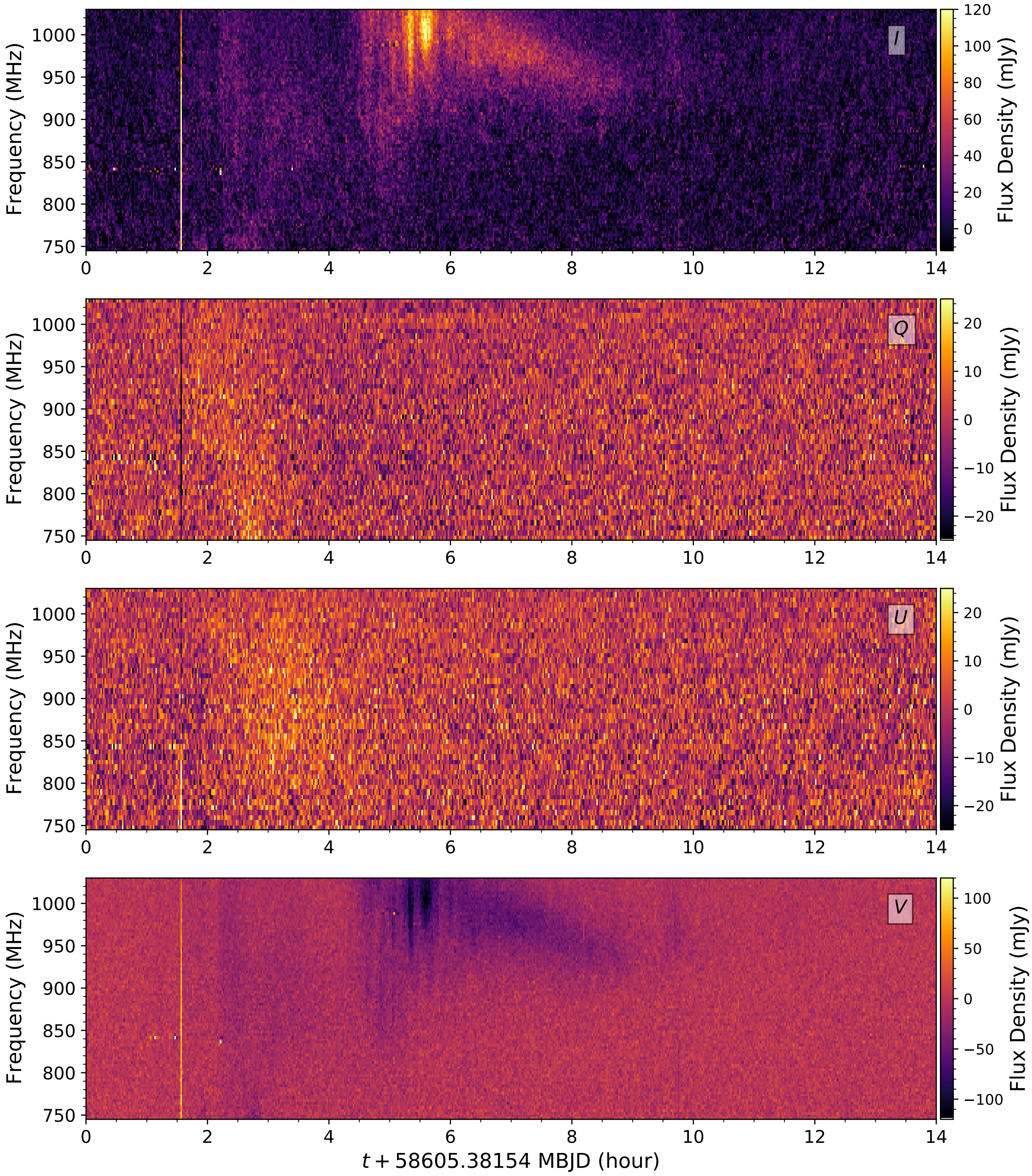

Figure 4.7: Full-Stokes ASKAP dynamic spectrum, showing intensity as a function of frequency and time for Stokes I, Q, U, and V from top to bottom. The high degree of circular polarisation for all bursts, and diffuse spectro-temporal structure of the linearly polarised component of AB2 are evident. The spectral resolution is 3 MHz for Stokes I and V, and 6 MHz for Stokes Q and U. The temporal resolution is 10 s for all Stokes parameters.

Label	t + MBJD 58605 (days)	Δt (mins)	$S_{\rm peak}$ (mJy)	$T_{b,\rm peak}{}^{a}$ ($\times 10^{11}$ K)	f_L (%)	f_C (%)	f_P (%)	$\dot{\nu}$ (MHz s^{-1})
AB1	0.4466	1.3	142.4 ± 1.4	2.93 ± 0.03	36.5 ± 1.1	-52.1 ± 1.3	57.1 ± 1.4	-4.70 ± 0.66
AB2	0.4715	119	24.7 ± 1.4	0.51 ± 0.02	43.3 ± 0.4	87.4 ± 0.8	98.5 ± 1.0	Complex^{b}
AB3	0.5652	354	41.0 ± 1.4	0.84 ± 0.02	$< 9^{c}$	91 ± 4	91 ± 4	$5.9 \pm 0.3 \times 10^{-3}$

Table 4.1: Properties of the radio bursts. Columns, from left to right: burst label, start time, duration, peak flux density, brightness temperature; fractional linear polarisation; circular polarisation, and total polarisation, and frequency drift rate. To avoid positive biases due to Ricean statistics, fractional polarisations were measured by masking out insignificant values (signal-to-noise ratio < 1) in the dynamic spectra, before averaging over frequency and taking the quadrature sum where relevant. Notes: a) This is a lower limit owing to the conservatively large size of the emission region used; b) AB2 exhibits reversals in its drift direction, preventing simple characterisation with a linear drift rate; c) Some linear polarisation is evident at the beginning of AB3. However, this is likely to be from the overlapping tail end of AB2.

of AB1 (bottom right). Table 4.1 summarises the important burst properties. The important observational characteristics of these bursts include high flux densities (peak flux density > 100 mJy, high degree of circular polarisation ($|V/I| > 50\%$), presence of moderate degrees of linear polarisation for AB1 and AB2 ($\sim 40\%$), and narrow-band and sharp-cutoff spectral features. To measure fractional polarisations, we masked insignificant values (signal-to-noise ratio < 1) in the dynamic spectra for each Stokes parameter, before averaging over frequency and taking quadrature sums where relevant. This mitigated positive biases toward the fractional polarisation due to the Ricean statistics of quadrature-summed signals.

To measure the drift rate of ASKAP Bursts 1 and 3 (AB1 and AB3), we measured a characteristic frequency of the burst for each temporal integration. We fit the time-frequency ordinate pairs with a linear model, using `emcee` (Foreman-Mackey et al., 2013) to estimate the slope and intercept parameters. AB1 is broadband, and its lower spectral cutoff is below the frequency range of the observations. For this reason, we measured the upper frequency cutoff (defined as the highest frequency where the intensity exceeds a 6σ threshold of 71 mJy), and took this as the characteristic frequency. The slope in the upper frequency cutoff of AB1 is evident in Figure 4.6. For AB3, we took the frequency of maximum flux density for each integration as the characteristic burst frequency, since the drifting component of AB3 is contained within the bandwidth of our observation. The derived drift rates are $-4.7 \pm 0.7\,\mathrm{MHz\,s^{-1}}$ for AB1 and $-7.0 \pm 0.2\,\mathrm{kHz\,s^{-1}}$ for AB3.

4.4.4 Determining the Radio Emission Mechanism

The brightness temperature is an important diagnostic of the emission mechanism, with very high brightness temperatures indicating a coherent emission process. Conservatively assuming a source size equal to the size of the full stellar disk ($R_* = 0.146R_\odot$; Ribas et al., 2017), we can calculate a lower limit on the brightness temperature using Equation 14 from Dulk (1985). The lower limits on the brightness temperature for each burst are given in Table 1, and lie within the range of

10^{10}–10^{11} K. Due to the high brightness temperatures, along with the high degrees of polarisation (up to 100%), and the spectral structure of the bursts (including narrow-band features and sharp frequency cutoffs), coherent emission is strongly favored. In the context of stellar radio emission, the most plausible coherent emission mechanisms are the electron cyclotron maser instability (ECMI), or plasma emission (Melrose, 2017; Dulk, 1985).

In the case of AB3, assuming that the drifting component with bandwidth $\Delta\nu \approx 120$ MHz arises from a single ECMI source, we can estimate the length of the emitting region L_s as $L_s \approx L_B \Delta\nu/\nu$, where $L_B = |B/\nabla B|$ is the magnetic scale height, taken to be close to the stellar radius (i.e. $\sim 1 \times 10^{10}$ cm). For $\Delta\nu = 120$ MHz, $\nu = 950$ MHz, we obtain a source length of 1.3×10^9 cm. Using this as the characteristic source size, we obtain brightness temperatures in the range of 10^{13} K to 10^{14} K, confirming the need for a coherent emission mechanism.

AB1 and AB2 also exhibit elliptical polarisation, as can be seen in Figures 4.6 and 4.7. Possible interpretations of its origin include intrinsically elliptically polarised emission arising from a strongly rarefied duct (Zic et al., 2019b; Melrose & Dulk, 1991); or coupling of the extraordinary and ordinary magneto-ionic modes as the radiation traverses an inhomogeneous quasi-transverse region (Kai, 1963). In the former case, only the ECMI can be responsible for the emission, while in the latter case both fundamental plasma emission or ECMI emission are plausible emission mechanisms. While both mechanisms are plausible, the complex time-frequency structure of AB2 and the lower frequency cutoff of AB3 can be more readily explained by the modulation and/or geometrical beaming effects of the ECMI mechanism, whereas plasma emission would require upward and downward motion and/or density fluctuations of an excited plasma region because this emission is more isotropic than beamed ECMI.

4.4.5 Inferring Physical Properties from the ECMI Emission

The properties of AB2 and AB3, which make up the type IV burst, can be used to infer properties of the associated post-eruptive loop system. The $\sim 40\%$ degree of linear polarisation in AB2 implies a strongly under-dense source region, since Faraday rotation effects, such as differential Faraday rotation and bandwidth depolarisation, should be strong in a dense and highly magnetised stellar corona (Sokoloff et al., 1998; Melrose & Dulk, 1991). Melrose & Dulk (1991) considered the elliptical polarisation of Jovian decametric radio emission (Lecacheux et al., 1991; Boudjada & Lecacheux, 1991), and argued that for the elliptical polarisation to be preserved along the propagation path, mode coupling around the emission region, and along the propagation must be weak. This leads to a condition on the electron density,

$$n_e \lesssim \alpha(\nu/25\,\mathrm{MHz})\,, \tag{4.6}$$

where α is a geometrical factor of order unity, which we take to be 1. Using this, we compute an electron density upper limit of $\sim 30\,\mathrm{cm}^{-3}$, corresponding to our lowest observing frequency $\nu = 744$ MHz. This limit is derived based on the emission angle relative to the magnetic field θ satisfying $\cos^2(\theta) \ll 1$, along with assumptions that $\nu_p^2/\nu^2 \ll 1$ and $\nu_p^2 \sin(\theta)/2\nu^2 \ll 1 - \nu_c/\nu \ll 1$ close to the emission region, and $\nu_p^2/\nu^2 \ll 1$, $\nu_c/\nu \ll 1$ more than about one magnetic scale length from the emission region (Melrose & Dulk, 1991). The emission frequency for ECMI is close to the local electron cyclotron frequency $\nu_c = eB/m_e c \approx 2.8B$ MHz, or its second harmonic. Assuming first (fundamental) harmonic emission, ECMI radiation in the ASKAP band (744–1031 MHz) corresponds to local magnetic field strengths ranging from ∼270–370 G. The low plasma density inferred from the elliptical polarisation implies a local plasma frequency $\nu_p \leq 100$ kHz, a factor of at least ∼ 1000 lower than the local electron cyclotron frequency. These properties satisfy the condition $\nu_p/\nu_c \ll 1$ for operation of the ECMI (Melrose & Dulk, 1982).

Using the observed frequencies of the emission, we can estimate the vertical extent of the post-eruptive loop system. The average surface magnetic field of Proxima Cen is 600±150 G (Reiners & Basri, 2008b). Considering that the magnetic field strength in active regions may be substantially stronger, we use a range of basal magnetic field strengths from 600–1600 G. Assuming (1) that the ECMI-emitting region fills a fraction between 0.1 and 0.5 of the length active loop (consistent with the fractional bandwidth of the bursts) from the footpoints, (2) an upper frequency cutoff for AB3 of ∼ 1200 MHz, and (3) a dipolar loop geometry (so that $B(r) \propto r^{-3}$), we estimate loop sizes from ∼0.3–1.0 stellar radii (∼ 0.3–1.0 × 10^{10} cm).

4.4.6 Probability of a Coincident Flare and Radio Burst

To compute the probability that the optical flare and AB1 are temporally aligned by chance coincidence, we followed the approach of Osten et al. (2005). We assume the probability distribution function of observing N flares occurring at a rate λ within a time interval Δt is

$$P(N \mid \lambda, \Delta t) = e^{-\lambda \Delta t}(\lambda \Delta t)^N / N!\,. \tag{4.7}$$

If two flare events in disparate wave bands are independent, then the probability of observing both within a time interval τ of each other is just the product of their independent rate probabilities. For the optical flare, using the bolometric flare energy of ∼ 1.6 × 10^{32} erg we calculate a rate for flare of this energy and higher of ∼ 0.04 day^{-1} using the cumulative flare frequency distribution model from Howard et al. (2018). The burst rate of Proxima Cen at radio frequencies is not well constrained and is likely to be frequency dependent (Villadsen & Hallinan, 2019). Given the six bursts observed in 46 hr of observing time with ASKAP, we estimate an ASKAP-band radio burst rate of ∼ 3 days^{-1}, above a detection threshold of a few millijansky.

Using the flare temporal model described above, we determine that the time at which the flare reaches 1% of its peak intensity is $94.59^{+0.32}_{-0.27}$ min. Taking this as the flare onset time, we obtain a temporal offset between the peak of AB1 and the flare onset of 42^{+19}_{-17} s, taking the 10 s ASKAP integration time as the uncertainty around the peak of AB1. Using Equation 4.7 with a temporal offset of 42 s, we obtain a probability of independent, coincident events of 3.2 × 10^{-8}, strongly indicating a causal relation. Considering there were four additional lower-energy flares detected by TESS during ASKAP observations (Vida et al., 2019b), and taking the total TESS flare rate of 1.49 days^{-1} (Vida et al., 2019b), we obtain a conservative trials-factor corrected coincidence probability of 7.8 × 10^{-6}. This is an overestimation, because the rate of energetic flares such as the one detected on MBJD 58605 is substantially lower than the total flare rate. This represents the first definitive association of an interferometrically detected coherent stellar burst with an optical flare in the literature.

4.4.7 Classification of Radio Bursts

The association of these radio bursts with the large optical flare indicates that they can be interpreted within the paradigm of solar radio bursts, which also are associated with multiwavelength activity. We interpret AB1 as a solar-like decimetric burst or an unresolved group of type III bursts. In the latter interpretation, we note that the measured frequency drift rate of $-4.7 \pm 0.7\,\mathrm{MHz\,s^{-1}}$ may represent the 'envelope' of the group of bursts rather than the drift of the individual bursts themselves. Solar observations show that both decimetric spike and type II bursts are often associated with hard X-ray bursts (Trottet, 1986; Stewart, 1978). The occurrence of AB1 prior to the impulsive phase of the flare (see Figure 4.3) suggests that particle acceleration was already ongoing during this early time (Trottet, 1986). This is consistent with the findings of Kundu et al. (2006), who detected decimetric bursts similar to AB1 prior to the impulsive phase of a flare, which occurred high above the impulsive flare energy release site. They suggested that these decimetric bursts indicate a destabilisation of the upper coronal magnetic field, which may be connected in some way to the flare energy release in the lower corona.

The onset of AB2 is 35 minutes after the flare impulsive peak, and occurs during the gradual decay phase of the flare. This burst lasts for 119 minutes and has a complex morphology, exhibiting a variety of both positive and negative drift components. These details of AB2 are consistent with the ~ 30 minute delays from solar flare peaks of the type IVdm bursts studied in Cliver et al. (2011), and of the complex early component of type IVdm bursts described in Takakura (1967). AB2 is also elliptically polarised, a property also exhibited by some type IV bursts (Kai, 1963).

The radio light-curves in Figure 4.2 show that AB3 either directly follows, or temporally overlaps with AB2, and shares the same handedness of circular polarisation. This suggests that they are two components of the same event, and are likely to originate from the same region in the stellar corona. The fractional bandwidth $\Delta\nu/\nu$ ranges from 0.1–0.3, although the upper frequency cutoff is not within the ASKAP frequency range at the early stages of the burst, so the upper limit may be higher. The burst is up to 100% circularly polarised, and exhibits a gradual drift of $-7.0 \pm 0.2\,\mathrm{kHz\,s^{-1}}$ over its 353 minute duration. These properties are again consistent with solar type IV bursts, which display high degrees of circular polarisation (up to 100%), high brightness temperatures ($\sim 10^{11}$ K; Cliver et al. 2011), and can show relatively modest fractional bandwidths (Benz & Tarnstrom, 1976). The long-duration, slowly drifting morphology of the event also closely resembles other type IVdm events from the Sun (e.g., see Figure 5(a) from Cliver et al., 2011 or Figure 2(d) from Takakura, 1963).

The properties of AB2 and AB3 together, and their association with the 1.6×10^{32} erg optical/Hα flare, identify this radio event as a type IV burst. Our detection of this event with full-Stokes dynamic spectroscopy along with the suite of multi-wavelength observations make this the most compelling example of a solar-like radio burst from another star to date.

4.4.8 Type IV Bursts as Indicators of Post-Eruptive Arcades and Coronal Mass Ejections

As described in Section 4.2.1, studies of solar type IV bursts have established that these events are very closely associated with CMEs and SEPs (Robinson, 1986; Cane & Reames, 1988a,b), and indicate ongoing electron acceleration during magnetic field reconfiguration in the wake of CMEs (e.g. Kahler & Hundhausen, 1992). Recently, a systematic study of solar type IV events by Salas-Matamoros & Klein (2020) established that these bursts occur in columnar structures near the extremities of post-eruptive loop arcades, which they ascribe to the magnetic flux rope of the outgoing CME. The association of post-eruptive loop arcades and CMEs with decimetric type IV bursts has also been noted by Cliver et al. (2011) – for example, the 2002 April 21 "HF type IV" burst presented in Kundu et al. (2004) and Cliver et al. (2011) occurred at the same time as the rise of a post-eruptive loop system after an X1.5 flare (Gallagher et al., 2002). Cliver et al. (2011) argued that these bursts may be originate in low-density flux tubes, with a field-aligned potential drop driving ECMI emission. Ultraviolet imaging of the rising post-eruptive loop arcades during the 2002 April 21 event showed the presence of evacuated flux tubes (Gallagher et al., 2002), supporting this claim, and perhaps explaining the existence of small degrees of linear polarisation in other solar type IV bursts (Kai, 1963; Melrose & Dulk, 1991). This picture, developed from multiwavelength observations of solar flares may explain the high degree of circular polarisation, presence of linear polarisation, and the long duration of the type IV burst from Proxima Cen. Driven by large-scale magnetic field reconfiguration associated with a post-eruptive loop arcade, the type IV burst from Proxima Cen is highly suggestive of a CME leaving the stellar corona (Robinson, 1986; Cane & Reames, 1988a; Tripathi et al., 2004).

If this type IV burst is indeed associated with a CME, it does not directly probe CME properties, but its exceptional nature indicates that eruptive processes on active M-dwarfs may only be associated with the most powerful flares. This is consistent with numerical simulations of CMEs and associated type II bursts by Alvarado-Gómez et al. (2020), who reported that a simulated CME with a kinetic energy of 1.7×10^{32} erg is weakly confined within a Proxima Cen-like magnetosphere. Applying a solar-like energy partition between bolometric flare energy and CME kinetic energy ($E_{K,\mathrm{CME}}$) of $E_{\mathrm{bol}}/E_{K,\mathrm{CME}} = 0.3$ (Emslie et al., 2012), we estimate a CME kinetic energy of $\sim 5.5 \times 10^{32}$ erg for the putative CME indicated by our flare–type IV event. Even with a more conservative energy partition $E_{\mathrm{bol}}/E_{K,\mathrm{CME}} = 1$ (Osten & Wolk, 2015) (resulting in $E_{K,\mathrm{CME}} = 1.6 \times 10^{32}$ erg), these CME kinetic energy estimates closely match or exceed the weak CME confinement scenario explored by Alvarado-Gómez et al. (2020), depending on the flare-CME energy partition.

If energetic flares such as the 1.6×10^{32} erg flare presented here are necessary for eruptive space weather events, then their low rate ($\sim 0.04\,\mathrm{day}^{-1}$; Howard et al., 2018) indicates that the space weather environment around Proxima Cen may be less threatening to planetary habitability than predicted by solar scaling relations (Osten & Wolk, 2015). However, without direct evidence for the putative CME and its influence on planetary companions, our inferences on the space weather environment around Proxima Centauri also remain indirect.

4.5 Conclusions

We have presented simultaneous optical and radio observations of the nearby active M-dwarf and planet host, Proxima Cen. Photometric monitoring with TESS and the Zadko 1 m Telescope reveal a large flare, with an estimated bolometric energy of 1.6×10^{32} erg. Simultaneous spectroscopic monitoring with WiFeS showed strong enhancements in Hα and other chromospheric emission lines, indicating substantial deposition of energy into the chromosphere. Radio observations with ASKAP reveal a sequence of intense coherent bursts associated with this flare. The first, AB1, occurred ~ 42 s before the onset of the optical flare. The burst properties are consistent with solar-like decimetric spike bursts, which occur prior to the impulsive phase of flares, and indicate electron acceleration prior to the main impulsive outburst. The spectro-temporal and polarisation properties of the radio bursts that trail the optical flare identify them as a type IV burst event. This is the most compelling identification of a solar-like radio burst from another star to date. Appealing to the properties of solar radio bursts, we suggest that the type IV burst from Proxima Cen is indicative of a CME, and ongoing electron acceleration in post-eruptive magnetic structures. Observational campaigns incorporating low-frequency radio, soft X-ray, and extreme ultraviolet observations may reveal in more detail the properties of post-eruptive loop systems on M-dwarfs, and directly probe CME properties. These will be required to verify the solar type IV burst-CME relationship on active M-dwarfs, and to probe the influence of these events on planetary companions. To this end, we strongly encourage further effort toward improving our understanding of space weather around active stars, which remains limited in comparison to the solar case.

Acknowledgements

We thank Gregg Hallinan and Stephen White for useful discussions, and Phil Edwards for providing comments on the manuscript. We thank the referee for their constructive feedback, which improved this work. A.Z. thanks Thomas Nordlander and Gary Da Costa for their advice on observing with the ANU 2.3m Telescope. A.Z. is supported by an Australian Government Research Training Program Scholarship. T.M. acknowledges the support of the Australian Research Council through Grant No. FT150100099. D.K. is supported by NSF Grant No. AST-1816492. Parts of this research were conducted by the Australian Research Council Centre of Excellence for Gravitational Wave Discovery (OzGrav), through Project No. CE170100004. M.A.M. acknowledges support from a National Science Foundation Astronomy and Astrophysics Postdoctoral Fellowship under Award No. AST-1701406. Some of the data presented in this paper were obtained from the Mikulski Archive for Space Telescopes (MAST). STScI is operated by the Association of Universities for Research in Astronomy, Inc., under NASA contract NAS5-26555. Support for MAST for non-HST data is provided by the NASA Office of Space Science via grant NNX13AC07G and by other grants and contracts. This research was supported by the Australian Research Council Centre of Excellence for All Sky Astrophysics in 3 Dimensions (ASTRO 3D), through Project No. CE170100013. The International Centre for Radio Astronomy Research (ICRAR) is a Joint Venture of Curtin University and The University of Western Australia, funded by the Western Australian State government. ASKAP is part of the Australia Telescope National Facility, which is managed by the CSIRO. Operation of ASKAP is funded by the Australian Government with support from the National Collaborative Research Infrastructure Strategy. ASKAP uses the resources of the Pawsey Supercomputing Centre. Establishment of ASKAP, the Murchison Radio-astronomy Observatory, and the Pawsey Supercomputing Centre are initiatives of the Australian Government, with support from the Government of Western Australia and the Science and Industry Endowment Fund. We acknowledge the Wajarri Yamatji as the traditional owners of the Murchison Radio-astronomy Observatory site.

Software: ASTROALIGN (Beroiz et al., 2020), ASTROPY (Astropy Collaboration et al., 2018), CASA (McMullin et al., 2007), CCDPROC (Craig et al., 2015), MATPLOTLIB (Hunter, 2007), NUMPY (van der Walt et al., 2011), SEXTRACTOR (Bertin & Arnouts, 1996), PYWIFES (Childress et al., 2014), SPECUTILS[5], EMCEE (Foreman-Mackey et al., 2013).

[5]https://specutils.readthedocs.io/

Chapter 5

Conclusions and outlook

In this thesis, we have investigated low-frequency radio emission from active low-mass stars, and harnessed this emission to probe their magnetospheres. Observations with ASKAP, detailed in Chapters 3 and 4, have clearly demonstrated the ability of this instrument to detect stellar radio bursts with unprecedented data quality. These observations also demonstrate the potential of the relatively unexplored frequency range of $\sim 700 - 1000$ MHz for exploring coherent stellar radio bursts (Villadsen & Hallinan, 2019). With commencement of the full ASKAP sky surveys on the horizon, the near future holds great promise for this area of research. In the following sections, I will summarise results from this thesis, and outline areas of future work.

5.1 Low frequency GMRT observations of ultra-cool dwarfs

In Chapter 2, we presented ~ 610 and ~ 1300 MHz Giant Metrewave Radio Telescope (GMRT) observations of nine ultra-cool dwarfs previously detected at radio frequencies. The aim of this investigation was to place tighter constraints on their magnetospheric properties by constraining the shape of the optically-thick end of the quiescent radio emission, and to determine the existence of a low-frequency component of the bursts observed at higher frequencies. We detected two of the nine targets: 2MASS J1314+1320, and 2MASS 0746+20 at both 610 and 1300 MHz, finding that only 2MASS J1314+1320 showed emission consistent with optically thick gyrosynchrotron radiation. None of the targets exhibited significant variability over timescales of minutes to hours, in contrast to the bursty behaviour observed at higher frequencies. Using our low-frequency measurements and archival measurements of flux density from the literature, we performed radiative transfer modelling to determine the range of coronal parameters consistent with the observed shape of the spectral energy distribution. We found that we could only place fairly weak constraints on the coronal parameters, largely due to the non-simultaneous measurements of the spectral flux densities which are variable on timescales of days-months, and an unknown source region size. Nonetheless, our observations demonstrate that some ultra-cool dwarfs are capable of producing low-frequency emission, but the majority do not. The lack of low-frequency bursts indicates that the electron cyclotron maser instability (ECMI) driving the bursts at higher frequencies is confined to the lower portions of the stellar magnetosphere.

5.2 ASKAP detection of periodic and elliptically polarised radio pulses from UV Ceti

In Chapter 3, we presented observations of the prototypical dMe flare star, UV Ceti (a.k.a L726−8 B) with the ASKAP during commissioning tests for the Variables and Slow Transients survey (Murphy et al., 2013). Previous studies of this M5.5e binary member have shown that it exhibits activity well-characterised by the solar paradigm (e.g. Guedel et al., 1996). In stark contrast to expectations for solar-like activity, recent low and mid-frequency radio observations hinted at a periodicity of the coherent radio bursts from UV Ceti – a signature of auroral activity seen on the lower-mass brown dwarfs, and on magnetised planets. Our ASKAP observations – the longest continuous radio-frequency observations of this star to date – confirmed the periodicity of these coherent bursts, showing for the first time that main-sequence active stars can possess large, stable auroral current systems. The similarity of the pulses observed ∼5 months apart suggests an origin from a stable magnetic feature in the stellar magnetosphere. Further, our observations revealed a linearly polarised component of the pulsed ECMI emission, confirming the earlier detection of elliptically polarised ECMI emission by Lynch et al. (2017). We argued that the existence of the linearly polarised component of the emission implies that the emission must arise from an extremely rarefied density cavity in the stellar magnetosphere, with a density $n_e \lesssim 41\,\mathrm{cm}^{-3}$ – at least 7 orders of magnitude less dense than expected from a simple hydrostatic equilibrium model of the corona. This may represent an extreme version of the low-density ducts observed in the terrestrial auroral regions (Ergun et al., 2000), but further investigation into the emission and its implications on the source environment is warranted. These results suggest that the transition from solar-like to planetary-like auroral activity may begin with active M-dwarfs, and that rapidly-rotating M-dwarfs with strong, large-scale dipolar magnetic fields may host aurorae similar to UV Ceti.

5.3 A flare-type IV burst event from Proxima Centauri and implications for space weather

Chapter 4 details results from one night of an 11-night multi-wavelength campaign targeting the active planet host, and nearest solar neighbour, Proxima Centauri (Proxima Cen). Like UV Ceti, Proxima Cen is also spectral type M5.5e, but is much more slowly-rotating, with a period of $\sim$ 82.5 days (Kiraga & Stepien, 2007) (c.f. 5.4432 ± 0.0072 h for UV Ceti; Barnes et al., 2017), and so occupies a different region of parameter space in the operation of fully-convective dynamos. The goal of our campaign was to detect signatures of space weather events from Proxima Centauri by observing solar-like coherent radio bursts, which have only been observed once before on another star (Kahler et al., 1982).

We detected a flare in optical continuum and chromospheric emission lines with photometric and spectroscopic monitoring, with an estimated bolometric energy of 2.1×10^{32} erg. ASKAP observations revealed a series of intense, coherent radio bursts which we associate with the large flare. The first of these bursts was a short, intense, and broadband burst which occurred approximately 50 s prior to the onset of the optical flare. This is the first confirmed coherent radio burst directly associated with multi-wavelength flaring activity from another star, indicating the operation of solar-like flaring activity. Two subsequent coherent bursts occurred during and after the decay phase of the flare. The polarisation properties, spectro-temporal morphology, and relationship with the optical flare allow us to identify these bursts as a solar-like type IV event. This is the first example of a solar-like radio burst detected with modern interferometric instruments, and with full-Stokes dynamic spectroscopy.

Solar type IV radio bursts are highly associated with CMEs (Salas-Matamoros & Klein, 2020; Robinson et al., 1986), and are thought to be driven by ongoing acceleration in magnetic structures (e.g. Salas-Matamoros & Klein, 2020; Cliver et al., 2011). By analogy with the established paradigm for solar type IV bursts, we suggest that the type IV burst from Proxima Cen is associated with a CME from the star, and indicates ongoing electron acceleration in a post-eruptive loop arcade or CME magnetic flux rope. Our detections show a promising CME candidate from Proxima Cen, indicating that CMEs may erupt from active M-dwarfs and generate a solar-like space weather environment.

5.4 Overview and future work

In this thesis, we sought to harness low-frequency radio emission from low-mass, active stars to investigate different manifestations of magnetic activity present in these objects. The lowest-mass stars – ultra-cool dwarfs and brown dwarfs – have been shown to exhibit planetary-like auroral activity (Hallinan et al., 2015). Using the GMRT, we have determined that most of these objects do not produce low-frequency emission, indicating that the driver for the auroral ECMI radio emission arises from the lower magnetosphere. We also demonstrated that low-frequency emission can be used to moderately constrain coronal properties of these low mass stars.

On the other hand, observations of active M-dwarfs from microwave to X-ray wavelengths have shown that their magnetic activity is well-described by the solar activity paradigm (e.g. Gudel et al., 1993; Guedel et al., 1996; Güdel et al., 2002a). However, modern low-frequency observations of these stars have been difficult to interpret in the solar paradigm (Kundu et al., 1988; Bastian, 1990; Villadsen & Hallinan, 2019). Our observation of a flare-type IV event from Proxima Cen demonstrates that at least some low-frequency emissions from active low-mass stars can operate in the solar paradigm, and that these stars may possess a solar-like space weather environment. In stark contrast, our observation of periodic pulses from the highly magnetic, rapidly-rotating 'twin' of Proxima Cen, UV Ceti (Kervella et al., 2016), reveal that active M-dwarfs with active solar-like coronae can also host stable, large-scale aurorae.

The similar mass, temperature, and spectral type, but distinct age and rotation rate of UV Ceti and Proxima Cen suggests that rotation is a key factor behind this apparent dichotomy in magnetic activity at low radio frequencies. This appears to be consistent with the picture of rapidly-rotating active stars possessing strong dipolar magnetic fields which gradually give way to more complex multipolar fields as they spin down and age (Yadav et al., 2016, 2015; Vidotto et al., 2014; Reiners & Basri, 2008a). Verifying this claim will clearly requires significantly more observational evidence, ideally through statistical studies of the prevalence of auroral vs. solar-like radio activity in active M-dwarfs as a function of mass, age, rotation rate, and, where possible, magnetic topology.

With this in mind, a promising line of future work will be to a search for auroral radio emission similar to UV Ceti from other active M-dwarfs. By investigating how the occurrence of this phenomenon depends on fundamental stellar properties such as mass, age, rotation rate, and planetary companions, we may better understand how these powerful current systems are generated in large-scale stellar magnetic fields. Detailed studies of individual systems may uncover more about the physical driver of the auroral systems, possibly indicating interaction with planetary companions (e.g. Vedantham et al., 2020).

We have also reported a promising candidate for a space weather event from Proxima Centauri. To detect additional rare stellar type IV radio bursts and verify their relationship with CMEs, further sustained multi-wavelength campaigns, harnessing low-frequency radio, X-ray, and ultra-violet observations, will be required. This will provide the first observational constraints on the space weather environment around active M-dwarfs.

A surprising phenomenon which we reported in Chapters 3 and 4 was the presence of a linearly-polarised component of the coherent emission. As discussed in Section 1.3.1, linear polarisation is expected to be destroyed or undetectable from within stellar coronae. Its presence therefore indicates very special conditions within and around the emission environment. In this work, we use the elliptical polarisation infer that the emission arises from extremely rarefied density cavities in the magnetosphere, similar to the case of Jovian decametric emission (Melrose & Dulk, 1991). However, the nature of these cavities, their formation, and their stability remains unclear. Furthermore, some of the emission shows evidence for Faraday rotation. We have begun exploring ways to harness this effect to probe the densities and magnetic fields in stellar coronae. However, any investigation will require careful assessment of the validity of the assumptions in magneto-ionic theory underpinning standard Faraday Rotation techniques.

The results presented in this thesis demonstrate the rich and varied phenomena in stellar magnetospheres that can be probed with low-frequency observations. Our results also raise further questions into the magnetic activity of low-mass stars, some of which we have outlined above. These future investigations will provide unique insights into the nature of magnetic fields around low-mass stars, and their effect on the circumstellar environment. With full ASKAP sky surveys commencing imminently, upgrades to the Murchison Widefield Array, and other Square Kilometre Array precursors such as MeerKAT and the Low Freqeuncy Array (LOFAR) approaching full operations, there appears to be fertile ground to explore in future.

Bibliography

Aarnio, A. N., Matt, S. P., & Stassun, K. G. 2012, ApJ, 760, 9, doi: 10.1088/0004-637X/760/1/9

Alvarado-Gómez, J. D., Drake, J. J., Cohen, O., Moschou, S. P., & Garraffo, C. 2018, ApJ, 862, 93, doi: 10.3847/1538-4357/aacb7f

Alvarado-Gómez, J. D., Drake, J. J., Moschou, S. P., et al. 2019, ApJ, 884, L13, doi: 10.3847/2041-8213/ab44d0

Alvarado-Gómez, J. D., Drake, J. J., Fraschetti, F., et al. 2020, ApJ, 895, 47, doi: 10.3847/1538-4357/ab88a3

Anglada-Escudé, G., Amado, P. J., Barnes, J., et al. 2016, Nature, 536, 437, doi: 10.1038/nature19106

Antonova, A. 2007, PhD thesis, Armagh Observatory, College Hill, Armagh BT61 9DG, UK

Antonova, A., Doyle, J. G., Hallinan, G., Bourke, S., & Golden, A. 2008, A&A, 487, 317, doi: 10.1051/0004-6361:20079275

Antonova, A., Doyle, J. G., Hallinan, G., Golden, A., & Koen, C. 2007, A&A, 472, 257, doi: 10.1051/0004-6361:20077231

Antonova, A., Hallinan, G., Doyle, J. G., et al. 2013, A&A, 549, A131, doi: 10.1051/0004-6361/201118583

Argiroffi, C., Reale, F., Drake, J. J., et al. 2019, Nature Astronomy, 3, 742, doi: 10.1038/s41550-019-0781-4

Aschwanden, M. J. 1986, Sol. Phys., 104, 57, doi: 10.1007/BF00159947

Aschwanden, M. J. 2005, Physics of the Solar Corona An Introduction with Problems and Solutions, Springer Praxis Books (Berlin, Heidelberg: Springer Berlin Heidelberg)

Astropy Collaboration, Robitaille, T. P., Tollerud, E. J., et al. 2013, A&A, 558, A33, doi: 10.1051/0004-6361/201322068

Astropy Collaboration, Price-Whelan, A. M., Sipőcz, B. M., et al. 2018, AJ, 156, 123, doi: 10.3847/1538-3881/aabc4f

Barnes, J. R., Jeffers, S. V., Haswell, C. A., et al. 2017, MNRAS, 471, 811, doi: 10.1093/mnras/stx1482

Bartels, J. 1937, Terrestrial Magnetism and Atmospheric Electricity (Journal of Geophysical Research), 42, 235, doi: 10.1029/TE042i003p00235

Bastian, T. S. 1990, Sol. Phys., 130, 265, doi: 10.1007/BF00156794

Bastian, T. S., Bookbinder, J., Dulk, G. A., & Davis, M. 1990, ApJ, 353, 265, doi: 10.1086/168613

Bastian, T. S., & Bookbinder, J. A. 1987, Nature, 326, 678, doi: 10.1038/326678a0

Beck, R. 2015, A&A Rev., 24, 4, doi: 10.1007/s00159-015-0084-4

Begelman, M. C., Blandford, R. D., & Rees, M. J. 1984, Reviews of Modern Physics, 56, 255, doi: 10.1103/RevModPhys.56.255

Benz, A. O. 2017, Living Reviews in Solar Physics, 14, 2, doi: 10.1007/s41116-016-0004-3

Benz, A. O., & Güdel, M. 2010, ARA&A, 48, 241, doi: 10.1146/annurev-astro-082708-101757

Benz, A. O., Gudel, M., & Schmitt, J. H. M. M. 1996, in Astronomical Society of the Pacific Conference Series, Vol. 93, Radio Emission from the Stars and the Sun, ed. A. R. Taylor & J. M. Paredes, 291

Benz, A. O., & Guedel, M. 1994, A&A, 285, 621

Benz, A. O., & Tarnstrom, G. L. 1976, ApJ, 204, 597, doi: 10.1086/154208

Berdyugina, S. V., Harrington, D. M., Kuzmychov, O., et al. 2017, ApJ, 847, 61, doi: 10.3847/1538-4357/aa866b

Berger, E. 2002, ApJ, 572, 503, doi: 10.1086/340301

—. 2006, ApJ, 648, 629, doi: 10.1086/505787

Berger, E., Ball, S., Becker, K. M., et al. 2001, Nature, 410, 338. https://arxiv.org/abs/astro-ph/0102301

Berger, E., Rutledge, R. E., Reid, I. N., et al. 2005, ApJ, 627, 960, doi: 10.1086/430343

Berger, E., Gizis, J. E., Giampapa, M. S., et al. 2008, ApJ, 673, 1080, doi: 10.1086/524769

Berger, E., Rutledge, R. E., Phan-Bao, N., et al. 2009, ApJ, 695, 310, doi: 10.1088/0004-637X/695/1/310

Berger, E., Basri, G., Fleming, T. A., et al. 2010, ApJ, 709, 332, doi: 10.1088/0004-637X/709/1/332

Beroiz, M., Cabral, J. B., & Sanchez, B. 2020, Astronomy and Computing, 32, 100384, doi: 10.1016/j.ascom.2020.100384

Bertin, E., & Arnouts, S. 1996, A&AS, 117, 393, doi: 10.1051/aas:1996164

Bigg, E. K. 1964, Nature, 203, 1008, doi: 10.1038/2031008a0

Bingham, R., & Cairns, R. A. 2000, Physics of Plasmas, 7, 3089, doi: 10.1063/1.874163

Boischot, A. 1957, Academie des Sciences Paris Comptes Rendus, 244, 1326

Boudjada, M. Y., & Lecacheux, A. 1991, A&A, 247, 235

Browning, M. K. 2008, ApJ, 676, 1262, doi: 10.1086/527432

Burgasser, A. J., & Putman, M. E. 2005, ApJ, 626, 486, doi: 10.1086/429788

Burningham, B., Hardcastle, M., Nichols, J. D., et al. 2016, MNRAS, 463, 2202, doi: 10.1093/mnras/stw2065

Burrows, A., Hubbard, W. B., Lunine, J. I., & Liebert, J. 2001, Reviews of Modern Physics, 73, 719, doi: 10.1103/RevModPhys.73.719

Cairns, I. H. 2011, in The Sun, the Solar Wind, and the Heliosphere, ed. M. P. Miralles & J. Sánchez Almeida, Vol. 4 (Berlin: Springer), 267

Cairns, I. H., Knock, S. A., Robinson, P. A., & Kuncic, Z. 2003, Space Sci. Rev., 107, 27, doi: 10.1023/A:1025503201687

Caldwell, J., Tokunaga, A. T., & Gillett, F. C. 1980, Icarus, 44, 667, doi: 10.1016/0019-1035(80)90135-9

Cane, H. V., & Reames, D. V. 1988a, ApJ, 325, 895, doi: 10.1086/166060

—. 1988b, ApJ, 325, 901, doi: 10.1086/166061

Carmichael, H. 1964, in AAS NASA Symposium on the Physics of Solar Flares: Proceedings of a Symposium Held at the Goddard Space Flight Center, Greenbelt, Maryland, October 28-30, 1963, Vol. 50, National Aeronautics and Space Administration, 451

Carrington, R. C. 1859, MNRAS, 20, 13, doi: 10.1093/mnras/20.1.13

Chabrier, G., & Baraffe, I. 1997, A&A, 327, 1039. https://arxiv.org/abs/astro-ph/9704118

—. 2000, ARA&A, 38, 337, doi: 10.1146/annurev.astro.38.1.337

Chabrier, G., & Küker, M. 2006, A&A, 446, 1027, doi: 10.1051/0004-6361:20042475

Chapman, S., & Ferraro, V. C. A. 1930, Nature, 126, 129, doi: 10.1038/126129a0

Childress, M. J., Vogt, F. P. A., Nielsen, J., & Sharp, R. G. 2014, Ap&SS, 349, 617, doi: 10.1007/s10509-013-1682-0

Chippendale, A., & Anderson, C. 2019, On-Dish Calibration of XY Phase for ASKAP's Phased Array Feeds, Tech. Rep. 19, ATNF ACES Memo. https://www.atnf.csiro.au/projects/askap/aces_memo_019.pdf

Christensen, U. R. 2010, Space Sci. Rev., 152, 565, doi: 10.1007/s11214-009-9553-2

Christensen, U. R., Holzwarth, V., & Reiners, A. 2009, Nature, 457, 167, doi: 10.1038/nature07626

Clarke, J. T., Ballester, G. E., Trauger, J., et al. 1996, Science, 274, 404, doi: 10.1126/science.274.5286.404

Cliver, E. W., & Dietrich, W. F. 2013, Journal of Space Weather and Space Climate, 3, A31, doi: 10.1051/swsc/2013053

Cliver, E. W., White, S. M., & Balasubramaniam, K. S. 2011, ApJ, 743, 145, doi: 10.1088/0004-637X/743/2/145

Committee on the Societal and Economic Impacts of Severe Space Weather Events. 2008, Severe Space Weather Events – Understanding Societal and Economic Impacts: A Workshop Report. (National Academies Press.)

Condon, J. J., Cotton, W. D., Greisen, E. W., et al. 1998, AJ, 115, 1693, doi: 10.1086/300337

Condon, J. J., & Ransom, S. M. 2016, Essential radio astronomy, Vol. 2 (Princeton University Press)

Coward, D. M., Gendre, B., Tanga, P., et al. 2017, PASA, 34, e005, doi: 10.1017/pasa.2016.61

Cowley, S., Bunce, E., & Prangé, R. 2004, Annales Geophysicae, 22, 1379, doi: 10.5194/angeo-22-1379-2004

Cowley, S. W. H., & Bunce, E. J. 2001, Planet. Space Sci., 49, 1067, doi: 10.1016/S0032-0633(00)00167-7

Craig, M. W., Crawford, S. M., Deil, C., et al. 2015, ccdproc: CCD data reduction software, 2.0.1. http://ascl.net/1510.007

Cranmer, S. R., & Winebarger, A. R. 2019, ARA&A, 57, 157, doi: 10.1146/annurev-astro-091918-104416

Crosley, M. K., & Osten, R. A. 2018a, ApJ, 862, 113, doi: 10.3847/1538-4357/aacf02

—. 2018b, ApJ, 856, 39, doi: 10.3847/1538-4357/aaaec2

Crosley, M. K., Osten, R. A., Broderick, J. W., et al. 2016, ApJ, 830, 24, doi: 10.3847/0004-637X/830/1/24

Damasso, M., Del Sordo, F., Anglada-Escudé, G., et al. 2020, Science Advances, 6, eaax7467, doi: 10.1126/sciadv.aax7467

Das, B., Chandra, P., Shultz, M. E., & Wade, G. A. 2019a, MNRAS, 489, L102, doi: 10.1093/mnrasl/slz137

—. 2019b, ApJ, 877, 123, doi: 10.3847/1538-4357/ab1b12

Das, B., Chandra, P., & Wade, G. A. 2018, MNRAS, 474, L61, doi: 10.1093/mnrasl/slx193

Das, B., Mondal, S., & Chandra, P. 2020, ApJ, 900, 156, doi: 10.3847/1538-4357/aba8fd

Davenport, J. R. A., Hawley, S. L., Hebb, L., et al. 2014, ApJ, 797, 122, doi: 10.1088/0004-637X/797/2/122

Davis, I., Taylor, G., & Dowell, J. 2020, MNRAS, 494, 4848, doi: 10.1093/mnras/staa988

Davis, R. J., Lovell, B., Palmer, H. P., & Spencer, R. E. 1978, Nature, 273, 644, doi: 10.1038/273644a0

DeBoer, D. R., Gough, R. G., Bunton, J. D., et al. 2009, IEEE Proceedings, 97, 1507, doi: 10.1109/JPROC.2009.2016516

Dennis, B. R., & Zarro, D. M. 1993, Sol. Phys., 146, 177, doi: 10.1007/BF00662178

Donati, J.-F., Forveille, T., Collier Cameron, A., et al. 2006, Science, 311, 633, doi: 10.1126/science.1121102

Donati, J. F., & Landstreet, J. D. 2009, ARA&A, 47, 333, doi: 10.1146/annurev-astro-082708-101833

Dopita, M., Hart, J., McGregor, P., et al. 2007, Ap&SS, 310, 255, doi: 10.1007/s10509-007-9510-z

Drake, J. J., Cohen, O., Yashiro, S., & Gopalswamy, N. 2013, ApJ, 764, 170, doi: 10.1088/0004-637X/764/2/170

Dulk, G. A. 1985, ARA&A, 23, 169, doi: 10.1146/annurev.aa.23.090185.001125

Dulk, G. A., Leblanc, Y., & Lecacheux, A. 1994, A&A, 286, 683

Dulk, G. A., & Marsh, K. A. 1982, ApJ, 259, 350, doi: 10.1086/160171

Dupuy, T. J., & Liu, M. C. 2012, ApJS, 201, 19, doi: 10.1088/0067-0049/201/2/19

Durney, B. R., De Young, D. S., & Roxburgh, I. W. 1993, Sol. Phys., 145, 207, doi: 10.1007/BF00690652

Emslie, A. G., Dennis, B. R., Shih, A. Y., et al. 2012, ApJ, 759, 71, doi: 10.1088/0004-637X/759/1/71

Ergun, R. E., Carlson, C. W., McFadden, J. P., et al. 2000, ApJ, 538, 456, doi: 10.1086/309094

Faherty, J. K., Burgasser, A. J., Cruz, K. L., et al. 2009, AJ, 137, 1, doi: 10.1088/0004-6256/137/1/1

Faherty, J. K., Burgasser, A. J., Walter, F. M., et al. 2012, ApJ, 752, 56, doi: 10.1088/0004-637X/752/1/56

Farnes, J. S. 2014, arXiv e-prints, arXiv:1407.0528. https://arxiv.org/abs/1407.0528

Fischer, G., Cecconi, B., Lamy, L., et al. 2009, Journal of Geophysical Research (Space Physics), 114, A08216, doi: 10.1029/2009JA014176

Fleming, T. A., Giampapa, M. S., & Schmitt, J. H. M. M. 2000, ApJ, 533, 372, doi: 10.1086/308657

Forbrich, J., Berger, E., & Reid, M. J. 2013, ApJ, 777, 70, doi: 10.1088/0004-637X/777/1/70

Forbrich, J., Dupuy, T. J., Reid, M. J., et al. 2016, ApJ, 827, 22, doi: 10.3847/0004-637X/827/1/22

Foreman-Mackey, D., Hogg, D. W., Lang, D., & Goodman, J. 2013, PASP, 125, 306, doi: 10.1086/670067

Gaia Collaboration, Brown, A. G. A., Vallenari, A., et al. 2018, A&A, 616, A1, doi: 10.1051/0004-6361/201833051

Gallagher, P. T., Dennis, B. R., Krucker, S., Schwartz, R. A., & Tolbert, A. K. 2002, Sol. Phys., 210, 341, doi: 10.1023/A:1022422019779

Gallet, F., & Bouvier, J. 2015, A&A, 577, A98, doi: 10.1051/0004-6361/201525660

Garraffo, C., Drake, J. J., & Cohen, O. 2016, ApJ, 833, L4, doi: 10.3847/2041-8205/833/1/L4

Garraffo, C., Drake, J. J., Cohen, O., Alvarado-Gómez, J. D., & Moschou, S. P. 2017, ApJ, 843, L33, doi: 10.3847/2041-8213/aa79ed

Gary, D. E., Linsky, J. L., & Dulk, G. A. 1982, ApJ, 263, L79, doi: 10.1086/183928

Gary, D. E., Linsky, J. L., & Dulk, G. A. 1983, in Solar and Stellar Magnetic Fields: Origins and Coronal Effects, ed. J. O. Stenflo, Vol. 102, 387–390

George, S. J. 2009, PhD thesis, The University of Birmingham, Birmingham University, Edgbaston Park Rd, Birmingham B15 2TT, UK

Gillon, M., Triaud, A. H. M. J., Demory, B.-O., et al. 2017, Nature, 542, 456, doi: 10.1038/nature21360

Ginzburg, V. L., & Zhelezniakov, V. V. 1958, Soviet Ast., 2, 653

Gizis, J. E., Monet, D. G., Reid, I. N., et al. 2000, AJ, 120, 1085, doi: 10.1086/301456

Goldreich, P., & Lynden-Bell, D. 1969, ApJ, 156, 59, doi: 10.1086/149947

Gopalswamy, N. 2004, in Astrophysics and Space Science Library, Vol. 317, The Sun and the Heliosphere as an Integrated System, ed. G. Poletto & S. T. Suess (Springer), 201, doi: 10.1007/978-1-4020-2831-9_8

—. 2006, Washington DC American Geophysical Union Geophysical Monograph Series, 165, 207, doi: 10.1029/165GM20

Güdel, M., Audard, M., Reale, F., Skinner, S. L., & Linsky, J. L. 2004, A&A, 416, 713, doi: 10.1051/0004-6361:20031471

Güdel, M., Audard, M., Skinner, S. L., & Horvath, M. I. 2002a, ApJ, 580, L73, doi: 10.1086/345404

Güdel, M., Audard, M., Smith, K. W., et al. 2002b, ApJ, 577, 371, doi: 10.1086/342122

Gudel, M., Schmitt, J. H. M. M., Bookbinder, J. A., & Fleming, T. A. 1993, ApJ, 415, 236, doi: 10.1086/173158

Guedel, M., Benz, A. O., Schmitt, J. H. M. M., & Skinner, S. L. 1996, ApJ, 471, 1002, doi: 10.1086/178027

Haisch, B., Strong, K. T., & Rodono, M. 1991, ARA&A, 29, 275, doi: 10.1146/annurev.aa.29.090191.001423

Haisch, B. M. 1989, Sol. Phys., 121, 3, doi: 10.1007/BF00161684

Haisch, B. M., Slee, O. B., Siegman, B. C., et al. 1981, ApJ, 245, 1009, doi: 10.1086/158878

Hale, G. E. 1908, ApJ, 28, 315, doi: 10.1086/141602

—. 1931, ApJ, 73, 379, doi: 10.1086/143316

Hallinan, G., Antonova, A., Doyle, J. G., et al. 2006, ApJ, 653, 690, doi: 10.1086/508678

—. 2008, ApJ, 684, 644, doi: 10.1086/590360

Hallinan, G., Bourke, S., Lane, C., et al. 2007, ApJ, 663, L25, doi: 10.1086/519790

Hallinan, G., Littlefair, S. P., Cotter, G., et al. 2015, Nature, 523, 568, doi: 10.1038/nature14619

Hancock, P. J., Murphy, T., Gaensler, B. M., Hopkins, A., & Curran, J. R. 2012, MNRAS, 422, 1812, doi: 10.1111/j.1365-2966.2012.20768.x

Hancock, P. J., Trott, C. M., & Hurley-Walker, N. 2018, PASA, 35, e011, doi: 10.1017/pasa.2018.3

Hardegree-Ullman, K. K., Cushing, M. C., Muirhead, P. S., & Christiansen, J. L. 2019, AJ, 158, 75, doi: 10.3847/1538-3881/ab21d2

Harding, J. C., Cairns, I. H., & Lobzin, V. V. 2019, ApJ, 877, 25, doi: 10.3847/1538-4357/ab19a0

Harding, L. K., Hallinan, G., Boyle, R. P., et al. 2013, ApJ, 779, 101, doi: 10.1088/0004-637X/779/2/101

Hawley, S. L., & Pettersen, B. R. 1991, ApJ, 378, 725, doi: 10.1086/170474

Hawley, S. L., Fisher, G. H., Simon, T., et al. 1995, ApJ, 453, 464, doi: 10.1086/176408

Heald, G., Mao, S., Vacca, V., et al. 2020, Galaxies, 8, 53, doi: 10.3390/galaxies8030053

Henry, T. J., Jao, W.-C., Subasavage, J. P., et al. 2006, AJ, 132, 2360, doi: 10.1086/508233

Hirayama, T. 1974, Sol. Phys., 34, 323, doi: 10.1007/BF00153671

Hodgson, R. 1859, MNRAS, 20, 15, doi: 10.1093/mnras/20.1.15

Hotan, A., Tuthill, J., Whiting, M., et al. submitted, PASA

Houdebine, E. R., Foing, B. H., & Rodono, M. 1990, A&A, 238, 249

Howard, W. S., Tilley, M. A., Corbett, H., et al. 2018, ApJ, 860, L30, doi: 10.3847/2041-8213/aacaf3

Hunter, J. D. 2007, Computing in Science and Engineering, 9, 90, doi: 10.1109/MCSE.2007.55

Intema, H. T. 2014, SPAM: Source Peeling and Atmospheric Modeling. http://ascl.net/1408.006

Intema, H. T., Jagannathan, P., Mooley, K. P., & Frail, D. A. 2017, A&A, 598, A78, doi: 10.1051/0004-6361/201628536

Intema, H. T., van der Tol, S., Cotton, W. D., et al. 2009, A&A, 501, 1185, doi: 10.1051/0004-6361/200811094

Irwin, J., Berta, Z. K., Burke, C. J., et al. 2011, ApJ, 727, 56, doi: 10.1088/0004-637X/727/1/56

Jackson, P. D., Kundu, M. R., & White, S. M. 1987, ApJ, 316, L85, doi: 10.1086/184898

Jaeger, T. R., Osten, R. A., Lazio, T. J., Kassim, N., & Mutel, R. L. 2011, AJ, 142, 189, doi: 10.1088/0004-6256/142/6/189

Johns-Krull, C. M., & Valenti, J. A. 1996, ApJ, 459, L95, doi: 10.1086/309954

Johnston, S., Taylor, R., Bailes, M., et al. 2008, Experimental Astronomy, 22, 151, doi: 10.1007/s10686-008-9124-7

Jonas, J. L. 2009, IEEE Proceedings, 97, 1522, doi: 10.1109/JPROC.2009.2020713

Kahler, S., Golub, L., Harnden, F. R., et al. 1982, ApJ, 252, 239, doi: 10.1086/159551

Kahler, S. W. 1982, ApJ, 261, 710, doi: 10.1086/160381

Kahler, S. W., & Hundhausen, A. J. 1992, J. Geophys. Res., 97, 1619, doi: 10.1029/91JA02402

Kai, K. 1962, PASJ, 14, 1

—. 1963, PASJ, 15, 195

—. 1965, PASJ, 17, 294

Kao, M. M., Hallinan, G., Pineda, J. S., et al. 2016, ApJ, 818, 24, doi: 10.3847/0004-637X/818/1/24

Kao, M. M., Hallinan, G., Pineda, J. S., Stevenson, D., & Burgasser, A. 2018, ApJS, 237, 25, doi: 10.3847/1538-4365/aac2d5

Kellermann, K. I., & Pauliny-Toth, I. I. K. 1969, ApJ, 155, L71, doi: 10.1086/180305

Kervella, P., Mérand, A., Ledoux, C., Demory, B. O., & Le Bouquin, J. B. 2016, A&A, 593, A127, doi: 10.1051/0004-6361/201628631

Khodachenko, M. L., Ribas, I., Lammer, H., et al. 2007, Astrobiology, 7, 167, doi: 10.1089/ast.2006.0127

Kiraga, M., & Stepien, K. 2007, Acta Astron., 57, 149. https://arxiv.org/abs/0707.2577

Kochukhov, O., & Lavail, A. 2017, ApJ, 835, L4, doi: 10.3847/2041-8213/835/1/L4

Kopp, R. A., & Pneuman, G. W. 1976, Sol. Phys., 50, 85, doi: 10.1007/BF00206193

Koskinen, H. 2011, Physics of Space Storms : From the Solar Surface to the Earth, Springer Praxis Books (Berlin, Heidelberg: Springer Berlin Heidelberg)

Küker, M., & Rüdiger, G. 1999, A&A, 346, 922

Kundu, M. R. 1965, Solar radio astronomy (Interscience Publishers)

Kundu, M. R., Garaimov, V. I., White, S. M., & Krucker, S. 2004, ApJ, 600, 1052, doi: 10.1086/379876

Kundu, M. R., Pallavicini, R., White, S. M., & Jackson, P. D. 1988, A&A, 195, 159

Kundu, M. R., White, S. M., Garaimov, V. I., et al. 2006, Sol. Phys., 236, 369, doi: 10.1007/s11207-006-0059-8

Lacy, C. H., Moffett, T. J., & Evans, D. S. 1976, ApJS, 30, 85, doi: 10.1086/190358

Lammer, H., Lichtenegger, H. I. M., Kulikov, Y. N., et al. 2007, Astrobiology, 7, 185, doi: 10.1089/ast.2006.0128

Lang, K. R. 2006, in Sun, Earth and Sky (New York, New York: Springer-Verlag), 136–163, doi: 10.1007/978-0-387-33365-6

Lang, K. R., & Willson, R. F. 1986, ApJ, 305, 363, doi: 10.1086/164253

Law, N. M., Hodgkin, S. T., & Mackay, C. D. 2006, MNRAS, 368, 1917, doi: 10.1111/j.1365-2966.2006.10265.x

Lecacheux, A., Boischot, A., Boudjada, M. Y., & Dulk, G. A. 1991, A&A, 251, 339

Leitzinger, M., Odert, P., Ribas, I., et al. 2011, A&A, 536, A62, doi: 10.1051/0004-6361/201015985

Leitzinger, M., Odert, P., Greimel, R., et al. 2020, MNRAS, 493, 4570, doi: 10.1093/mnras/staa504

Leto, G., Pagano, I., Linsky, J. L., Rodonò, M., & Umana, G. 2000, A&A, 359, 1035

Leto, P., Trigilio, C., Buemi, C. S., et al. 2017, MNRAS, 469, 1949, doi: 10.1093/mnras/stx995

Leto, P., Trigilio, C., Oskinova, L. M., et al. 2018, MNRAS, 476, 562, doi: 10.1093/mnras/sty244

Liebert, J., Kirkpatrick, J. D., Reid, I. N., & Fisher, M. D. 1999, ApJ, 519, 345, doi: 10.1086/307349

Lim, J., White, S. M., & Slee, O. B. 1996, ApJ, 460, 976, doi: 10.1086/177025

Linsky, J. L., & Gary, D. E. 1983, ApJ, 274, 776, doi: 10.1086/161490

Linsky, J. L., Wood, B. E., Brown, A., Giampapa, M. S., & Ambruster, C. 1995, ApJ, 455, 670, doi: 10.1086/176614

Llama, J., Jardine, M. M., Wood, K., Hallinan, G., & Morin, J. 2018, ApJ, 854, 7, doi: 10.3847/1538-4357/aaa59f

Louis, C. K., Hess, S. L. G., Cecconi, B., et al. 2019, A&A, 627, A30, doi: 10.1051/0004-6361/201935161

Lovell, A. C. B. 1964a, The Observatory, 84, 191

Lovell, B. 1963, Nature, 198, 228, doi: 10.1038/198228a0

—. 1964b, Nature, 203, 1213, doi: 10.1038/2031213a0

—. 1969, Nature, 222, 1126, doi: 10.1038/2221126a0

Lovell, B., Mavridis, L. N., & Contadakis, M. E. 1974, Nature, 250, 124, doi: 10.1038/250124a0

Lundin, R., Lammer, H., & Ribas, I. 2007, Space Sci. Rev., 129, 245, doi: 10.1007/s11214-007-9176-4

Luyten, W. J. 1949, ApJ, 109, 532, doi: 10.1086/145158

Lynch, C., Murphy, T., Ravi, V., et al. 2016, MNRAS, 457, 1224, doi: 10.1093/mnras/stw050

Lynch, C., Mutel, R. L., & Güdel, M. 2015, ApJ, 802, 106, doi: 10.1088/0004-637X/802/2/106

Lynch, C. R., Lenc, E., Kaplan, D. L., Murphy, T., & Anderson, G. E. 2017, ApJ, 836, L30, doi: 10.3847/2041-8213/aa5ffd

MacGregor, M. A., Osten, R. A., & Hughes, A. M. 2020, arXiv e-prints, arXiv:2001.10546. https://arxiv.org/abs/2001.10546

MacGregor, M. A., Weinberger, A. J., Wilner, D. J., Kowalski, A. F., & Cranmer, S. R. 2018, ApJ, 855, L2, doi: 10.3847/2041-8213/aaad6b

Martín, E. L. 1999, MNRAS, 302, 59, doi: 10.1046/j.1365-8711.1999.02099.x

McConnell, D., Allison, J. R., Bannister, K., et al. 2016, PASA, 33, e042, doi: 10.1017/pasa.2016.37

McLean, M., Berger, E., Irwin, J., Forbrich, J., & Reiners, A. 2011, ApJ, 741, 27, doi: 10.1088/0004-637X/741/1/27

McLean, M., Berger, E., & Reiners, A. 2012, ApJ, 746, 23, doi: 10.1088/0004-637X/746/1/23

McMullin, J. P., Waters, B., Schiebel, D., Young, W., & Golap, K. 2007, in Astronomical Society of the Pacific Conference Series, Vol. 376, Astronomical Data Analysis Software and Systems XVI, ed. R. A. Shaw, F. Hill, & D. J. Bell (San Francisco: ASP), 127

Melrose, D. B. 1986, Instabilities in space and laboratory plasmas (Cambridge: Cambridge University Press)

Melrose, D. B. 2009, in Universal Heliophysical Processes, ed. N. Gopalswamy & D. F. Webb, Vol. 257, 305–315, doi: 10.1017/S1743921309029470

Melrose, D. B. 2017, Reviews of Modern Plasma Physics, 1, 5, doi: 10.1007/s41614-017-0007-0

Melrose, D. B., & Dulk, G. A. 1982, ApJ, 259, 844, doi: 10.1086/160219

—. 1991, A&A, 249, 250

—. 1993, Planet. Space Sci., 41, 333, doi: 10.1016/0032-0633(93)90066-B

Melrose, D. B., Dulk, G. A., & Smerd, S. F. 1978, A&A, 66, 315

Melrose, D. B., & Wheatland, M. S. 2016, Sol. Phys., 291, 3637, doi: 10.1007/s11207-016-1006-y

Mestel, L. 2012, Stellar magnetism, 2nd edn., International series of monographs on physics ; 154 (Oxford: Oxford University Press)

Metodieva, Y. T., Kuznetsov, A. A., Antonova, A. E., et al. 2017, MNRAS, 465, 1995, doi: 10.1093/mnras/stw2597

Mohanty, S., & Basri, G. 2003, ApJ, 583, 451, doi: 10.1086/345097

Mohanty, S., Basri, G., Shu, F., Allard, F., & Chabrier, G. 2002, ApJ, 571, 469, doi: 10.1086/339911

Morin, J., Donati, J. F., Petit, P., et al. 2010, MNRAS, 407, 2269, doi: 10.1111/j.1365-2966.2010.17101.x

—. 2008, MNRAS, 390, 567, doi: 10.1111/j.1365-2966.2008.13809.x

Morosan, D. E., Kilpua, E. K. J., Carley, E. P., & Monstein, C. 2019, A&A, 623, A63, doi: 10.1051/0004-6361/201834510

Moschou, S.-P., Drake, J. J., Cohen, O., Alvarado-Gomez, J. D., & Garraffo, C. 2017, ApJ, 850, 191, doi: 10.3847/1538-4357/aa9520

Moschou, S.-P., Drake, J. J., Cohen, O., et al. 2019, ApJ, 877, 105, doi: 10.3847/1538-4357/ab1b37

Mullan, D. J., & Paudel, R. R. 2019, ApJ, 873, 1, doi: 10.3847/1538-4357/ab041b

Murphy, T., Chatterjee, S., Kaplan, D. L., et al. 2013, PASA, 30, e006, doi: 10.1017/pasa.2012.006

Mutel, R. L., Morris, D. H., Doiron, D. J., & Lestrade, J. F. 1987, AJ, 93, 1220, doi: 10.1086/114402

Nelson, G. J., Robinson, R. D., Slee, O. B., et al. 1979, MNRAS, 187, 405, doi: 10.1093/mnras/187.3.405

Ness, J. U., Güdel, M., Schmitt, J. H. M. M., Audard, M., & Telleschi, A. 2004, A&A, 427, 667, doi: 10.1051/0004-6361:20040504

Neupert, W. M. 1968, ApJ, 153, L59, doi: 10.1086/180220

Nichols, J. D., Burleigh, M. R., Casewell, S. L., et al. 2012, ApJ, 760, 59, doi: 10.1088/0004-637X/760/1/59

Ochsenbein, F., Bauer, P., & Marcout, J. 2000, A&AS, 143, 23, doi: 10.1051/aas:2000169

Oppermann, N., Junklewitz, H., Greiner, M., et al. 2015, A&A, 575, A118, doi: 10.1051/0004-6361/201423995

Ossendrijver, M. 2003, A&A Rev., 11, 287, doi: 10.1007/s00159-003-0019-3

Osten, R. A., & Bastian, T. S. 2006, ApJ, 637, 1016, doi: 10.1086/498410

Osten, R. A., Hawley, S. L., Allred, J. C., Johns-Krull, C. M., & Roark, C. 2005, ApJ, 621, 398, doi: 10.1086/427275

Osten, R. A., Hawley, S. L., Bastian, T. S., & Reid, I. N. 2006, ApJ, 637, 518, doi: 10.1086/498345

Osten, R. A., & Wolk, S. J. 2015, ApJ, 809, 79, doi: 10.1088/0004-637X/809/1/79

Osten, R. A., & Wolk, S. J. 2017, in IAU Symposium, Vol. 328, Living Around Active Stars, ed. D. Nandy, A. Valio, & P. Petit (Cambridge: Cambridge Univ. Press), 243–251, doi: 10.1017/S1743921317004252

O'Sullivan, S. P., Purcell, C. R., Anderson, C. S., et al. 2017, MNRAS, 469, 4034, doi: 10.1093/mnras/stx1133

Pandya, A., Zhang, Z., Chandra, M., & Gammie, C. F. 2016, ApJ, 822, 34, doi: 10.3847/0004-637X/822/1/34

Pettersen, B. R. 1989, Sol. Phys., 121, 299, doi: 10.1007/BF00161702

Pick, M. 1986, Sol. Phys., 104, 19, doi: 10.1007/BF00159942

Pineda, J. S., Hallinan, G., & Kao, M. M. 2017, ApJ, 846, 75, doi: 10.3847/1538-4357/aa8596

Prangé, R., Pallier, L., Hansen, K. C., et al. 2004, Nature, 432, 78, doi: 10.1038/nature02986

Quiroga-Nuñez, L. H., Intema, H. T., Callingham, J. R., et al. 2020, A&A, 633, A130, doi: 10.1051/0004-6361/201936491

Ravi, V., Hallinan, G., Hobbs, G., & Champion, D. J. 2011, ApJ, 735, L2, doi: 10.1088/2041-8205/735/1/L2

Reid, H. A. S., & Ratcliffe, H. 2014, Research in Astronomy and Astrophysics, 14, 773, doi: 10.1088/1674-4527/14/7/003

Reid, I. N., Kirkpatrick, J. D., Gizis, J. E., & Liebert, J. 1999, ApJ, 527, L105, doi: 10.1086/312409

Reid, M. J., & Moran, J. M. 1981, ARA&A, 19, 231, doi: 10.1146/annurev.aa.19.090181.001311

Reiners, A., & Basri, G. 2008a, ApJ, 684, 1390, doi: 10.1086/590073

—. 2008b, A&A, 489, L45, doi: 10.1051/0004-6361:200810491

—. 2009, A&A, 496, 787, doi: 10.1051/0004-6361:200811450

Ribas, I., Gregg, M. D., Boyajian, T. S., & Bolmont, E. 2017, A&A, 603, A58, doi: 10.1051/0004-6361/201730582

Ricker, G. R., Winn, J. N., Vanderspek, R., et al. 2015, Journal of Astronomical Telescopes, Instruments, and Systems, 1, 014003, doi: 10.1117/1.JATIS.1.1.014003

Riddle, A. C. 1970, Sol. Phys., 13, 448, doi: 10.1007/BF00153563

Robinson, P. A., & Cairns, I. H. 2000, Washington DC American Geophysical Union Geophysical Monograph Series, 119, 37, doi: 10.1029/GM119p0037

Robinson, P. A., & Melrose, D. B. 1984, Australian Journal of Physics, 37, 675, doi: 10.1071/PH840675

Robinson, R. D. 1986, Sol. Phys., 104, 33, doi: 10.1007/BF00159943

Robinson, R. D., Stewart, R. T., Sheeley, N. R., J., et al. 1986, Sol. Phys., 105, 149, doi: 10.1007/BF00156384

Robitaille, T., & Bressert, E. 2012, APLpy: Astronomical Plotting Library in Python. http://ascl.net/1208.017

Salas-Matamoros, C., & Klein, K.-L. 2020, A&A, 639, A102, doi: 10.1051/0004-6361/202037989

Sault, R. J. 2014, Initial characterisation of BETA polarimetric response, Tech. Rep. 2, ATNF ACES Memo. ftp://ftp.atnf.csiro.au/pub/people/sau078/memos/askap-1.pdf

Saur, J., Grambusch, T., Duling, S., Neubauer, F. M., & Simon, S. 2013, A&A, 552, A119, doi: 10.1051/0004-6361/201118179

Schlieder, J. E., Bonnefoy, M., Herbst, T. M., et al. 2014, ApJ, 783, 27, doi: 10.1088/0004-637X/783/1/27

Schwenn, R. 2006, Living Reviews in Solar Physics, 3, 2, doi: 10.12942/lrsp-2006-2

Segura, A., Walkowicz, L. M., Meadows, V., Kasting, J., & Hawley, S. 2010, Astrobiology, 10, 751, doi: 10.1089/ast.2009.0376

Shaposhnikov, V. E., Kocharovsky, V. V., Kocharovsky, V. V., et al. 1997, A&A, 326, 386

Shulyak, D., Sokoloff, D., Kitchatinov, L., & Moss, D. 2015, MNRAS, 449, 3471, doi: 10.1093/mnras/stv585

Skumanich, A. 1972, ApJ, 171, 565, doi: 10.1086/151310

Sokoloff, D. D., Bykov, A. A., Shukurov, A., et al. 1998, MNRAS, 299, 189, doi: 10.1046/j.1365-8711.1998.01782.x

Spangler, S. R., & Moffett, T. J. 1976, ApJ, 203, 497, doi: 10.1086/154105

Spangler, S. R., Rankin, J. M., & Shawhan, S. D. 1974, ApJ, 194, L43, doi: 10.1086/181664

Stewart, R. T. 1978, Sol. Phys., 58, 121, doi: 10.1007/BF00152558

Sturrock, P. A. 1966, Nature, 211, 695, doi: 10.1038/211695a0

Tagliaferri, G., Doyle, J. G., & Giommi, P. 1990, A&A, 231, 131

Takakura, T. 1963, PASJ, 15, 327

—. 1967, Sol. Phys., 1, 304, doi: 10.1007/BF00151359

Thompson, M. J., Toomre, J., Anderson, E. R., et al. 1996, Science, 272, 1300, doi: 10.1126/science.272.5266.1300

Tingay, S. J., Goeke, R., Bowman, J. D., et al. 2013, PASA, 30, e007, doi: 10.1017/pasa.2012.007

Tokar, R. L., Johnson, R. E., Hill, T. W., et al. 2006, Science, 311, 1409, doi: 10.1126/science.1121061

Treumann, R. A. 2006, A&A Rev., 13, 229, doi: 10.1007/s00159-006-0001-y

Trigilio, C., Leto, P., Leone, F., Umana, G., & Buemi, C. 2000, A&A, 362, 281. https://arxiv.org/abs/astro-ph/0007097

Tripathi, D., Bothmer, V., & Cremades, H. 2004, A&A, 422, 337, doi: 10.1051/0004-6361:20035815

Trottet, G. 1986, Sol. Phys., 104, 145, doi: 10.1007/BF00159956

Tsurutani, B. T., Gonzalez, W. D., Lakhina, G. S., & Alex, S. 2003, Journal of Geophysical Research (Space Physics), 108, 1268, doi: 10.1029/2002JA009504

van der Walt, S., Colbert, S. C., & Varoquaux, G. 2011, Computing in Science and Engineering, 13, 22, doi: 10.1109/MCSE.2011.37

van Haarlem, M. P., Wise, M. W., Gunst, A. W., et al. 2013, A&A, 556, A2, doi: 10.1051/0004-6361/201220873

van Maanen, A. 1940, ApJ, 91, 503, doi: 10.1086/144192

Vasavada, A. R., Bouchez, A. H., Ingersoll, A. P., et al. 1999, J. Geophys. Res., 104, 27133, doi: 10.1029/1999JE001055

Vedantham, H. K. 2020, A&A, 639, L7, doi: 10.1051/0004-6361/202038576

Vedantham, H. K., Callingham, J. R., Shimwell, T. W., et al. 2020, Nature Astronomy, 4, 577, doi: 10.1038/s41550-020-1011-9

Vida, K., Leitzinger, M., Kriskovics, L., et al. 2019a, A&A, 623, A49, doi: 10.1051/0004-6361/201834264

Vida, K., Oláh, K., Kővári, Z., et al. 2019b, ApJ, 884, 160, doi: 10.3847/1538-4357/ab41f5

Vidotto, A. A., & Cleary, A. 2020, MNRAS, 494, 2417, doi: 10.1093/mnras/staa852

Vidotto, A. A., Fares, R., Jardine, M., Moutou, C., & Donati, J. F. 2015, MNRAS, 449, 4117, doi: 10.1093/mnras/stv618

Vidotto, A. A., Jardine, M., Morin, J., et al. 2013, A&A, 557, A67, doi: 10.1051/0004-6361/201321504

Vidotto, A. A., Gregory, S. G., Jardine, M., et al. 2014, MNRAS, 441, 2361, doi: 10.1093/mnras/stu728

Villadsen, J., & Hallinan, G. 2019, ApJ, 871, 214, doi: 10.3847/1538-4357/aaf88e

Vourlidas, A., Buzasi, D., Howard, R. A., & Esfandiari, E. 2002, in ESA Special Publication, Vol. 1, Solar Variability: From Core to Outer Frontiers, ed. A. Wilson, 91–94

Vourlidas, A., Howard, R. A., Esfandiari, E., et al. 2010, ApJ, 722, 1522, doi: 10.1088/0004-637X/722/2/1522

Webb, D. F., & Howard, T. A. 2012, Living Reviews in Solar Physics, 9, 3, doi: 10.12942/lrsp-2012-3

Weber, E. J., & Davis, Leverett, J. 1967, ApJ, 148, 217, doi: 10.1086/149138

Wenger, M., Ochsenbein, F., Egret, D., et al. 2000, A&AS, 143, 9, doi: 10.1051/aas:2000332

West, A. A., Hawley, S. L., Bochanski, J. J., et al. 2008, AJ, 135, 785, doi: 10.1088/0004-6256/135/3/785

West, A. A., Hawley, S. L., Walkowicz, L. M., et al. 2004, AJ, 128, 426, doi: 10.1086/421364

White, S. 2007, Asian J. Phys., 16

White, S. M., Thejappa, G., & Kundu, M. R. 1992, Sol. Phys., 138, 163, doi: 10.1007/BF00146202

Wild, J. P., & McCready, L. L. 1950, Australian Journal of Scientific Research A Physical Sciences, 3, 387, doi: 10.1071/PH500387

Wild, J. P., Smerd, S. F., & Weiss, A. A. 1963, ARA&A, 1, 291, doi: 10.1146/annurev.aa.01.090163.001451

Williams, P. K. G., Berger, E., Irwin, J., Berta-Thompson, Z. K., & Charbonneau, D. 2015a, ApJ, 799, 192, doi: 10.1088/0004-637X/799/2/192

Williams, P. K. G., Casewell, S. L., Stark, C. R., et al. 2015b, ApJ, 815, 64, doi: 10.1088/0004-637X/815/1/64

Williams, P. K. G., Cook, B. A., & Berger, E. 2014, ApJ, 785, 9, doi: 10.1088/0004-637X/785/1/9

Yadav, R. K., Christensen, U. R., Morin, J., et al. 2015, ApJ, 813, L31, doi: 10.1088/2041-8205/813/2/L31

Yadav, R. K., Christensen, U. R., Wolk, S. J., & Poppenhaeger, K. 2016, ApJ, 833, L28, doi: 10.3847/2041-8213/833/2/L28

Yamada, M., Kulsrud, R., & Ji, H. 2010, Reviews of Modern Physics, 82, 603, doi: 10.1103/RevModPhys.82.603

Yang, Z., Bethge, C., Tian, H., et al. 2020, Science, 369, 694, doi: 10.1126/science.abb4462

Yu, S., Doyle, J. G., Kuznetsov, A., et al. 2012, ApJ, 752, 60, doi: 10.1088/0004-637X/752/1/60

Zarka, P. 1998, J. Geophys. Res., 103, 20159, doi: 10.1029/98JE01323

—. 2007, Planet. Space Sci., 55, 598, doi: 10.1016/j.pss.2006.05.045

Zarka, P., Marques, M. S., Louis, C., et al. 2018, A&A, 618, A84, doi: 10.1051/0004-6361/201833586

Zic, A., Lynch, C., Murphy, T., Kaplan, D. L., & Chandra, P. 2019a, MNRAS, 483, 614, doi: 10.1093/mnras/sty3163

Zic, A., Stewart, A., Lenc, E., et al. 2019b, MNRAS, 488, 559, doi: 10.1093/mnras/stz1684

Zic, A., Murphy, T., Lynch, C., et al. 2020, ApJ, 905, 23, doi: 10.3847/1538-4357/abca90